BURST-MODE LASER DEVELOPMENT FOR MHZ-RATE DIAGNOSTICS

by

Michael Edward Smyser

A Dissertation

Submitted to the Faculty of Purdue University

In Partial Fulfillment of the Requirements for the degree of

Doctor of Philosophy

School of Mechanical Engineering

West Lafayette, Indiana

December 2020

THE PURDUE UNIVERSITY GRADUATE SCHOOL
STATEMENT OF COMMITTEE APPROVAL

Dr. Terrence Meyer, Co-Chair
School of Mechanical Engineering

Dr. Mikhail Slipchenko, Co-Chair
School of Mechanical Engineering

Dr. Guillermo Paniagua
School of Mechanical Engineering

Dr. Haifeng Wang
School of Aeronautics and Astronautics

Approved by:
Dr. Nicole Key

Dedicated to Dr. Judy Walton; an academic and intellectual lifeline for a young man afflicted by apathy

ACKNOWLEDGMENTS

I will be writing my acknowledgements in the form of a personal message to individuals and/or groups.

Dr. Terrence R. Meyer,

As an undergraduate with a GPA of 3.45, my quantifiable academic excellence was relatively low compared to others applying for graduate school in our field. While I had held internships and other resume boosters, it must have been a considerable risk for you to recruit me as your second Purdue University student after Arafat. Whether it was my extremely charismatic nature, brilliant interview skills, optical background, or your desperation to find any student that met the bare minimum for your lab, I am eternally grateful that you recruited me into your ranks and served as a mentor for me throughout these years. I can honestly say that you were the perfect match for me, because you allowed me to be myself around you, and that allowed me to flourish. It felt like you treated me as much like a peer as a student, and your door (or email) was open for conversation regardless of the hour of day (or night). I really just want to say thank you for being so awesome.

Did you know that the group has many nicknames for you (spearheaded by yours truly)? Some of these include: The Big T, Young T, T-Steak, T-Bone, The T-Pot, T-Dawg, Terrodactyl, and Terry. These terms of endearment exemplify, not only the group's respect for you, but the relaxed and positive manner in which we can and do converse about you. Thank you for being a great mentor. Thank you for being a great person. Thank you for being The Big T.

Dr. Mikhail N. Slipchenko,

As the literal leading expert in our field, it was a blessing (and sometimes a curse) to be able to learn from you on a somewhat day-to-day basis. Your knowledge in the field was always appreciated in the end, even if it was somewhat annoying, at times, that you knew almost everything. We may not always agree on solutions for design layouts, aesthetically pleasing looks for quick fixes, or even the proper way for sledding down the Swiss Alps, but I have an immense amount of respect for who you are as a researcher, and more importantly, as a person. Thank you so much for your tutelage, and thank you for treating me like a peer (at least that is what it felt

like). At times earlier on in my tenure here, I recognized that whenever you were hard on me, it was because you expected a lot out of me, and that gave me more motivation than anything to get back into the lab and produce quality results. Терпенье и труд всё перетрут. I wish the best for you in the future, and I hope the future students that build the burst-mode lasers for the lab appreciate your knowledge as much as I do.

Dr. K. Arafat Rahman,

My days at Zucrow labs have seemed a little lonelier since you graduated and moved on to bigger and better things. While your brilliance and work ethic made your graduation inevitable, I have missed my office mate of 3 years tremendously. Thinking back to the summer of 2016 when it was just you, me, Terry, and Mikhail, I remember you stating that I was the first American graduate student to talk to you in the whole year you had already been here. I was happy to provide companionship to you then, especially since your now wife and entire family weren't even in the same country; and our academic and personal friendships grew from there. I find it somewhat humorous that it took you leaving for it to really hit me that the sense of companionship gained was very much mutual. I just wanted to formally thank you for a few things. Thank you for the many, many academic discussions we had. It was always nice to bounce ideas off of someone who didn't care how stupid the questions were before talking to Terry or Mikhail. Thank you for always making our version of "shooting the shit" extremely enjoyable. Whether it was shopping for engagement rings online together for both of our wives, watching Bangladesh thrash India in a game of Cricket, or discussing how to actually survive on a graduate student salary, it was always greatly appreciated. Thank you for being a good friend and the Shakib Al Hasan of office mates. I hope Alyssa and I can come and visit you, Shahereen, and the rest of your family in Bangladesh in the near future!

Dr. Jordan M. Fisher,

Thank you for being the ultimate counterpart in our experimental dynamic duo. It really felt like we could accomplish any experiment together; you with your aerospace background, and me with my optics background. You are one of my favorite people to work with because of the range of experiments we can accomplish, the ease at which they can be accomplished, and the manner in which we accomplish them in. Working with someone you can count on for, not only

their quality of work, promptness, and work ethic, but also their willingness to drink beer and shoot pool to celebrate a job well done, is an absolute blessing. Thank you for being a great coworker and an even greater friend. As the legend of J$ continues to live on elsewhere, I hope we can continue our professional relationship, and I guarantee we will continue our friendship.

TABLE OF CONTENTS

LIST OF TABLES

LIST OF FIGURES

ABSTRACT

This Ph.D. work is dedicated to advancements in burst-mode laser technology and their applications in MHz-rate high-speed gas-phase environments. A comprehensive computational model for simulating experimental burst-mode systems is discussed. Direct comparison of the modeled results to the output of a constructed nanosecond (ns) burst-mode laser shows agreement within a factor of 2 for output energy, the temporal domain skews positively in an appropriate manner, and the spectral domain correctly remains unchanged. The modeled output of a femtosecond (fs) burst-mode laser displays near perfect agreement with its hardware, generating only a 1.7% deviation for output energy, an 11% deviation in spectral bandwidth, and a temporal profile that correctly remains unchanged. The experimental ns to fs burst-mode lasers systems used to compare with the aforementioned model are described in detail and demonstrated for use in measurements of temperature, species, and velocity at high repetition rates.

In the ns regime, a compact-footprint (0.18 m^2) flashlamp-pumped, burst-mode Nd:YAG-based master-oscillator power-amplifier (MOPA) laser is developed with a fundamental 1064 nm output of over 14 J per burst. This portable laser system uses a directly modulated diode laser seed source to generate 10 ms duration arbitrary sequences of 500 kHz doublet or MHz singlet pulses for flow-field velocity or species measurements, respectively.

In the fs regime, a flashlamp-pumped burst-mode laser system with high peak power and a broad spectral bandwidth of >10 nm is constructed without the use of nonlinear compression techniques. A mode-locked, 1064.6 nm fundamental-wavelength broadband master oscillator, a fiber amplifier/pulse stretcher, and four Nd:glass power amplifiers are used to generate a sequence of high-repetition-rate, transform-limited 234 fs pulses over a 1 ms burst duration at a 0.1 Hz burst repetition rate. The generated peak powers are 1.24 GW at 100 kHz and 500 MW at 1 MHz with $M^2 \sim 1.5$.

An adaptation of the fs burst-mode laser is used for femtosecond laser electronic excitation tagging (FLEET) of nitrogen for tracking the velocity field in high-speed flows at kilohertz–megahertz (kHz–MHz) repetition rates without the use of added tracers. The fs burst-mode laser is used to produce 500 pulses per burst with pulses having a temporal separation as short as 1 μs, an energy of 120 μJ, and a duration of 274 fs. This enables 2 orders of magnitude higher measurement bandwidth over conventional kHz-rate FLEET velocimetry.

The fs burst-mode system was further improved to include a picosecond (ps) leg for hybrid fs/ps rotational coherent anti-Stokes Raman scattering (RCARS) at MHz rates. Using a common fs oscillator, the system simultaneously generates time synchronized 1061 nm, 274 fs and 1064 nm, 15.5 ps pulses with peak powers of 350 MW and 2.5 MW, respectively. The system is demonstrated for two-beam fs/ps RCARS in N_2 at 1 MHz with a signal-to-noise ratio of 176 at room temperature. This repetition rate is an order of magnitude higher than previous CARS using burst-mode ps laser systems and two to three orders of magnitude faster than previous continuously pulsed fs or fs/ps laser systems.

As a continuation of the above advances in fs regime, a regenerative fs burst-mode laser is discussed in detail with motivations, design layouts, and cavity physics laid out. Preliminary construction of the system with a ns seed source is underway to assess the detailed system design and evaluate the potential for optical damage due to Kerr lensing or other nonlinear effects. This system and other potential follow-on research topics are discussed.

1. INTRODUCTION

The purpose of this dissertation is to demonstrate advances in burst-mode laser technology development and its applications for MHz-rate measurements in high-speed gas-phase environments. This dissertation describes the fundamental background of the burst-mode laser, a universal burst-mode laser model applicable to any pulse width, direct improvements in the nanosecond (ns) and ultrafast regimes, and the design parameters and results for MHz-rate operation. Demonstrations of the practical utility of the advanced burst-mode laser systems include MHz-rate femtosecond (fs) laser electronic excitation tagging (FLEET) and hybrid femtosecond/picosecond coherent anti-Stokes Raman scattering (hybrid fs/ps CARS).

1.1 Motivation

Non-intrusive laser based diagnostic methods with high spatial and temporal resolution are of major importance when studying transient, stochastic, and dynamic flows in hypersonic systems, combustion, energetics, and a variety of other technical applications [1.1]. Recent efforts to improve the data rate of these diagnostics have shown the feasibility for MHz-rate seeded velocity measurements [1.2],[1.3] and single species measurements [1.4],[1.5]. The accuracy of velocity measurements based on particle seeding is limited by the tendency of particles to lag behind the true flow velocity in high-speed regimes. Prior single species measurements have been limited to qualitative imaging of few species, with significant potential for additional measurements that can track molecules instead of particles as well as target molecular energy distributions, major species, and temperature at high-speed flow conditions. These parameters are critical for understanding and modeling of pressure scaling, shock-chemistry interactions, detonation events, plasma-enhanced combustion, and other advanced concepts [1.4],[1.6]. Without such detailed information, new devices may not perform as predicted and/or they may incur significant delays and expenses in the development process.

With respect to single species measurements, ns spectroscopic techniques such as planar laser-induced fluorescence (PLIF), Raman spectroscopy, and Rayleigh scattering have been implemented at very high rates using burst-mode laser technology but suffer from pressure and species dependent collisional quenching rates and scattering cross sections. Multiline fluorescence

techniques can potentially alleviate dependence on collisions, but suffer from signal degradation and interferences from other molecular species (e.g., PAH, O_2, and CO_2). These interferences are exacerbated at higher pressure and with the use of practical hydrocarbon fuels. Filtered Rayleigh scattering can potentially alleviate scattering interferences from test-cell windows but has no chemical specificity and is not suitable for measuring molecular energy distributions.

Signal from ultrafast nonlinear laser-based techniques, such as CARS, are capable of collecting information about vibrational/rotational energy distributions, temperature, and species concentrations. Since the signal is a laser-like coherent beam, it can have high spatial resolution, can be easily be separated from background scattering, and can avoid emission background at high pressures and in hot plasmas.

Recently, the availability of ultrafast (picosecond and femtosecond) lasers has enabled kHz-rate point CARS, low data rate planar CARS imaging, measurements that are free of nonresonant background and collisions, thermometry over a wide temperature range, measurements of multiple species, and time dynamics investigations of rotational and vibrational states. The Air Force Research Laboratory pioneered ps CARS in combusting flows [1.7],[1.8], which allowed the measurement of temperature and collisional dephasing rates while suppressing nonresonant background. They then pioneered fs CARS for kHz-rate thermometry at high pressures without interference from nonresonant background or collisional dephasing [1.9],[1.10]. Finally, the same team in collaboration with the university researchers pioneered the use of fs and ps CARS, which gains the advantages of both techniques [1.11]-[1.13]. Known as hybrid fs/ps CARS, this technique can be advanced to the MHz regime for point, line, or planar measurements of vibrational/rotational energy states, temperature, and multiple species concentrations while suppressing the effects of nonresonant background and collisions [1.11],[1.12]. However, extending these measurements to the MHz regime in transient and nonequilibrium environments requires the development of new laser sources and imaging technology.

With respect to seeded velocimetry, challenges such as particle lag, limited optical access, particle seeding density issues, and desire to avoid hardware contamination discourage the application of planar Doppler velocimetry (PDV) and particle image velocimetry (PIV) in many supersonic and hypersonic test facilities. Molecular tagging based velocimetry techniques have been developed to combat the difficulties faced with making optical measurements in wind tunnel

environments. Introducing a gas-phase tracer, such as nitric-oxide into the flow, allows for velocity measurements that are not subject to particle lag

[1.14]. However, flow mixing and diffusion limit the ability of tracers to get into the desired measurement region, and mass injection can perturb the bulk flow that is being analyzed. Unseeded molecular tagging techniques take advantage of the fluorescence properties of molecules already present in air and therefore present the most promising avenue for advancement of non-intrusive velocimetry in ground test facilities. Raman excitation laser-induced electronic fluorescence (RELIEF)

[1.14],[1.15], Rayleigh-scattering velocimetry [1.16], and air photolysis and recombination tracking (APART) have been demonstrated but are subject to their own limitations discussed in the references.

Signal from ultrafast nonlinear laser-based techniques, such as FLEET, are capable of collecting information about velocity profiles in supersonic and hypersonic test facilities without the fidelity issues caused by particle seeding. FLEET is a technique that has been developed and demonstrated for velocimetry based on the dissociation and recombination of nitrogen molecules with the use of a femtosecond laser. FLEET allows velocity measurements in a simplified arrangement, necessitating the use of only one laser and camera, and can be performed in a line of sight configuration [1.17], requiring only one small window for optical access. FLEET has been shown to be a non-intrusive velocity measurement technique that is applicable to a wide range of Reynolds numbers and flow facilities. However, data acquisition for this method has generally been limited to a repetition rate of 1 kHz due to limitations of commercial femtosecond laser sources. A higher repetition rate is desired to capture time-resolved evolution of turbulent flow dynamics and coherent structures [1.18],[1.19].

1.2 Literature Review

The literature review is composed solely of burst-mode laser developments and innovations, and does not include literary sources acknowledging advances solely in diagnostics. In short, the proper citations relevant to the spectroscopic techniques presented later in this dissertation (i.e. CARS and FLEET) will be discussed and cited in those chapters.

1.2.1 Burst-Mode Laser Development

Burst-mode lasers have played a key role in advancing state-of-the-art measurements of such processes by providing high-energy laser pulses at very high repetition rates [1.1]. The "burst" concept derives from the reduction of the duty cycle of operation, and is critical to high rate laser diagnostics because the energy output of each pulse is constrained by the maximum average thermal load that the solid state lasing elements can tolerate [1.20]. Figure 1.1 illustrates the burst-mode concept. Commercially available lasers that operate with a continuous duty cycle (e.g. EdgeWave HD-Series) [1.21] operate at less than 1 kW of average power at 10 Hz repetition rates (100 J/pulse), shown in Figure 1.1a. At a repetition rate of 1 MHz (5 orders of magnitude shorter in time), limitations from material thermal attributes alone would allow less than 1 mJ per pulse of energy (5 orders of magnitude lower in energy). Essentially, 1 big pulse would be split into 100,000 smaller pulses. Most useful high-speed flow diagnostics experiments require more energy per pulse than this, especially ns techniques. In addition, such lasers are typically limited to a much smaller range of operating frequencies and output wavelengths. By reducing the duty cycle of operation, shown in Figure 1.1b and c, the energy per pulse can greatly increase for the same maximum average thermal load of the solid state lasing element.

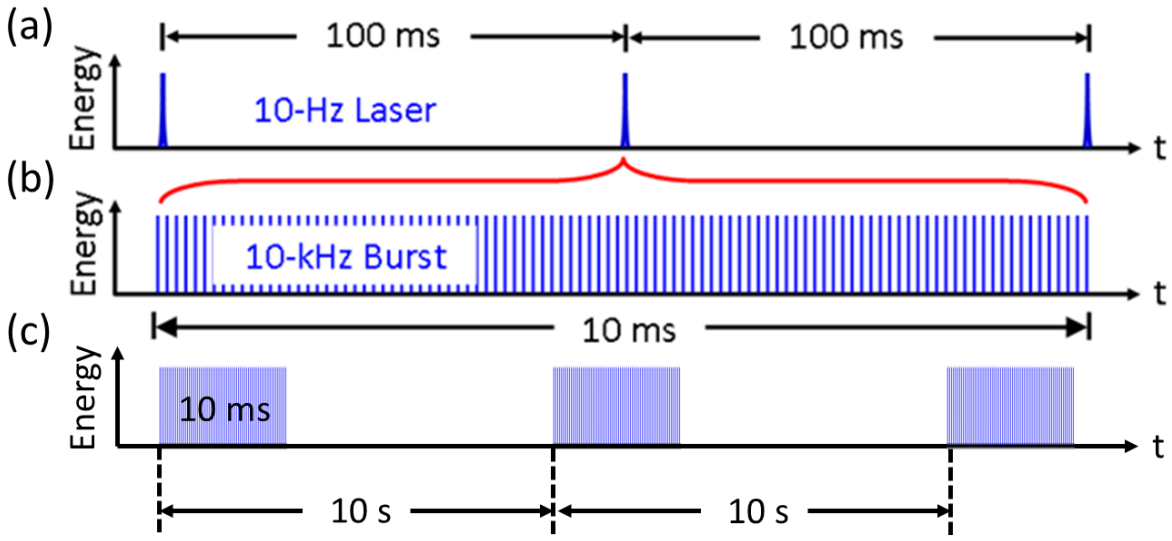

Figure 1.1. A representation of the burst-mode regime in time. (a) 10 Hz laser operation for a standard continuous duty cycle laser; (b) a representation of a burst of pulses at the same temporal location as in (a); and (c) an example of burst-mode duty cycle operation to allow thermal relaxation of solid state lasing elements.

Burst-mode lasers have evolved in both design and output since Ellis and Fourney built the first design in 1963 [1.22]. Table 1.1 shows the evolution of maximum laser repetition rates, burst energies, burst durations, pulse widths, and general comments. While many publications claimed certain characteristics, the table highlights bursts that were actually shown/described in their respective publications (e.g. claims of 250 kHz in the abstract but only gives 10 kHz burst details like energy, burst length, pulse-to-pulse uniformity, etc.). This comprehensive table does not include the advances that will be shown in this dissertation. The formatting of this table took inspiration from Slipchenko et al.'s recent publication, and each entry will be discussed chronologically [1.23].

Table 1.1. Burst-mode laser development and relevant statistics in chronological order from conception to the present. Advances in the same year are not necessarily in chronological order. Listed are year published, the fastest repetition rate listed that included the energy and burst duration with it, the operated energy/burst, the operated burst duration, the operated pulse width, and general comments about the laser itself.

Year Published	Operated Repetition Rate (kHz)	Operated Energy/Burst at Fundamental Wavelength (J)	Operated Burst Duration (ms)	Operated Pulse Width (ns)	Comments
1963 [1.22]	1000	Not listed	0.5	~50	Ruby Q-switching regime
1973 [1.24]	~100	0.06	0.09	20	Nd:YAG Q-switching
1978 [1.25]	120	~0.0005	0.1	60	5^{th} harmonic Nd:YAG AOM pulses for low power imaging
1994 [1.26]	500	5	0.5	100	Ruby Q-switching regime
1996 [1.20]	1000	0.03	0.1	20	First modern burst-mode laser (MOPA architecture)
1998 [1.27]	500	~20	0.14	10	Ruby Q-switching regime
1999 [1.28]	12.5	~10	1	Not listed	4 separate laser Nd:YAG Q-switching

Table 1.1 continued

2000 [1.29]	1000	2.1	.03	20	Increased energy from previous design
2003 [1.30]	1000	0.0045	0.03	20	Alexandrite regenerative amplifier
2004 [1.31]	100	1.2	.08	<10	Implemented phase-conjugate mirror with MOPA
2006 [1.32]	100	0.1	1	10	AOM seed slicing and uniform gain
2008 [1.33]	100	1.2	1	<10	Nd:YAG pumping OPO for NO PLIF
2008 [1.34]	250	1.3	0.08	70	Possible 20 ms burst and used Nd:YAG and Nd:glass
2009 [1.35]	100	2.7	1	6-25	Tunable wavelength with higher energy; up to 1 ms bursts
2009 [1.36]	500	0.0272	0.136	40	AOM slicing/ 50 MHz
2009 [1.37]	12.5	30	4	9	Nd:YAG Q-switching
2010 [1.38]	10	8.48	2	45	High-energy MOPA, for Thomson scattering
2011 [1.4]	1000	1	0.01	6-25	7 amplifiers Nd:YAG MOPA for NO PLIF
2012 [1.39]	10	200	1	25	High-energy 2-leg MOPA
2012 [1.40]	10	15	10	13	Diode and flashlamp pumped MOPA with fiber amplifier input
2013 [1.41]	75	~130	5	45	High energy MOPA with Nd:YAG and Nd:glass amplifiers
2013 [1.42]	10	36	30	13	Longest burst duration up to this point
2014 [1.43]	1000	100	10	0.1	First ps burst-mode laser
2014 [1.44]	100	400	100	13	Longest burst duration

Table 1.1 continued

2015 [1.45]	50	1.45	5	Not listed	Nd:YAG regenerative amplifier
2016 [1.46]	100	0.0425	0.25	14.5	Compact diode-pumped MOPA with Q-sqitch
2017 [1.47]	100	1.89	2	3.1	Compact Nd:YAG Q-switching and diode-pumped
2018 [1.48]	20	N/A	10	10	Dye burst-mode laser
2018 [1.49]	10	216	10	Not listed	3-legged MOPA for 3 techniques simultaneously
2020 [1.50]	1000	725	10	>5	8-amplifiers high energy system

In 1963, Ellis and Fourney conceptualized the burst-mode laser to achieve high-speed photography using a common ruby laser [1.22]. The pulsing was accomplished using cavity Q spoiling techniques with a Kerr cell. While exact energy outputs were not described (assumed to be consistent with ruby laser energies in 1963), varying cavity lengths resulted in laser operation of >1 Mc (1 MHz). Interestingly noted, they describe an instability of pulse amplitudes throughout their bursts, which is something that has to be monitored to this day.

In 1973, Bates published a burst-mode work utilizing the Nd:YAG medium for the first time [1.24]. He recognized that employing Q-switched ruby lasers wielding electro-optic modulators (EOM) (Kerr cell or Pockels cell) produce powerful pulses, but operate at a wavelength in which a lot of photographic materials were not highly sensitive. By frequency doubling the Nd:YAG fundamental wavelength of 1064 nm to 532 nm, a much wider range of emulsions could be used. He also notes that the 4-level Nd:YAG system is far more efficient than the 3-level ruby laser system. The actual laser design is similar to the ruby laser design in producing the fundamental wavelength pulses, and the singular amplifying rod is flashlamp pumped. The frequency doubled output holds characteristics of 20 ns pulse widths, 6 mJ energies/pulse, 10 pulses/burst, and 9 μs between pulses.

In 1978, Massey et al. extended upon harmonic generation and developed a burst-mode laser that could produce outputs down to the 5th harmonic [1.25]. The functionality of this laser also differed from Ellis and Bates, as the fundamental pulses were generated by placing a resonant, acousto-optic modulator (AOM) inside the cavity instead of an EOM. The purpose of the laser, since the output pulse peak power was much lower than conventional Q-switched lasers, was to produce flashlamp pumped focused pulses for photographic applications (illuminator for photoelectron microscope) requiring 212.8 nm wavelengths that would not damage the sample. The fundamental output characteristics include 60 ns pulse widths, 80 mJ burst energies, 120 kHz repetition rates, and 0.1 ms bursts. The 212.8 nm output characteristics include 60 ns pulse widths, 900 W peak power (0.05 mJ/pulse), 120 kHz repetition rates, and 0.1 ms bursts.

In 1994, Huntley expanded upon the previous works of Q-switched ruby burst-mode lasers for use in high-speed laser speckle photography [1.26]. The laser design is similar to previous Q-switched ruby lasers, utilizing an EOM and flashlamp pumping. The output characteristics include ~100 ns pulse widths, 20 mJ/pulse, 500 kHz repetition rates, and 0.5 ms fully amplified bursts.

In 1996, Lempert et al. produced what is widely considered the first modern burst-mode laser; it employs a master oscillator power amplifier (MOPA) scheme that has been the backbone for improvements in burst duration, pulse energy, repetition rate, pulse width, footprint, pulse tuning, and robust operation [1.20]. This specific laser was also the first burst-mode laser to perform spectroscopic measurements for flow diagnostics. The master oscillator is an Nd:YAG seed source, which is preamplified with 2 separate chains. In the second chain, the continuous wave source is sliced into 20 ns long pulses using 2 Pockels cells. The preamplifiers (Nd:YAG rods essentially) were effectively implemented to grow the seed source to a large enough output with inducing amplified spontaneous emission (ASE). The mature seed energy is sent through the power amplifier stage, and the output characteristics include 20 ns pulse widths, 10 mJ/pulse, 500 kHz repetition rates (up to 1 MHz but no energy listed), and 0.06 ms burst lengths (up to 0.1 ms).

In 1998, Grace et al. further expanded upon the previous works of Q-switched ruby burst-mode lasers in the high-speed photography realm [1.27]. A commercial ruby laser system was modified to provide a train of pulses by repetitive Q-switching in the oscillator cavity. The pulse-to-pulse stability was greatly improved, and the output characteristics include 10 ns pulse widths, 350 mJ/pulse, 500 kHz repetition rates, and 0.14 ms burst lengths.

In 1999, Kaminski et al. continued the previous works of Nd:YAG Q-switching to adequately analyze OH radical in a turbulent nonpremixed methane-air flame via planar laser induced fluorescence [1.28]. The total system comprises of four individual and independent Nd:YAG lasers with their own oscillator and amplification stage. Each of the four legs had a double pulse option included with their Pockels cell pulse slicers, so a total of 8 pulses could be produced in succession. A dye laser was pumped by these pulses to produce the correct wavelength for laser induced fluorescence. The output pulse characteristics prior to the pumping of the dye laser are listed for the second harmonic (532 nm), and are 270 mJ/pulse, 12.5 kHz repetition rates, and 1 ms burst lengths. The second harmonic conversion efficiency is not listed, but it can be reasonably assumed that the generation was saturated and the efficiency was greater than 30% (fundamental energy/pulse >1J/pulse). The pulse width is also not listed.

In 2000, Wu and Miles improved upon their previous MOPA system to successfully image shock evolution in a supersonic flow [1.29]. The only real addition to the previous design from 1996 was the addition of more flashlamp-pumped Nd:YAG amplifier chains. The output characteristics include 20 ns pulse widths, 70 mJ/pulse, 1 MHz repetition rates, and 0.03 ms bursts.

In 2003, Luff et al. constructed the first regenerative burst-mode system [1.30]. The system works by injecting a Q-switched 10 Hz pulse into the 32-meter-long cavity and allowing a portion of the beam to exit every x-amount of round trips. The cavity length has approximately a 107 ns round trip time, so 1 MHz can be attained with 10 round trips per pulse release. The cavity contains an alexandrite rod, and produces excellent beam quality (typical of a regenerative cavity). The external pulses are then amplified by 2 additional amplifiers, and all amplifiers are flashlamp-pumped. The output characteristics include 20 ns pulse widths, 0.15 mJ/pulse energies, 1 MHz repetition rates, and 0.03 ms bursts.

In 2004, Thurow et al. constructed a self-proclaimed “second generation” burst-mode laser for high-speed flow diagnostics, specifically planar Doppler velocimetry [1.31]. The specific improvement for this design is the incorporation of a phase-conjugate mirror near the end of the amplification chain for separation of the constant pedestal background from the pulses. The design follows the typical MOPA schematic, has Pockels cells for pulse slicing, and the output characteristics include <10 ns pulse widths, 150 mJ/pulse, 100 kHz repetition rates (up to 1 MHz), and 0.08 ms bursts.

In 2006, Thurow et al. expanded upon their previous work by adding 2 changes to their system [1.32]. They swapped out their dual Pockels cells pulse slicer in favor of an AOM for reasons of cost and the ability to produce variable repetition rates ranging from DC to 5 MHz. They also implemented a flashlamp controller to provide approximately uniform gain over the burst duration (as opposed to previous designs that had Gaussian shaped gain curves). The phase-conjugate mirror, used two years prior, was sidelined (most likely due to difficulty of use). The output characteristics include 10 ns pulse widths, 10 mJ/pulse, 10 kHz repetition rates (up to 5 MHz), and 1 ms bursts.

In 2008, two separate advances occurred, both stemming from the Lempert group. The first, by Jiang and Lempert, utilized 4th harmonic Nd:YAG pulses to pump an optical parametric oscillator (OPO) for planar laser-induced fluorescence imaging of nitric oxide [1.33]. The laser design was the exact same as the 2004 Thurow et al. laser, and the outputs are the same. The second, by Hartog et al., is the initial design of high-energy MOPA operation with a Q-switched seed source for the purposes of Thomson scattering [1.34]. The all-flashlamp-pumped system uses several Nd:YAG stages for initial amplification and silicate Nd:glass for the final stages. The employed capacitor banks allow burst durations from 0.3-20 ms. The output characteristics of the system include 70 ns pulse widths, 65 mJ/pulse energies, 250 kHz repetition rates, and 0.08 ms bursts.

In 2009, three separate advances occurred one was another advancement by Jiang et al. [1.35]. While this was officially published in 2008, the actual journal article was released in 2009, so this will be classified as a 2009 advancement. In their publication, the power supplies allowing variable pulse durations for flashlamps were incorporated (0.3-2 ms), and the flashlamp-pumped Nd:YAG burst-mode laser makes advances in realizable energy/pulse and burst length (uses 2 Pockels cells for slicing and PCM for pedestal removal). The laser was also used for more OPO pumping for a wide range of wavelength tuning for spectroscopic techniques like NO PLIF. The demonstrated fundamental output characteristics include pulse durations between 6 and 25 ns, 27 mJ/pulse energies, 100 kHz repetition rates, and 1.0 ms bursts.

Thurow et al., also in 2009, built upon their previous design with a self-proclamated “third generation” burst-mode laser system [1.36]. This system is essentially the final form of the laser published in 2006, and utilizes an AOM for pulse slicing and a variable pulse duration flashlamp for relatively uniform gain. The system uses Nd:YAG amplifiers, and operated output

characteristics include 40 ns pulse widths, 0.4 mJ/pulse, 500 kHz repetition rates (up to 50 MHz), and 0.13 ms bursts. This group also experimented with longer pulse physics, and a single 50 μs pulse carries with it 120 mJ of energy in this setup.

The final advancement in 2009 came from Hartog et al. in the Nd:YAG Q-switching regime for the purposes of Thomson scattering [1.37]. Utilizing an upgraded Pockels cell (repeatable on/off sequence) allows for the production of two or more Q-switched pulses from a single flashlamp pulse. Coupled with an improved flashlamp drive system, a sequence of high energy pulses are obtained. Utilizing two individual lasers in this scheme, the produced output characteristics are 9 ns pulse widths, ~2 J/pulse energies, 12.5 kHz repetition rates, and 4 ms bursts (triplet shots spaced out by 40 μs with a period of 1 ms for 4 ms).

In 2010, Harris et al. used a high-energy MOPA configuration burst-mode laser for the purposes of Thomson scattering [1.38]. The master oscillator consists of a commercial Q-switched Nd:YVO_4 laser, and the power amplifier consists of four Nd:YAG amplifiers. The laser operates for up to 20 ms in a continuous <50 kHz burst, or repetitive flashlamp 1 kHz discharges producing 10-30 pulse bursts up to 250 kHz. The system produces output characteristics of 45 ns pulse widths, 0.53 J/pulse energies, 10 kHz repetition rates, and 2 ms bursts.

In 2011, Jiang et al. expanded on their previous work from 2009 by producing a high-energy Nd:YAG MOPA configuration laser for NO PLIF imaging [1.4]. The only real addition to the previous laser was 2 additional amplifiers for higher energy production. The output characteristics include 6-25 ns pulse durations, 100 mJ/pulse energies, 1 MHz repetition rates, and 0.01 ms bursts.

In 2012, two advances were made in the burst-mode regime. Fuest et al. created a MOPA configuration that utilizes 2 separate legs to amplify a split beam and recombines via polarizing beams splitter with orthogonal polarizations [1.39]. The amplifying media are flashlamp pumped Nd:YAG rods, the master oscillator is an Nd:YVO_4 source and a PCM is installed which effectively eliminates the pedestal in the burst. The output characteristics include 25 ns pulse durations, 2 J/pulse energies, 10 kHz repetition rates, and 1 ms bursts.

Slipchenko et al. used the MOPA architecture in conjunction with a fiber amplifier for initial amplification and 2 diode-pumped amplifiers for the purposes of CH_2O imaging [1.40]. All amplifiers are Nd:YAG. The inclusion of the fiber amplifier mitigates the necessity of free-space preamplification chains used in previous works. This improves overall beam quality and reduced

complexity and power requirements of a system. The inclusion of diode-pumped amplifiers (higher thermal efficiency compared to flashlamps) allows for longer burst durations with uniform pulse-to-pulse stability. They use an optical isolator and EOM combination to completely remove the initial ASE in the system from the fiber amplifier (as opposed to using a PCM), and the system contains a total of 4 amplifiers. The output characteristics include 13 ns pulse durations, 150 mJ/pulse energies, 10 kHz repetition rates, and 10 ms burst lengths.

In 2013, two advances were made in the burst-mode regime. Young et al. created a high-energy MOPA configuration burst-mode laser that incorporates 4 Nd:YAG and 1 Nd:glass flashlamp pumped amplifiers for the purposes of Thomson scattering [1.41]. The master oscillator is a Q-switched, diode-pumped Nd: YVO_4 source. The MOPA operates in 2 regimes, the first being a uniform repetition rate sustained for 5-8 ms, and the second being shorter bursts at higher repetition rates (75 kHz) separated by a longer period (1 kHz). The output characteristics of a 5 ms burst operating in the second form (5 bursts of 15 pulses with 1 ms between bursts) are 45 ns pulse widths, 1.5-2 J/pulse energies (pretty non-uniform burst), and 75 kHz repetition rates.

Slipchenko et al. expanded upon their previous work from 2012 by creating the first all-diode-pumped burst-mode laser [1.42]. This MOPA utilizes the same advances from 2012 (i.e. Yb fiber amplifier) for ASE reduction, and employs only 3 diode-pumped Nd:YAG amplifiers. The major point of this change was to increase the burst duration to 30 ms without the terrible pulse-to-pulse uniformity that would accompany flashlamps for this length of burst. The output characteristics of this laser include 13 ns pulse durations, 120 mJ/pulse energies, 10 kHz repetition rates, and 30 ms bursts.

In 2014, two advances were made in the burst-mode regime. Roy et al. created the first ps burst-mode laser for ultrafast spectroscopy [1.43]. This laser utilizes a 100 ps mode-locked seed source and is duty cycled from its mode-locked repetition rate down to 10-1000 kHz via fiber coupled AOM. The pulses are preamplified with a single mode fiber amplifier, and sent through a free space power amplification system composed of 4 diode-pumped Nd:YAG amplifiers. The output characteristics include 100 ps pulse durations, 10 mJ/pulse energies, 1 MHz repetition rates, and 10 ms burst lengths with excellent pule-to-pulse uniformity.

Slipchenko et al. expanded on their previous works from 2012 and 2013 by created a burst-mode laser with the longest burst duration to date [1.44]. The burst-mode laser utilizes a MOPA configuration with fiber coupled diode laser as a seed source. The amplifier chain consists of 6

Nd:YAG diode-pumped amplifiers. The novelty in this design is the use of dual-wavelength array diode emission. As diodes heat up, their wavelengths shift, so a single wavelength diode will lose efficiency over time with respect to its overlap with the Nd:YAG absorption spectrum. With diodes operating at 2 separate wavelengths (offset from the central wavelength by approximately the same amount in opposite directions), the time of uniform gain can be increased at a cost of peak gain. The resulting output characteristics include 13 ns pulse durations, 40 mJ/pulse energies, 100 kHz repetition rates, and 100 ms bursts.

In 2015, Mance et al. constructed the most recent regenerative amplifier burst-mode laser using Nd:YAG media [1.45]. The laser was constructed using a convex-concave cavity structure, and a quarter-wave plate combined with a Pockels cell locks the pulses into the cavity. The cavity consists of 2 flashlamp-pumped Nd:YAG rods. Prior to energy bifurcations, the output characteristics include 5.8 mJ/pulse energies, 50 kHz repetition rates, and 5 ms bursts.

In 2016, Pan et al. built a compact diode-pumped Nd:YAG MOPA with a Q-switched oscillator [1.46]. There are 3 total amplifiers in the system. The output characteristics include 14.5 ns pulse widths, 1.7 mJ/pulse energies, 100 kHz repetition rates, and 0.25 ms.

In 2017, Wu et al. constructed a compact diode-pumped Nd:YAG Q-switching burst-mode laser [1.47]. They use a cavity dumping process similar to the alexandrite regenerative laser mentioned earlier and amplify the output pulses with 2 more double-passed Nd:YAG rods. The output characteristics include 3.1 ns pulse widths, 9.45 mJ/pulse energies, 100 kHz repetition rates, and 2 ms bursts.

In 2018, two advances were made in the burst-mode regime. Pan et al. crafted a tunable wavelength burst-mode laser by pumping a dye laser with an Nd:YAG burst-mode laser [1.48]. The idea is essentially the same as pumping an OPO with a burst-mode laser to create the exact wavelength needed for PLIF, but the medium is liquid dye instead of a solid crystal. It is described in the publication that higher conversion efficiencies can be achieved for ultraviolet excitation pulses as compared to a burst-mode OPO, but repetition rates are limited due to the exchange times needed for the dye solution to recirculate. Since the novelty of this burst-mode laser is the dye laser itself, the fundamental 1064 nm statistics of the pumping burst-mode laser has no relevance, so reporting its statistics into the table is redundant and meaningless for comparison sake. The dye in the laser is Rh6G, the operable repetition rates range from 7.5 to 20 kHz, the output pulse widths are ~10 ns, burst lengths are 10 ms, and pulse energies of ~2 mJ are obtainable at 283 nm.

Roy et al. created a 3-leg high-energy flashlamp-pumped system for operating 3 simultaneous spectroscopic techniques on a system [1.49]. The 3 legs share the master oscillator, fiber amplifier, and a preamplifying leg before being split. A clever use of AOMs and Pockels cells split the incumbent pulse train into the 3 separate legs, and each of these pulses are sent through Nd:YAG amplification chains. The MOPA architecture is used for simultaneous PIV, OH PLIF, and CH_2O PLIF by frequency doubling and tripling the necessary legs. The fundamental output characteristics include 1000+570+590=2160 mJ/pulse, 10 kHz repetition rates (up to 500 kHz), and 10 ms bursts.

In 2020, Felver et al. made the final advancement to date in the burst-mode field and extended MHz-rate flow diagnostic possibilities [1.50]. Utilizing a MOPA configuration, a directly modulated diode master oscillator or a fiber-coupled AOM in tandem with a continuous wave source is employed for pulse width control. These master oscillators are swapped depending on pulse width needs for optimizing second harmonic generation conversion efficiency and staying below the damage threshold of the crystal. The overall layout is consistent with previous MOPA layouts, but the flashlamps were modified to provide more pumping energy to the 2 preamplifier Nd:YAG and 6 amplifier Nd:YAG rods in the setup. The output characteristics include >5 ns pulse widths, 72.5 mJ/pulse energies, 1 MHz repetition rates, and 10 ms burst durations.

The remainder of this dissertation describes further advances in the development of burst-mode laser technology, beginning with a model used to predict laser performance from the ns to the fs regime, experimental validation, and practical application to a variety of diagnostic approaches.

1.3 References

[1.1] B. Thurow, N. Jiang, and W. Lempert, “Review of ultra-high repetition rate laser diagnostics for fluid dynamic measurements”, Measurement Science and Technology, Volume 24, Number 1, 012002 (2013).

[1.2] B. Thurow, N. Jiang, W. Lempert, and M. Samimy, “Development of Megahertz-Rate Planar Doppler Velocimetry for High-Speed Flows”, AIAA, Volume 43, Number 5, (2005).

[1.3] N. Buchmann, C. Atkinson, and J. Soria, “Ultra-high-speed tomographic digital holographic velocimetry in supersonic particle-laden jet flows”, Measurement Science and Technology, Vol. 24, No. 2, (2012).

[1.4] N. Jiang, M. Webster, W. Lempert, J. Miller, T. Meyer, C. Ivey, and P. Danehy, "MHz-rate nitric oxide planar laser-induced fluorescence imaging in a Mach 10 hypersonic wind tunnel." Appl. Opt. 50, A20-A28, (2011).

[1.5] N. Jiang, J. Bruzzese, R. Patton, J. Sutton, R. Yentsch, D. Gaitonde, W. Lempert, T. Meyer, R. Parker, T. Wadham, M. Holden, and P. Danehy, "NO PLIF imaging in the CUBRC 48-inch shock tunnel", Experiments in Fluids, Volume 53, Issue 6, 1637-1646, (2012).

[1.6] C. Park, "Review of chemical-kinetic problems of future NASA missions. I – Earth entries", Journal of Thermophysics and Heat Transfer 7, 385-398, (1993).

[1.7] S. Roy, T. Meyer, and J. Gord, "Time-resolved dynamics of resonant and nonresonant broadband picosecond coherent anti-Stokes Raman scattering signals", Appl. Phys. Lett. 87, 264103, (2005).

[1.8] T. Meyer, S. Roy, and J. Gord, "Improving Signal-to-Interference Ratio in Rich Hydrocarbon-Air Flames Using Picosecond Coherent Anti-Stokes Raman Scattering", Appl. Spectrosc. 61, 1135, (2007).

[1.9] R. Lucht, S. Roy, T. Meyer, and J. Gord, "Femtosecond coherent anti-Stokes Raman scattering measurement of gas temperature from frequency-spread dephasing of the Raman coherence", Appl. Phys. Lett. 89, 251112, (2006).

[1.10] J. Gord, T. Meyer, and S. Roy, "Applications of Ultrafast Lasers for Optical Measurements in Combusting Flows", Annu. Rev. Anal. Chem. 1, 663, (2008).

[1.11] J. Miller, M. Slipchenko, T. Meyer, H. Stauffer, and J. Gord, "Hybrid femtosecond/picosecond coherent anti-Stokes Raman scattering for high-speed gas-phase thermometry", Opt. Lett. 35, 2430-2432, (2010).

[1.12] J. Miller, C. Dedic, S. Roy, J. Gord, and T. Meyer, "Interference-free gas-phase thermometry at elevated pressure using hybrid femtosecond/picosecond rotational coherent anti-Stokes Raman scattering", Opt. Express 20, 5003-5010, (2012).

[1.13] C. Dedic, J. Miller, and T. Meyer, "Dual-pump vibrational/rotational femtosecond/picosecond coherent anti-Stokes Raman scattering temperature and species measurements", Opt. Lett. 39, 6608-6611, (2014).

[1.14] W. Lempert, Y. Zuzeek, M. Uddi, K. Frederickson, N. Jiang, S. Roy, T. Meyer, S. Gogineni, and J. Gord, "RELIEF Velocimetry Using Picosecond Tagging and Nd:YAG-based Interrogation", 25th AIAA Aerodynamic Measurement Technology and Ground Testing Conference, Fluid Dynamics and Co-located Conferences, AIAA 2006-2970.

[1.15] R. Miles, C. Cohen, J. Connors, P. Howard, S. Huang, E. Markovitz, and G. Russell, "Velocity measurements by vibrational tagging and fluorescent probing of oxygen", Opt. Lett. 12, 861-863, (1987).

[1.16] J. Forkey, N. Finkelstein, W. Lempert, and R. Miles, "Demonstration and characterization of filtered Rayleigh scattering for planar velocity measurements", AIAA Journal, Vol. 34, No. 3, 442-448, (1996).

[1.17] R. Burns, P. Danehy, B. Halls, and N. Jiang, "Application of FLET Velocimetry in the NASA Langley 0.3-Meter Transonic Cryogenic Tunnel", AIAA Journal, Vol. 55, No. 2 (2017).

[1.18] N. Jiang, M. Nishihara, and W. Lempert, "Quantitative NO_2 molecular tagging velocimetry at 500 kHz frame rate", Appl. Phys. Lett. 97, 221103, (2010).

[1.19] N. Jiang, M. Webster, W. Lempert, J. Miller, T. Meyer, C. Ivey, and P. Danehy, "MHz-rate nitric oxide planar laser-induced fluorescence imaging in a Mach 10 hypersonic wind tunnel", Appl. Opt. 5-, A20-A28 (2011).

[1.20] W. Lempert, P. Wu, B. Zhange, and R. Miles, "Pulse-burst laser system for high-speed flow diagnostics", AIAA, (1996).

[1.21] **http://www.edge-wave.de/**.

[1.22] A. Ellis and M. Fourney, "Application of a ruby laser to high-speed photography." Proceedings of the IEEE 51, 942-943, (1963).

[1.23] M. Slipchenko, T. Meyer, and S. Roy, "Advances in burst-mode laser diagnostics for reacting and nonreacting flows." Proceedings of the Combustion Institute, (2020).

[1.24] H. Bates, "Burst-Mode Frequency-Doubled YAG:Nd^{3+} Laser for Time-Sequenced High-Speed Photography and Holography." Appl. Opt. 12, 1172-1178, (1973).

[1.25] G. Massey, M. Jones, and J. Johnson, "Generation of Pulse Bursts at 212.8 nm by Intracavity Modulation of an Nd:YAG laser", IEEE Journal of Quantum Mechanics, Vol. QE-14, No. 7, (1978).

[1.26] J. Huntley, “High-speed laser speckle photography. Part 1: repetitively Q-sqitched ruby laser light source.” Optical Engineering 33, 1692-1699, (1994).

[1.27] J. Grace, P. Nebolsine, C. Goldey, G. Ghahal, J. Norby, and J. Heritier, “Repetitively pulsed ruby lasers as light sources for high-speed photography.” Optical Engineering 37, 2205-2212, (1998)

[1.28] C. Kaminski, J. Hult, and M. Aldén, “High repetition rate planar laser induced fluorescence of OH in a turbulent non-premixed flame.” Appl. Phys. B 68, 757-760, (1999).

[1.29] P. Wu and R. Miles, “High-energy pulse-burst laser system for megahertz-rate flow visualization.” Opt. Lett 25, 1639-1641 (2000).

[1.30] J. Luff, D. Mansfield, S. Zaidi, H. Aschoff, J. Kuper, and R. Miles, “Development of a tunable megahertz pulseburst alexandrite laser system.” AIAA Plasmadynamics and Lasers Conference, 2003-3746, (2003).

[1.31] B. Thurow, N. Jiang, M. Samimy, and W. Lempert, “Narrow-linewidth megahertz-rate pulse-burst laser for high-speed flow diagnostics”, Appl. Opt. **43**, 5064 (2004).

[1.32] B. Thurow and A. Satija, “Design of a MHz Repetition Rate Pulse Burst Laser System at Auburn University.” AIAA 2006-1384, (2006).

[1.33] N. Jiang and W. Lempert, “Ultrahigh-frame-rate nitric oxide planar laser-induced fluorescence imaging.” Opt. Lett. 33, 2236-2238, (2008).

[1.34] D. Hartog, N. Jiang, and W. Lempert, “A pulse-burst laser system for a high-repetition-rate Thomson scattering diagnostic.” Review of Scientific Instruments 79, 10E736, (2008).

[1.35] N. Jiang, M. Webster, and W. Lempert, “Advances in generation of high-repetition-rate burst mode laser output.” Appl. Opt. 48, B23-B31, (2009).

[1.36] B. Thurow, A. Satija, and K. Lynch, “Third-generation megahertz-rate pulse burst laser system.”, Appl. Opt. 48, 2086-2093, (2009).

[1.37] D. Hartog, J. Ambuel, M. Borchardt, J. Reusch, P. Robl, and Y. Yang, “Pulse-burst operation of standard Nd:YAG lasers.” Journal of Physics: Conference Series 227, (2009).

[1.38] W. Harris, D. Hartog, and N. Hurst, “Initial operation of a pulse-burst laser system for high-repetition-rate Thomson scattering.” Review of Scientific Instruments 81, 10D505, (2010).

[1.39] F. Fuest, M. Papageorge, W. Lempert, and J. Sutton, “Ultrahigh laser pulse energy and power generation at 10 kHz.”, Opt. Lett. 37, 3231-3233, (2012).

[1.40] M. Slipchenko, J. Miller, S. Roy, J. Gord, and T. Meyer, “Quasi-continuous burst-mode laser for high-speed planar imaging”, Opt. Lett. 37, 1346-1348, (2012).

[1.41] W. Young, L. Morton, E. Parke, and D. Hartog, “High-repetition-rate pulse-burst laser for Thomson scattering on the MST reversed-field pinch.” Journal of Instrumentation 8, C11013, (2013).

[1.42] M. Slipchenko, J. Miller, S. Roy, J. Gord, and T. Meyer, “All-diode-pumped quasi-continuous burst-mode laser for extended high-speed planar imaging.” Opt. Exp. 21, 681-689, (2013).

[1.43] S. Roy, J. Miller, M. Slipchenko, P. Hsu, J. Mance, and J. Gord, “100-ps-pulse-duration, 100-J burst-mode laser for kHz-MHz flow diagnostics.” Opt. Lett. 39, 6462-6465, (2014).

[1.44] M. Slipchenko, J. Miller, S. Roy, T. Meyer, J. Mance, and J. Gord, “100 kHz, 100 ms, 400 J burst-mode laser with dual-wavelength diode-pumped amplifiers.” Opt. Lett. 39, 4735-4738, (2014).

[1.45] J. Mance, M. Slipchenko, and S. Roy, “Regenerative amplification and bifurcations in a burst-mode Nd:YAG laser.” Opt. Lett. 40, 5093-5096, (2015).

[1.46] H. Pan, R. Yan, X. Li, X. Fa, Y. Ma, R. Fan, X. Yu, and D. Chen, “6.1 MW, 10 kHz Side-Pumped Burst-Mode Nd:YAG Laser.” Journal of Russian Laser Research 37, 259-264 (2016).

[1.47] W. Wu, X. Li, R. Yan, Y. Zhou, Y. Ma, R. Fan, Z. Dong, D. Chen, “100 kHz, 3.1 ns, 1.89 J cavity-dumped burst-mode Nd:YAG MOPA Laser.” Opt. Exp. 25, 26875-26884, (2017).

[1.48] R. Pan, U. Retzer, T. Werblinski, M. Slipchenko, T. Meyer, L. Zigan, and S. Will, “Generation of high-energy, kilohertz-rate narrowband tunable ultraviolet pulses using a burst-mode dye laser system.” Opt. Lett. 43, 1191-1194, (2018).

[1.49] S. Roy, N. Jiang, P. Hsu, T. Yi, M. Slipchenko, J. Felver, J. Estevadeordal, and J. Gord, “Development of a three-legged, high-speed, burst-mode laser system for simultaneous measurements of velocity and scalars in reacting flows.” Opt. Lett. 43, 2704-2707, (2018).

[1.50] J. Felver, M. Slipchenko, E. Braun, T. Meyer, and S. Roy, “High-energy laser pulses for extended duration megahertz-rate flow diagnostics.” Opt. Lett. 45, 4583-4586, (2020).

2. MODELING

In this chapter, a comprehensive Matlab model and direct comparisons to constructed hardware outputs are reported, followed by the demonstration of this hardware for advanced measurements. This chapter describes the unique approach of creating a single model applicable to all forms of burst-mode laser hardware.

2.1 Motivation

Computational modeling plays an important role in understanding physical phenomena across all scientific disciplines. Mathematical derived equations, assumptions, and logic can aptly describe the inner workings of many application-based prototypes and structures, like wind tunnels, turbines, compressors, engines, etc. Likewise, experimental probes and techniques attempt to explain these phenomena in real time and space. Both the models and experimental techniques have underlying sources of error and uncertainty, be they from incorrect assumptions, poor alignment, faulty equipment, etc. Using a tug-of-war concept, it is important that the models and experiments tug on each other to provide "checks" to help produce consistent results. Similar results improve confidence in the accuracy of the measurements.

In the realm of high-speed flows and combustion, applying physical probes, like thermocouples for temperature measurements, gas chromatographers for species concentration measurements, and pitot tubes for pressure measurements, can drastically affect the flow field. In supersonic and hypersonic flows, insertion of physical probes can generate shock waves, and in flames, these probes can displace the flow as well as catalytically react with sample species [2.1]. Higher fidelity results can be achieved by sampling these phenomena with nonintrusive measurements (i.e. laser diagnostics). While not immune to altering the flow (e.g. high energy deposition creating local perturbations in the flow), these nonintrusive measurements provide higher fidelity results than their intrusive counterparts.

In order to model the theoretical output of laser diagnostic techniques in these environments, characterization of the laser is imperative. For techniques like CARS, this is extremely important. The spectral bandwidth of the pump, Stokes, and probe beams, their temporal counterparts, and higher order spectral phase effects like chirp are driving factors for accurate modeling. Figure 2.1

elicits the general iterative process for solving for temperature. A two-beam room temperature RCARS setup is shown, and all parameters (probe delay, spectral bandwidths, pulse widths, beam quality, chirp, etc.) are recorded as data is taken. The experimental results are shown at the top in blue, and a theoretical fit from the bottom [2.2] is applied to it. If the fit has a high residual, parameters are altered and the fit is reapplied. Because temperature is obtained using a least-squares fitting routine to fit the experimental spectra with a phenomenological N_2 RCARS model, a single incorrect beam parameter could cause turmoil. In order to prevent an iterative guessing game for laser characteristics in the model, Figure 2.2 illustrates how burst-mode laser experimental and modeling results work together to create accurate laser characterization. By modeling the expected spectral bandwidth (top left), temporal pulse width (bottom left), energy output (top right), and spatial profile (bottom right), the experimental outputs can be confirmed to some degree and be used to adjust the model in an iterative process.

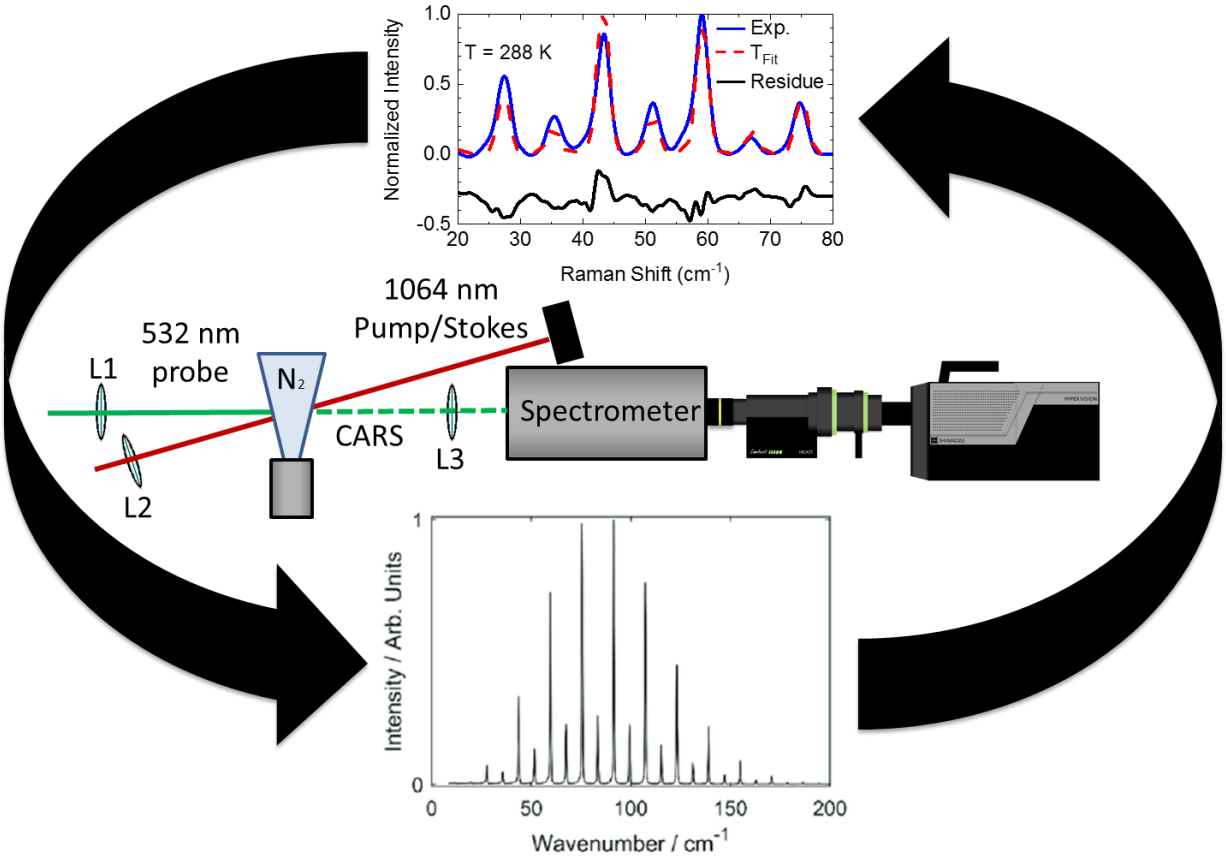

Figure 2.1. A two-beam room temperature RCARS setup is shown. If the fit has a high residual, parameters are altered and the fit is reapplied.

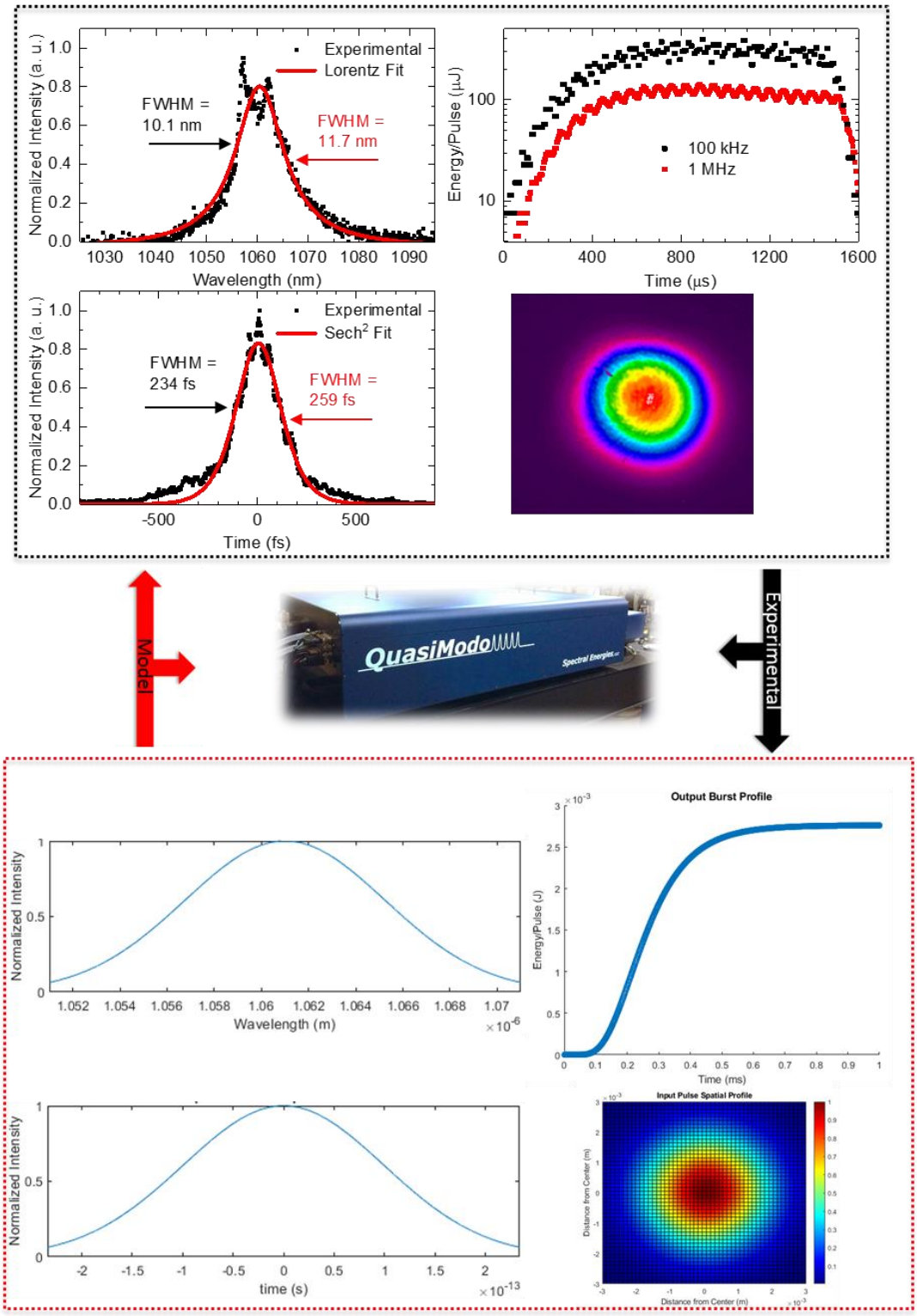

Figure 2.2. A representation of experimental results (black) and modeling results (red) working in tandem to characterize the burst-mode laser. In both dotted boxes: spectral bandwidth (top left), temporal pulse width (bottom left), energy output (top right), and spatial profile (bottom right)

2.2 Methodology

The ultimate goal of this code is to produce a graphic user interface (GUI) that can provide accurate results for burst-mode lasers already constructed, and as a predictive model for those being designed. The incorporation of different rod materials, spectral bandwidths, temporal pulse widths, beam spatial parameters, number of leg passes, and the burst-mode regime are all taken into consideration. Commented code can be found in Appendix A, and a step-by-step walkthrough of the outputs is employed. The code is tested by using constructed hardware outputs from multiple lasers to confirm its validity via output overlap.

The code begins with a series of prompts for the seed laser's central wavelength, spectral bandwidth, temporal pulse width, and beam diameter. Our ns laser from chapter 3 will be our representative hardware.

```
Let's build a laser! We will start with pulse input parameters.
Please enter your laser's central wavelength in meters: 1064.45E-9
Please enter the initial pulse width of your laser in seconds: 10E-9
Please enter the initial bandwidth of your laser in meters: .00167E-9
Please enter the intial beam diameter of your laser in meters: .002
```

The time_bandwidth_spatial function is called for the purpose of establishing input figures. The data sets are made into Gaussian lineshapes using Eq. 2.1, where Δx is the FWHM of the lineshape, x is the variable, and x_0 is the expected value.

$$f(x) = \frac{2}{\left(\frac{\Delta x}{2*sqrt(2*\ln(2))}\right)*sqrt(2\pi)} * \exp\left(-\frac{(x-x_0)^2}{2*\left(\frac{\Delta x}{2*sqrt(2*ln(2))}\right)^2}\right) \quad 2.1$$

While the temporal pulse lineshape could easily have been chosen to represent a $sech^2$ shape, Gaussian was chosen in the hopes of direct transform limited comparison in the future. The results of the input frequency and temporal beam characteristics can be seen in Figure 2.3, and the input beam spatial profile can be seen in Figure 2.4.

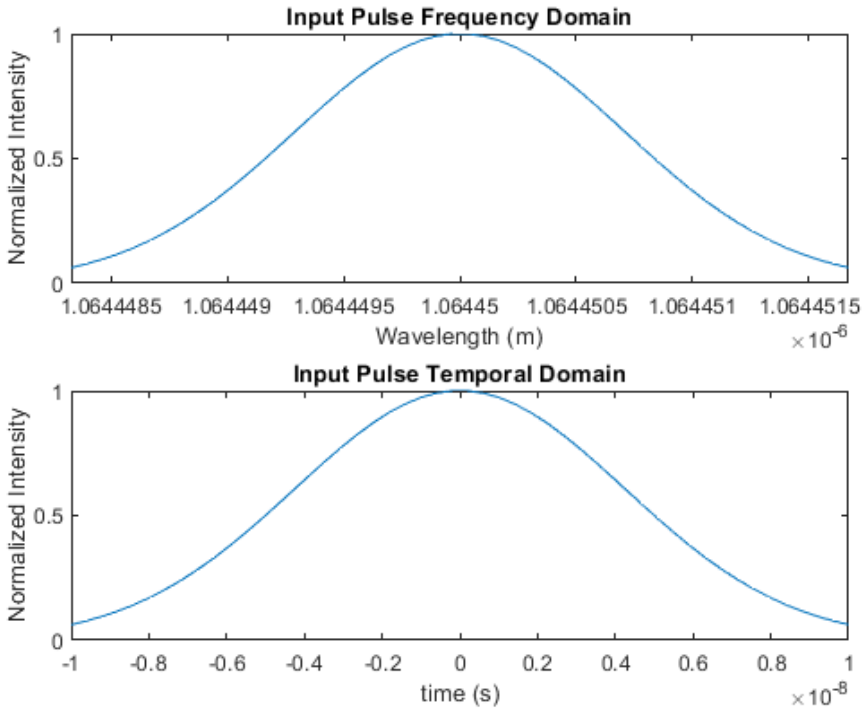

Figure 2.3. Input frequency and temporal domains for our beam set as Gaussian linewidths.

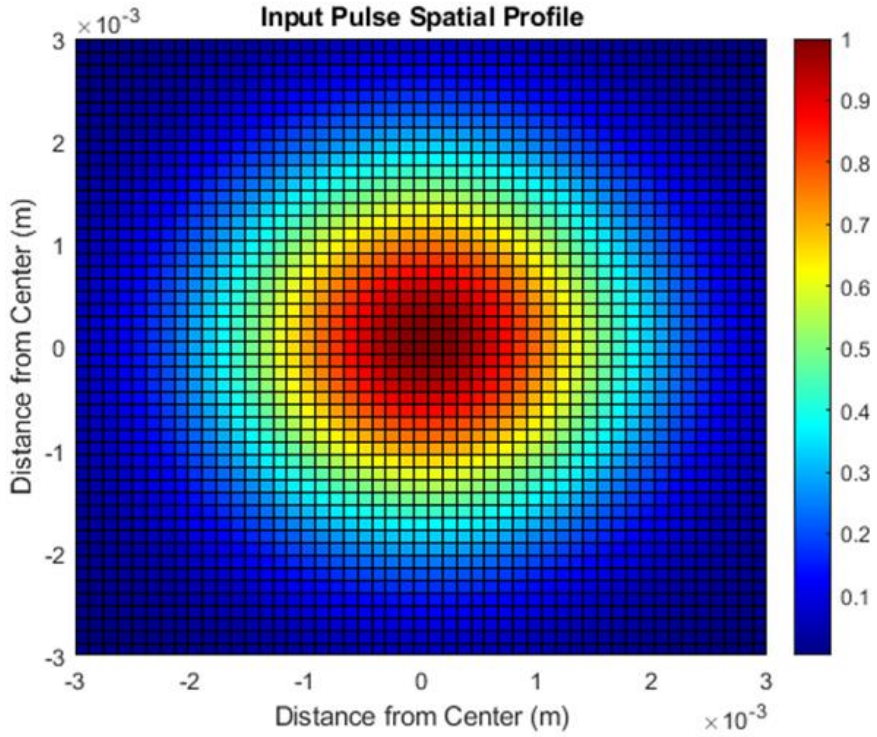

Figure 2.4. Input Gaussian beam spatial profile.

The system parameters are then requested, prompting for the system repetition rate, burst length, and average power.

```
Now we will need system parameters!
Please enter your repetition rate in Hz (e.g. 1 MHz = 1000000): 100000
Please enter your burst length in seconds: .01
Please enter your seed input power in Watts: .01
```

With the system parameters called, the total pulses and individual fluence per pulse are found. The fluence is broken up into a spectrum and corrected to represent the total fluence under the curve. Note that this can be done with fluence or energy. It was decided to go with fluence because it is consistent with literature, and because the spatial propagation through the system is not to a point in the code where the spatial domain needs to be calculated simultaneously with energy.

At this point, the beam is prepared to interact with any loss elements before the first leg. A loss element matrix is established, and a lot of effort is used to make sure the total loss element matrix can consistently be called upon and be accurate for each leg in the system. The code prompts for a loss element, and if there is one, will prompt for an OI, spatial filter, or PBS. Each of these loss elements have specifically been given loss values that have to be manually changed in the function. The code will keep prompting for additional loss elements until a 0 is pressed.

```
It is time to build the first leg of the laser!
Is there a loss element before your rod? Hit 1 for yes and 0 for no: 1
Enter 1 for OI, 2 for spatial_filter, or 3 for PBS: 3
You've chosen a PBS
Is there another loss element before your rod? Hit 1 for yes and 0 for no: 0
```

Now that the loss elements before the first leg in the system have been established, the code will prompt for information pertinent to the first rod in the first leg – rod diameter, small-signal gain, rod material (Nd:YAG or Nd:Glass), and rod length. For each property, a dummy variable will be used to establish the property for that leg. The code keeps track of legs by using cells containing the dummy variables for each leg. A leg counter, m, is also established. The small-signal gain is measured experimentally, and is represented as a function of time that emulates the rise-time of the power supplies, shown in Eq. 2.2. SSG_0 is the measured SSG, t is time, and τ is the time constant associated with rise time.

$$SSG = SSG_0 * \left(1 - \exp\left(-\frac{t}{\tau}\right)\right) \qquad 2.2$$

With the rod correctly implemented, the code will prompt for loss elements directly after this rod in the same fashion as how it prompted for loss elements before the first rod. The loss element added matrix is used at each point where loss elements are prompted. These matrices are added to the initial loss element matrix and update the total loss element matrix. If there are no loss elements, the matrix will form a row of 0's equal to the previous row. If there are fewer loss elements in the added matrix than the initial, 0's are added to the added matrix. If the opposite is true, then 0's are added to the first row until it is the same length as the added row.

The code will then ask if there is another rod in the system. If yes, essentially the same code runs, and then there will be a prompt for additional loss elements after that rod. This continues until the answer is no for another rod in the system. The rod count in the system is established with k. The loss element matrix is continually addressed to be the correct dimensions. The rod diameter, small-signal gain, rod material, and rod length dummy variables gain an additional row for each additional rod added to the leg.

```
Rod 1
Enter this rod's maximum small-signal-gain: 208
Enter 1 for Nd:YAG or 2 for q246 material properties for this rod: 1
Enter this rod's length in meters: .1
Enter this rod's diameter in meters: .003
Is there a loss element after your rod? Hit 1 for yes and 0 for no: 1
Enter 1 for OI, 2 for spatial_filter, or 3 for PBS: 2
You've chosen a spatial filter
Is there another loss element after your rod? Hit 1 for yes and 0 for no: 0
Is there another rod in the leg? Hit 1 for yes and 0 for no: 1

Rod 2
Enter this rod's maximum small-signal-gain: 208
Enter 1 for Nd:YAG or 2 for q246 material properties for this rod: 1
Enter this rod's length in meters: .1
Enter this rod's diameter in meters: .003
Is there a loss element after your rod? Hit 1 for yes and 0 for no: 0
This leg now has 2 rods
Is there another rod in the leg? Hit 1 for yes and 0 for no: 0
```

The rod diameter, small-signal gain, rod material, and rod length cells are updated to include the dummy matrices. The passes function is now called to determine if the leg is a single pass, double pass, or regenerative cavity, and to step through the burst to get output characteristics for the leg.

For the passes function, all necessary matrices and cells are created – rod gain bandwidth, saturation fluence, stored rod energy, Einstein coefficient, simulated emission cross section, total

output fluence, rod extraction efficiency, small-signal gain coefficient, output fluence, and input fluence. Next, material properties are called within the function, and a common wavelength vector is used to unite rods. This only changes the wavelength vector if the rods in the same leg are different materials (e.g. rod 1 is Nd:YAG and rod 2 is Nd:glass). Input fluence is altered based on the laser leg count. If this is the first leg, the input fluences have not had a seed bandwidth applied to their value, so it is applied. Later leg pulse fluences are taken as is since their fluence has wavelength dependence already incorporated.

The wavelength dependent saturation fluence and pumping power are created using Eq. 2.3 and 2.4, respectively. Here, h is Planck's constant, c is the speed of light in vacuum, λ_0 is the central wavelength of the material gain bandwidth, $\Delta\lambda$ is the rod gain bandwidth, and σ_{SE} is the material stimulated emission cross section.

$$E_s = \left(\frac{hc}{\lambda_0 \sigma_{SE}} \Delta\lambda_{rod}\right) * \frac{\frac{hc}{\lambda_0 \sigma_{SE}}}{\int \frac{hc}{\lambda_0 \sigma_{SE}} \Delta\lambda_{rod} d\lambda} \tag{2.3}$$

$$P = E_s A_{21} \ln(SSG) \tag{2.4}$$

At this point, the choice for single pass, double pass, or regenerative passing is implemented. The single pass option is listed first. A technique originally used by Park et al. is used for double passed legs with ns long pulses [2.3]. This technique is necessary and important for longer pulses because portions of the pulse fluence that interact with the rod first will actually double pass and extract energy from the rod before the later portion of the initial pulse fluence interacts with the rod. The input fluence is established and loss elements are applied to the input.

The front pass gain is is implmented with Eq. 2.5 and Eq. 2.6, where E_s is saturation fluence, E_0 is input fluence, and E_{stored} is stored fluence. For ns sources, these equations will essentially amount to the same thing. However, with broadband sources, they vary significantly, and Eq. 2.7 is necessary to lock the SSG at the correct amount while correctly implementing the bandwidth changes. The SSG coefficient is also established in Eq. 2.8 by relating the SSG to the length of the rod.

$$Gain_{dummy} = E_s * \ln\left(1 + \left(exp\left(\frac{E_0}{E_s}\right) - 1\right) * \exp\left(\frac{E_{stored,0}}{E_s}\right)\right. \tag{2.5}$$

$$Gain_{bandwidth} = E_s * \ln\left(1 + \left(exp\left(\frac{E_0}{E_s}\right) - 1\right) * \exp\left(\frac{E_{stored,0}}{E_s}\right) * bandwidth_{gain}\right. \tag{2.6}$$

$$Gain = Gain_{bandwidth} * \left(\frac{\int Gain_{dummy} d\lambda}{\int Gain_{bandwidth} d\lambda}\right) \quad 2.7$$

$$g_0 = \ln\left(\frac{SSG}{l_{rod}}\right) \quad 2.8$$

The total extraction efficiency, η, updated stored fluence, and updated SSG coefficient are displayed in Eq. 2.9-2.11 [2.4].

$$\eta = \frac{(\int Gain(\lambda) d\lambda - \int E_0(\lambda) d\lambda)}{g_0 * l_{rod} * \int E_s(\lambda) d\lambda} \quad 2.9$$

$$E_{stored}(t + \Delta t) = E_{stored}(t) \exp(-A_{21}\Delta t) + \frac{P}{A_{21}}[1 - \exp(-A_{21}\Delta t)] - E_{stored}(t)\eta \quad 2.10$$

$$g_1 = g_0 * (1 - \eta) \quad 2.11$$

These 3 equations are necessarily important for single passed amplifier legs because of the temporal domain count concept extraction energy from the rod. These are important equations for double passed and regnerative cavities because the pulses will continue to interact with the same rods and because of the temporal domain count concept.

The rod count is updated, and the input pulse fluence to the next rod is re-established as the current pulse fluence. If there are no more rods, loss elements after the final rod are incorporated, and the stored fluence in the rods is calculated using Eq. 2.10. Outputs for time and wavelength dependent fluence are cataloged.

The double pass logic is almost identical, and slices of the temporal pulse are sent through independently to simulate the earlier portions of the pulse extracting more fluence than the laer portions of the pulse. Note: As of now, the distances between rods and other optics have not been accounted for. It is assumed that the first portion of the pulse clears the entire leg before the next portion in time.

Since the regenerative operation has not been successfully added yet, that portion of the code will not be posted. The user is then prompted for more losses after the leg.

```
Is this a single-pass, double pass, or regen? Hit 1 for single, 2 for double, or 3 for regen: 2
Is there a loss element after this leg? Hit 1 for yes and 0 for no: 0
Is there another leg in the laser? Hit 1 for yes and 0 for no: 1
```

At this point, the user will be prompted for additional legs. If the case is such that there are additional legs, the logic is very similar to what was already displayed, and can be seen in Appendix A. If there are no additional legs, the outputs are collected in figure form.

2.3 Results

The model is directly compared to the constructed hardware from chapters 3 and 4. In chapter 3, a ns laser is constructed. The model is compared to the full power output at the fundamental wavelength at a repetition rate of 100 kHz. This repetition rate was chosen to eliminate ASE contributions. The temporal domain can be seen in Figure 2.5. The output pulse is clearly positively skewed, indicating the initial portions of the pulse extracted more energy than the latter portions of the pulse. Figure 2.6 displays the spectral domain. The input and output bandwidths are nearly identical due to the narrow spectral bandwidth and orders of magnitude larger gain bandwidth.

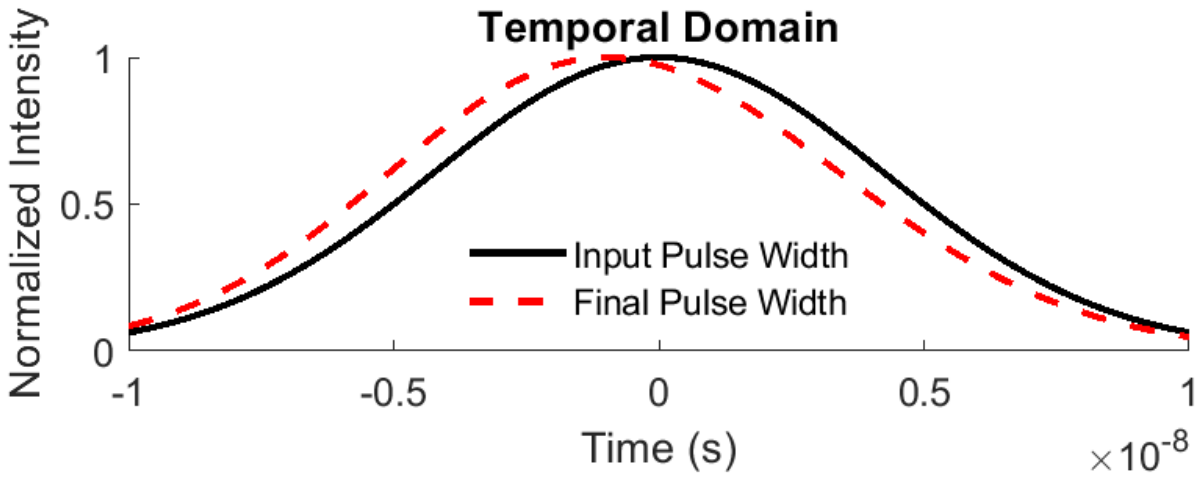

Figure 2.5. Temporal domain for the input seeded pulse and output amplified pulse for the ns system.

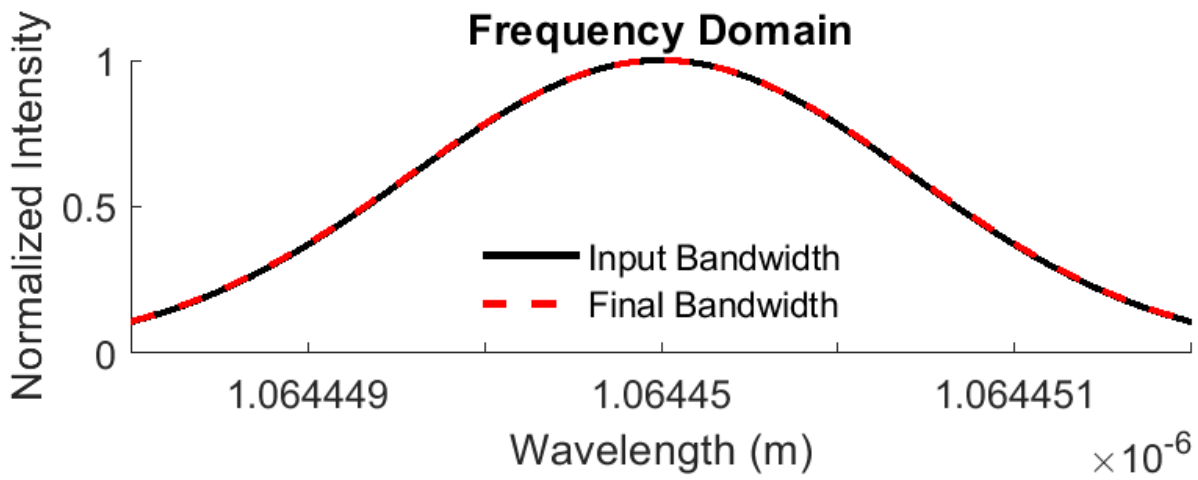

Figure 2.6. Frequency domain for the input seeded pulse and output amplified pulse for the ns system.

The experimental and computational energies per pulse are compared in Figure 2.7. The model predicts 23.4 mJ/pulse, while the experimental output is 14.1 mJ/pulse. The result is within a factor of 2, with sources of uncertainty deriving from mismeasurements of the small-signal gain, losses in the system, and input power. Dropping the small-signal gain to previously measured amounts results in a near perfect overlap.

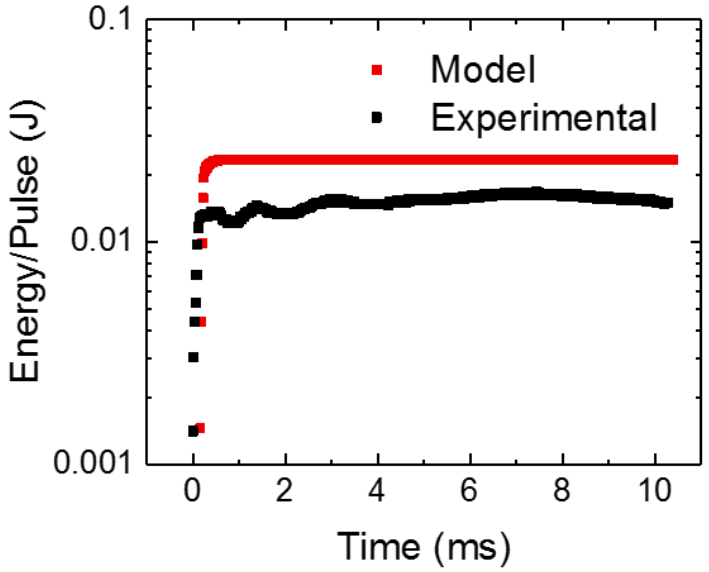

Figure 2.7. A comparison of computational and experimental energies per pulse for the ns laser.

The model is directly compared to the fs laser from chapter 4.1 instead of 4.3 since it contains only double passes and no quadruple passes. The model is compared to the full power output at the fundamental wavelength at a repetition rate of 1 MHz. This repetition rate was chosen because the power input measurements are more trustworthy (i.e. 100 kHz repetition rate pulses lost a lot of their initial energy by ASE filtration, so there is a higher chance of uncertainty). The temporal domain can be seen in Figure 2.8. The complete overlap in the temporal domain makes sense in this case because the pulses are short enough to not affect latter portions of themselves like the ns pulse, and a temporal stretching physics package for the rods was not implemented. Figure 2.9 shows the spectral domain of the pulse. Since the gain bandwidth is centered at 1062 nm, the 1064.6 nm central wavelength seed has its bandwidth shifted to 1062.4 nm. The FWHM of the modeled bandwidth is 9 nm, compared to the experimental value of 10.1 nm. This offset is attributed to unaccounted for nonlinear spectral phase components.

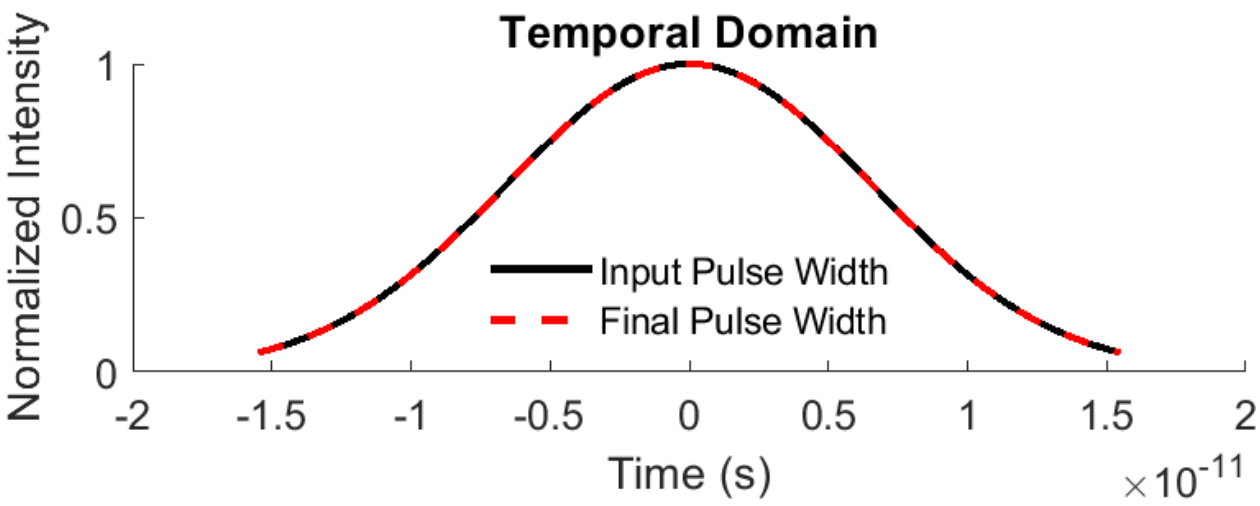

Figure 2.8. Temporal domain for the input seeded pulse and output amplified pulse for the ns system.

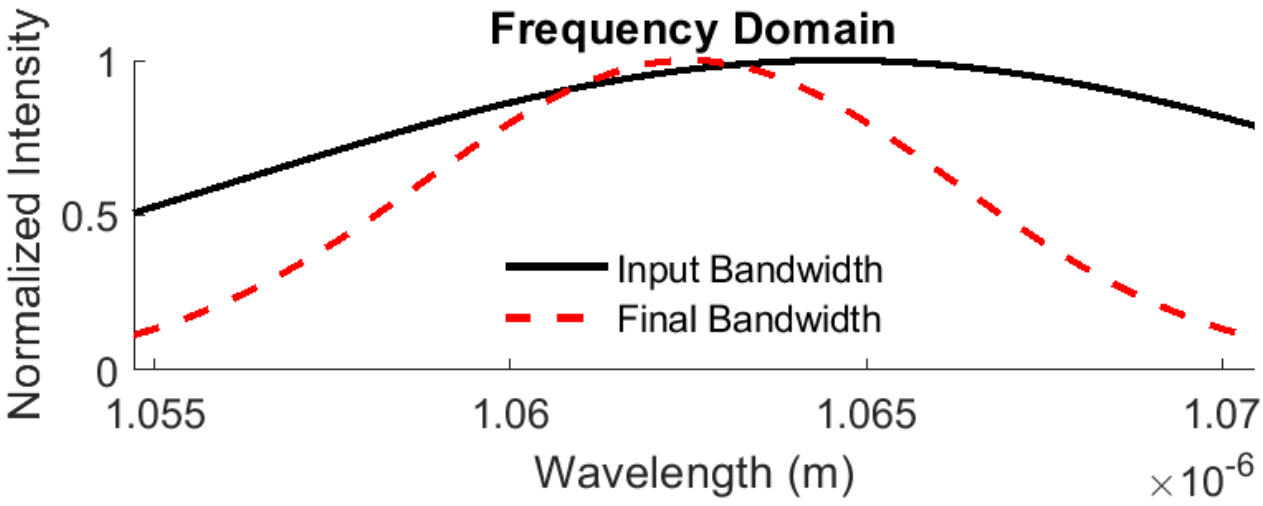

Figure 2.9. Frequency domain for the input seeded pulse and output amplified pulse for the ns system.

The experimental and computational energies per pulse are compared in Figure 2.10. The experimental energy is 117 μJ/pulse, and the modeled energy is 119 μJ/pulse, a 1.7% difference. Uncertainty arises from improperly measured small-signal gain, since a value differential of approximately .01 for each rod would overlap them perfectly.

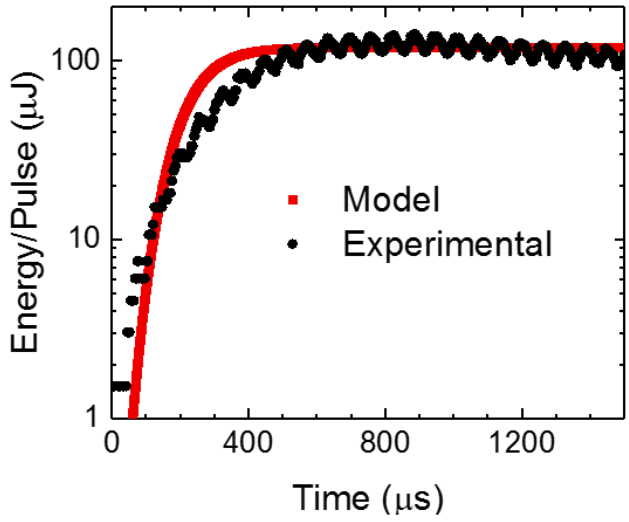

Figure 2.10. A comparison of computational and experimental energies per pulse for the fs laser.

2.4 References

[2.1] F. Xing, Y. Huang, M. Zhao, and J. Zhao, “The Brief Introduction of Different Laser Diagnostics Methods Used in Aeroengine Combustion Research.” Journal of Censors, (2016).

[2.2] A. Hosseinnia, “On the Use of Rotational CARS on Polyatomics and in Time Domain.” Dissertation, Lund University, (2020).

[2.3] D. Park, J. Jeong, and T. Yu, “Optimization of the pulse width and injection time in a double-pass laser amplifier.” High Power Laser Science and Engineering **6**, (2018).

[2.4] W. Koechner, *Solid-State Laser Engineering*, 4th Ed. (Springer Berlin, 1996).

3. NANOSECOND BURST-MODE LASER DEVELOPMENT

M. Smyser, K. Rahman, M. Slipchenko, S. Roy, and T. Meyer, "Compact burst-mode Nd: YAG laser for kHz-MHz bandwidth velocity and species measurements", Opt. Lett. **43**, 735-738 (2018).

In this chapter, ns burst-mode advancements are reported on, which date from 2016 to 2020 at Purdue University. Publications used in this chapter are listed above.

3.1 Background

Spatial and temporal resolution are important factors in the analysis of high-speed, stochastic, and dynamic processes in fluid mechanics, combustion, energetics, and other technical applications. Burst-mode lasers have played a key role in advancing state-of-the-art measurements of such processes by providing high-energy laser pulses at very high repetition rates [3.1]. This has allowed ultra-high-speed (1 MHz) short duration (0.1–1 ms) planar measurements of flowfield parameters using techniques such as filtered Rayleigh scattering [3.2], Doppler velocimetry [3.3], and laser-induced fluorescence (LIF) [3.4]. Longer duration (1–100 ms) measurements at 10–100 kHz have been made using LIF [3.5], laser-induced incandescence (LII) [3.6], particle image velocimetry (PIV) [3.7],[3.8], and picosecond coherent anti-Stokes Raman scattering (CARS) [3.9]. The high pulse energies of burst-mode lasers have also been used for planar Rayleigh scattering [3.10], planar Raman scattering [3.11], simultaneous LIF and PIV [3.12], dual-species LIF [3.13], and three-dimensional tomographic imaging [3.14]-[3.16]. Such measurements take advantage of high mode quality for reliable beam propagation and focusing, laser operation with multiple output harmonics, and different pulse patterns such as pulse doublets for tracking high-speed flows.

Despite the high pulse energies and flexible operation available with burst-mode lasers, ongoing challenges include large system size and cost, which can limit implementation to only a few major research facilities. This is due, in part, to the power electronics and long amplification chains needed to generate the burst. Multiple amplification chains are required to amplify a few nanojoules per pulse from the seed source up to tens or hundreds of millijoules per pulse levels. The amplification of a single chain can be increased using a regenerative approach or using multiple passes, but such high gain can result in energy bifurcation because of the long lifetime of

the Nd:YAG excited state [3.17]. The use of a solid-state, high-pulse-energy oscillator would reduce the gain requirements [3.18], but such oscillators have no flexibility in the generation of a pulse train. Therefore, the development of a compact, efficient, and versatile burst-mode laser for kHz–MHz bandwidth is limited by the high small-signal gain, which causes the system to lase spontaneously, while the small footprint complicates the use of spatial filters or active optical gating elements.

3.2 Results

Reported is a compact architecture with significantly reduced complexity that utilizes a directly modulated laser diode followed by a high-energy fiber amplifier and folded power amplifier design to achieve a robust and versatile kHz–MHz burst-mode laser system. At the lowest repetition rate, the system generates a sequence of 50 pulse singlets or doublets in a 10 ms burst with a total energy of 2.5 J/burst at 1064 nm. This is equivalent to over 50 mJ in each pulse singlet or doublet. At 1 MHz, the total energy increases to 14 J/burst at 1064 nm, equivalent to 1.4 mJ in each of 10,000 pulse singlets or doublets. System performance such as mode quality, shot-to-shot stability, and second harmonic conversion efficiency are investigated over this very wide range of operation. We further assess the utility of pulse singlets at 1064 nm for detection of soot volume fraction using LII and pulse doublets at 532 nm for measurements of planar velocity at kHz–MHz rates.

An alternative to burst-mode lasers is the diode-pumped solid-state (DPSS) laser architecture, which is limited by thermal loading because it operates on a continuous duty cycle. As such, an average power of 1.4 kW would be required to achieve similar energies per pulse as targeted in this work. Such high average powers are two to three times larger than one of the largest commercially available lasers of this kind used for laser diagnostics (e.g., EdgeWave HD-Series) [3.19]. In addition, such lasers are typically limited to a much smaller range of operating frequencies and output wavelengths.

A schematic of the compact burst-mode laser is shown in Figure 3.1. A continuous pulse train at 5–1000 kHz repetition rates with pulse widths of 5–10 ns and 2 GHz spectral bandwidth is produced using a directly modulated diode at 1064.4 nm. The pulsed output is pre-amplified with an Ytterbium fiber amplifier with a large core fiber (30 dB gain, 12.5-μm-core-diameter). The beam is initially expanded and transmitted through an optical isolator, which utilizes Faraday

rotation to prevent damage to the fiber by back-propagating beams. The power amplification system is comprised of three flash-lamp-pumped Nd:YAG modules with 101.6 mm long cavities. Multi-pass Amplifiers 1 and 2 contain 3-mm-diameter rods, while single-pass amplifier 3 contains a 4-mm-diameter rod. The rods are cut at a slight 1-degree angle to prevent self-lasing. In between amplifiers 1 and 2, a spatial filter is installed to prevent self-lensing due to amplified spontaneous emission (ASE).

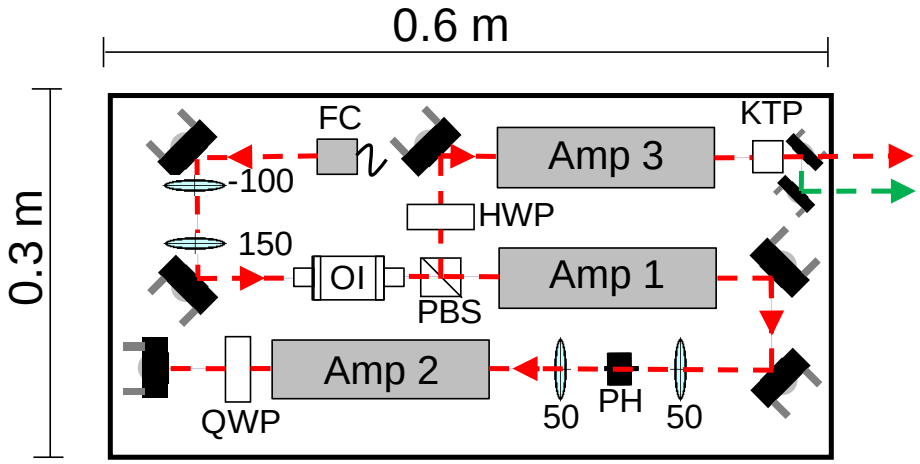

Figure 3.1. Compact burst-mode laser system. Red lines for 1064 nm path and green line for 532-nm path. Lens focal lengths of 50, 100, and 150 mm. QWP, quarter-wave plate; OI, optical isolator; PH, 50-µm pinhole; HWP, half-wave plate; PBS; polarizing beam splitter; KTP, second harmonic crystal; FC, fiber collimator.

The polarization of the light is then tuned with a half-wave plate for efficient second harmonic generation before passing through amplifier 3. It is then frequency-doubled with an 8 mm long Type II KTP crystal, separated with a dichroic mirror, and emitted through wall ports in the exterior of the 0.3×0.6 m^2 system. This footprint is three times smaller than a compact, 0.6×0.9 m^2 design previously reported by Slipchenko et al. using hybrid diode-pump/flashlamp-pump amplification stages with a similar maximum burst energy at the fundamental wavelength [3.5].

The burst-mode laser was characterized at repetition rates of 5–1000 kHz for 10 ms burst durations, as summarized in Figure 3.2. For repetition rates below 75 kHz, Figure 3.2a shows that there was considerable ASE originating from the fiber amplifier and from amplifiers 1 and 2. Additional measures to suppress ASE such as an electro-optic modulator (EOM) and spatial filtering were avoided to maintain the simplicity and compact footprint of the laser. Hence, the

ASE limited the laser output to ~2.5 J/burst at 5 kHz even as the flashlamp energy was increased. At 75 kHz and beyond, the ASE was minimal and the laser was able to produce 14.1 J per burst at 1064 nm with the highest electrical energy of 990 J. Figure 3.2Figure 3.2b shows the calculated energy per pulse at 1064 nm for a range of repetition rates and three pumping conditions. After frequency conversion to 532 nm, the energies per burst and per pulse are shown in Figure 3.2c and d, respectively. The second harmonic conversion efficiency, shown in Figure 3.2e, exceeded 40% for 10 kHz repetition rates but dropped to below 30% at 100 kHz and beyond due to the lower per pulse energies. The results for pulse doublets used for PIV are shown in Figure 3.2f, with 11.75 mJ and 1.13 mJ per pulse at 10 kHz and 100 kHz, respectively. At 200 kHz and beyond, similar pulse energies can be achieved in pulse singlets while maintaining the short inter-pulse spacing needed for PIV.

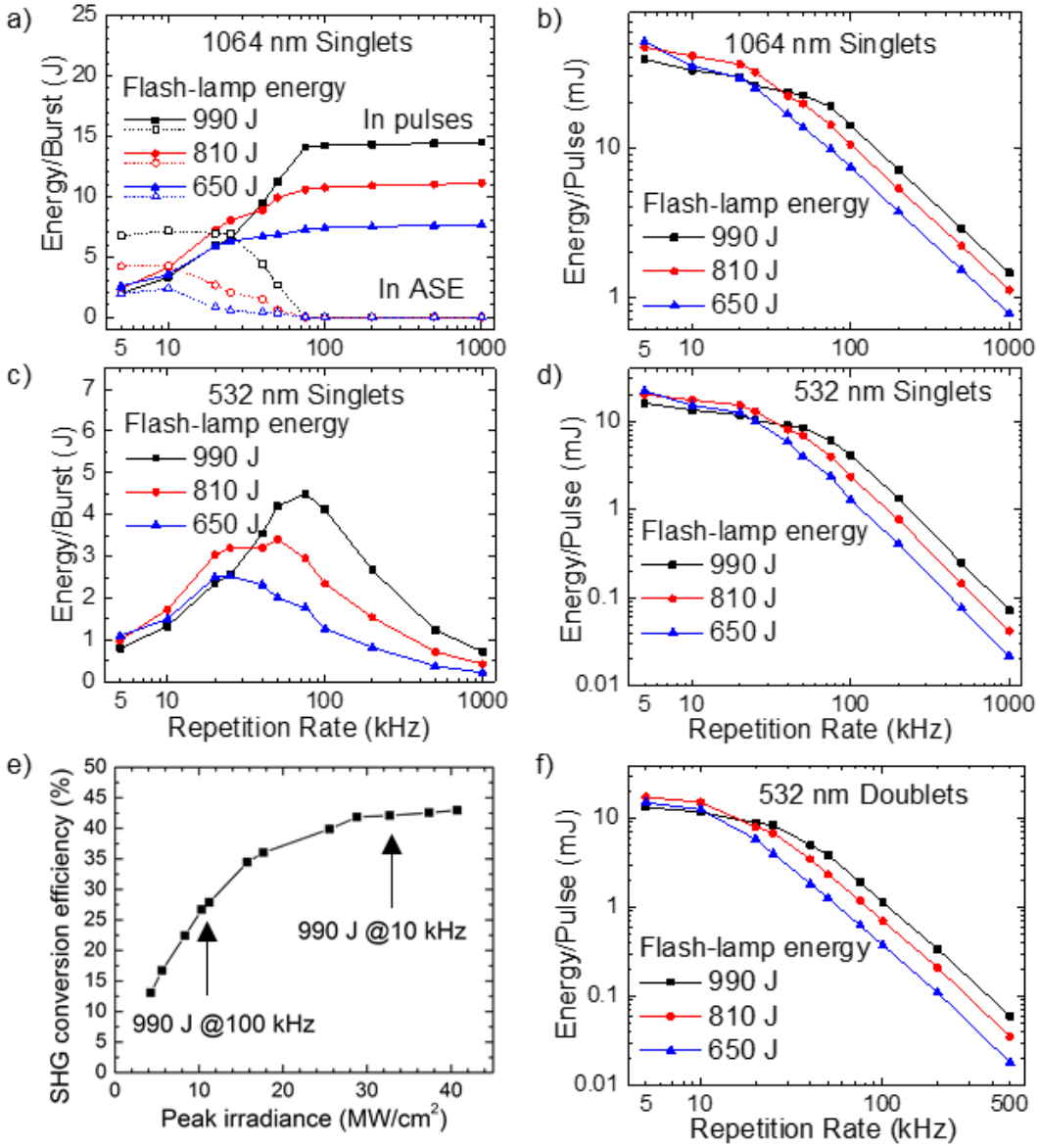

Figure 3.2. Laser characterization: (a) Fundamental mode energies per burst in singlets, (b) resultant energies per pulse, (c) second harmonic generation (SHG) energies per burst in singlets, (d) resultant energies per pulse, (e) SHG conversion efficiency, and (f) energies per pulse for second harmonic doublets.

The quality of the beam was also documented, as shown in the near-field (0.05 m) and far-field (2 m) beam profiles of Figure 3.3a and b, respectively. It is evidenced by the far-field image that there is a slight astigmatic divergence. The quality of the beam, M^2, was measured in both the *x*- and *y*-directions. The laser beam was transmitted through a 100-mm focal-length lens and a

series of beam profiles were acquired along the optical axis to take D4σ beam diameter measurements [3.20]. The beam profiler was moved via a micrometer stage for accurate measurements. The results can be seen in Figure 3.3c, with the resulting M^2 values for the x- and y-directions being 2.22 and 2.29, respectively. The beam spatial shape is near Gaussian with some wings visible in the far field. While the energy per pulse changes for different repetition rates, the spatial beam profile does not depend on repetition rate, temporal pulse shape, or doublet inter-pulse time interval for a given flash lamp energy, burst duration, and burst period.

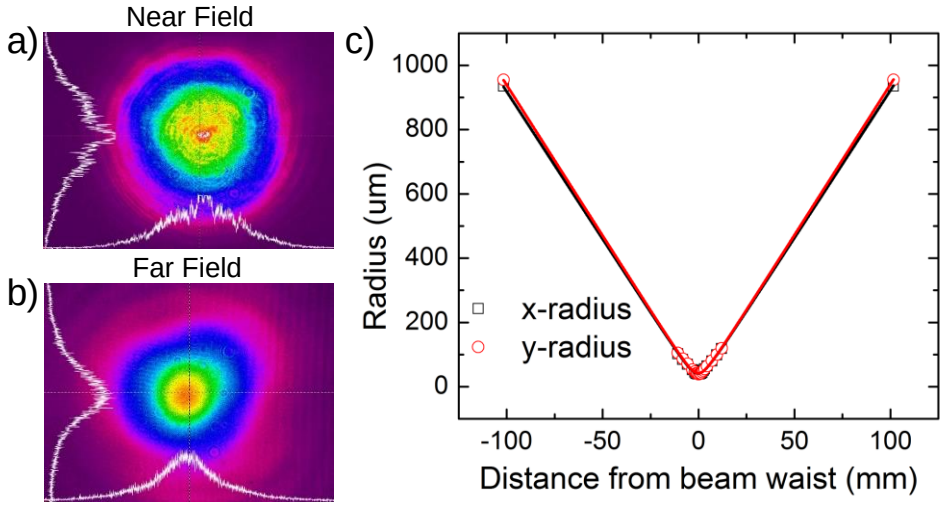

Figure 3.3. Beam quality: (a) near-field burst profile, (b) far-field burst profile, and (c) divergence profiles of the burst-mode laser in the x- and y-directions. M^2 = 2.22 and 2.29, respectively.

As noted earlier, PIV techniques require a pair of images separated by a short time interval for velocity calculations. As a result of finite energy stored in the Nd:YAG amplifiers, the second pulse within a doublet experiences less gain, and the decrease of the gain is larger at lower repetition rates due to higher pulse energies. Different amounts of energy per pulse in a doublet complicates image analysis. To help equalize the doublet energies, the intensity and pulse width of each pulse was adjusted, as shown in Figure 3.4. This was enabled by using a pulse diode with a pulse-following current driver for the seed source, which generates the current pulses with constant peak current and duration equal to the trigger pulse duration.

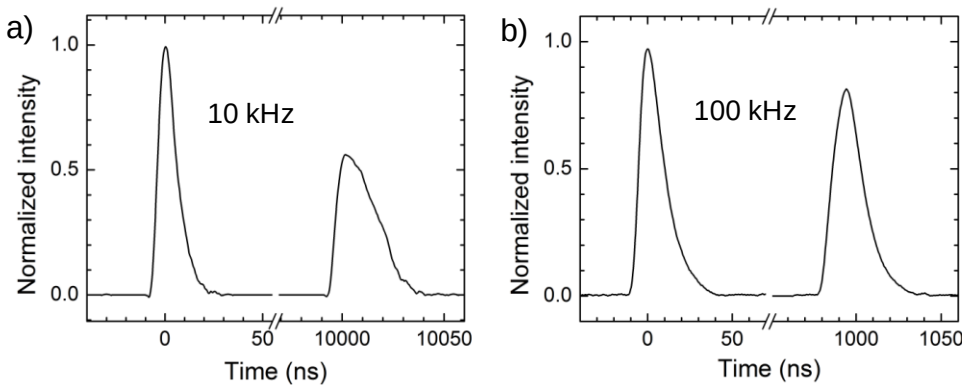

Figure 3.4. Intensity profiles of 532 nm doublet pulses at 990 J electrical energy for (a) 10 kHz and (b) 100 kHz repetition rates.

The width of the second pulse was controlled until both pulses provided the same energy, which was measured by a CMOS camera. Unlike conventional PIV lasers, the two pulses within a doublet are automatically collinear, eliminating potential misalignment, and they have the same polarization and reflection characteristics. Temporal profiles for 10 and 100 kHz doublets are shown in Figure 3.4a and b, respectively.

Figure 3.5 illustrates the burst profiles at 10 kHz and 100 kHz, with good pulse-to-pulse uniformity and constant pulse energies throughout the bursts. Over the 10 ms burst, the 100 kHz pulse energy has a standard deviation of 0.121 mJ (7%) for the first pulse and 0.124 mJ (7.1%) for the second pulse. For the 10 kHz burst profile, the pulse energy has a standard deviation of 2.16 mJ for the first pulse and 0.922 mJ for the second pulse (17.5% and 7.5% of the mean, respectively). The larger deviation in the peak pulse intensity for the 10 kHz burst is likely due to ASE related gain defects, whereas there is little ASE contribution when the laser is operated at 100 kHz (see Figure 3.2a). The similar standard deviations and the overlap of data points between the first and second pulses in Figure 3.5 indicates excellent pulse-to-pulse uniformity for use in particle scattering or incandescence measurements, especially at high repetition rates.

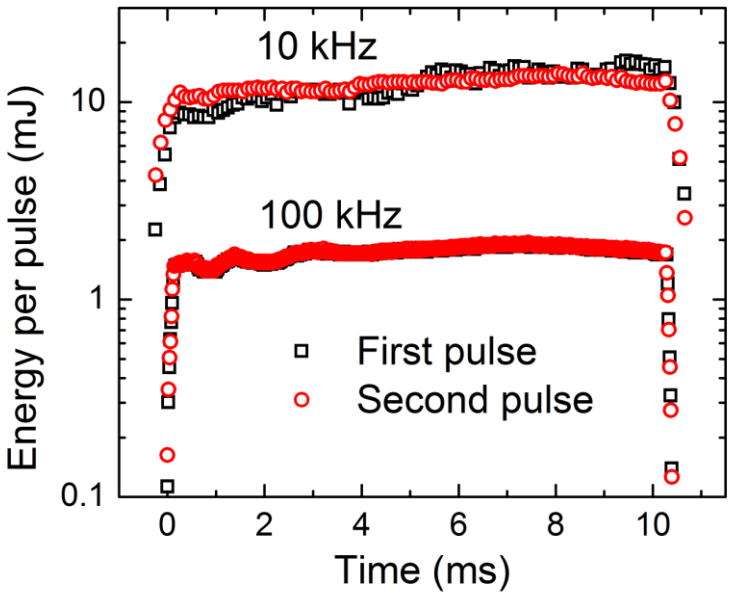

Figure 3.5. Doublet burst profiles over 10 ms duration at 532 nm.

For the PIV experiment, particles were seeded into an air jet with a 6.4-mm-diameter nozzle and a Reynolds number of 57,700 at the nozzle exit, which was well within the turbulent flow regime. An f = +1000 mm spherical lens and an f = -50 mm cylindrical lens were used to produce a vertical laser sheet of 37-mm-height and 200-µm-width to illuminate the field of view located 1.7 mm above the nozzle exit. 100 kHz pulse doublets with 0.8 mJ/pulse at 532 nm were then used generate a pair of particle scattering images, as shown in Figure 3.6a and b, that were recorded on a CMOS camera (Photron, SA-Z) operating at 200 kHz. The scattering images exemplify a high degree of repeatability in the laser sheet's temporal and spatial energy distributions. The flow velocity was computed using a temporal spacing of 2 µs between each pair of images, and the particle displacement was measured using standard cross-correlation procedures (LaVision, DaVis 8.3). A sample of 3 out of 1000 images from a 100 kHz sequence of two-dimensional distributions of the flow velocity are shown in Figure 3.6c to e, with calculated uncertainties of 1% in the core flow and 3–4% at the edges. As the 37 mm sheet height is much larger than needed for the 9 mm field of view, it is estimated that similar uncertainties can be achieved using pulse singlets up to 500 kHz with the same 2 µs spacing between images for turbulence spectra measurements [3.21]. At lower repetition rates (~10–50 kHz), the laser energies are sufficient for three-dimensional tomographic PIV [3.22].

For the LII experiment, the laser was operated at a 100 kHz repetition rate with pulse singlets at 1064 nm to illuminate soot particles within a turbulent methane-air jet diffusion flame (Reynolds number of 6500). An f = +500 mm spherical lens and an f = -25 mm cylindrical lens were used to produce a vertical laser sheet of 50-mm-height and 800-μm-width with a fluence of 0.037 J/cm^2 at 1064 nm. This fluence was selected based on prior work [3.6] to induce heating and incandescence of soot particles at rates up to 100 kHz without significantly altering the soot properties from shot to shot. As such, the LII signal can be related to the soot volume fraction within the flame. The same CMOS camera was used with a high-speed intensifier (HS-IRO, LaVision) to capture the LII signal with a 70 ns gate to minimize natural flame emission in the images. A partial sequence from 1000 LII images collected at 100 kHz with a mean ratio of signal to background noise of 60 is shown in Figure 3.7. The nearly identical signals in the flame from one image to the next (with a standard deviation of 4% on average) indicates the high accuracy of the measurement. With proper normalization, this can provide detailed measurements of the soot volume fraction. By reducing the sheet height, measurement rates exceeding that of prior work at 100 kHz are also feasible [3.6].

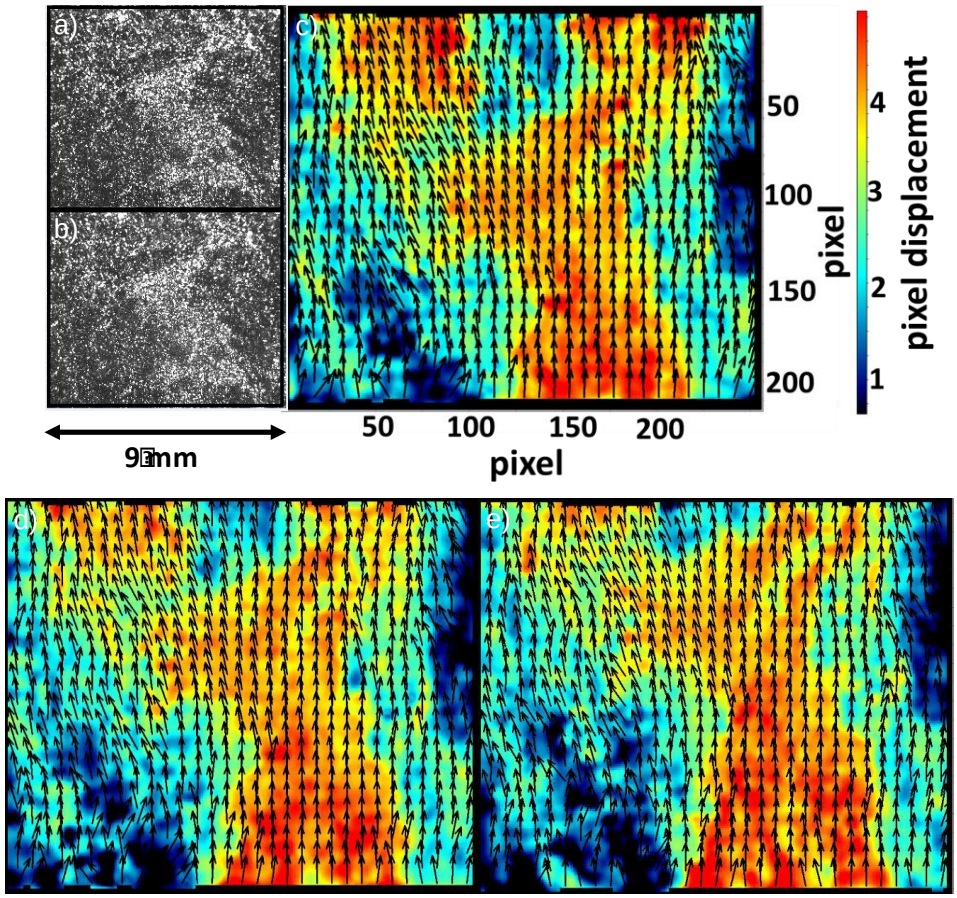

Figure 3.6. PIV of a free jet seeded with micron sized Di-Ethyl-Hexyl-Sebacate (DEHS) particles: raw images of (a) first and (b) second pulses in a doublet, (c) corresponding vector field from the pair of images, and (d) and (e) successive vector fields at 100 kHz.

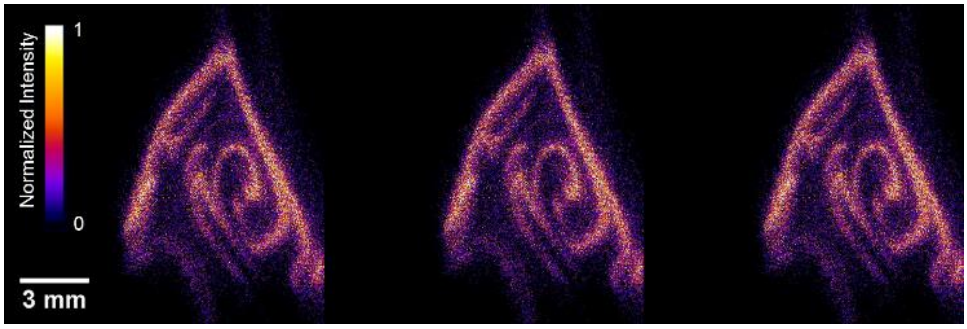

Figure 3.7. Partial sequence of 100 kHz laser-induced incandescence images of soot volume fraction in a wrinkled jet diffusion flame.

In conclusion, a simplified burst-mode laser architecture with a 0.18 m^2 footprint has been demonstrated to produce sufficient pulse energy, mode quality, and pulse-to-pulse stability for accurate measurements of velocity and species with kHz–MHz bandwidth for a duration up to 10 ms. The design allows for flexible use of the fundamental 1064 nm or frequency doubled 532 nm output, along with custom pulse patterns such as doublets or singlets for use in various measurement techniques. Future improvements of this laser architecture include pumping of a tunable source, extension to UV wavelengths, and use of shorter pulse widths to enhance the second-harmonic generation efficiency.

3.3 References

[3.1] B. Thurow, N. Jiang, and W. Lempert, "Review of ultra-high repetition rate laser diagnostics for fluid dynamic measurements," Meas. Sci. Technol. **24**, 1 (2013).

[3.2] P. Wu, W. R. Lempert, and R. B. Miles, "Megahertz pulse-burst laser and visualization of shock-wave/boundary-layer interaction," AIAA J. **38**, 672 (2000).

[3.3] B. Thurow, N. Jiang, M. Samimy, and W. Lempert, "Narrow-linewidth megahertz-rate pulse-burst laser for high-speed flow diagnostics," Appl. Opt. **43**, 5064 (2004).

[3.4] N. Jiang, M. Webster, W. R. Lempert, J. D. Miller, T. R. Meyer, C. B. Ivey, and P. M. Danehy, "MHz-rate nitric oxide planar laser-induced fluorescence imagine in a Mach 10 hypersonic wind tunnel," Appl. Opt. **50**, A20 (2011).

[3.5] M. N. Slipchenko, J. D. Miller, S. Roy, J. R. Gord, S. A. Danczyk, and T. R. Meyer, "Quasi-continuous burst-mode laser for high-speed planar imaging," Opt. Lett. **37**, 1346 (2012).

[3.6] J. B. Michael, P. Venkateswaran, C. R. Shaddix, and T. R. Meyer, "Effects of repetitive pulsing on multi-kHz planar laser-induced incandescence imaging in laminar and turbulent flames," Appl. Opt. **54**, 3331 (2015).

[3.7] J. D. Miller, N. Jiang, M. N. Slipchenko, J. G. Mance, T. R Meyer, S. Roy, and J. R. Gord, "Spatiotemporal analysis of turbulent jets enabled by 100-kHz, 100-ms burst-mode particle image velocimetry," Exp. Fluids **57**, 192 (2016).

[3.8] S. Beresh, S. Kearney, J. Wagner, D. Guildenbecher, J. Henfling, R. Spillers, B. Pruett, N. Jiang, M. Slipchenko, and J. Mance, "Pulse-burst PIV in a high-speed wind tunnel," Meas. Sci. Technol. **26**, 095305 (2015).

[3.9] S. Roy, P. S. Hsu, N. Jiang, M. N. Slipchenko, and J. R. Gord, "100-kHz-rate gas-phase thermometry using 100-ps pulses from a burst-mode laser," Opt. Lett. **40**, 5125 (2015).

[3.10] M. J. Papageorge, T. A. McManus, F. Fuest, and J. A. Sutton, "Recent advances in high-speed planar Rayleigh scattering in turbulent jets and flames: increased record lengths, acquisition rates, and image quality," Appl. Phys. B **115**, 197 (2014).

[3.11] N. Jiang, P. S. Hsu, J. G. Mance, Y. Wu, M. Gragston, Z. Zhang, J. D. Miller, J. R. Gord, and S. Roy, "High-speed 2D Raman imaging at elevated pressures," Opt. Lett. **42**, 3678 (2017).

[3.12] J. D. Miller, J. B. Michael, M. N. Slipchenko, S. Roy, T. R. Meyer, and J. R. Gord, "Simultaneous high-speed planar imaging of mixture fraction and velocity using a burst-mode laser," Appl. Phys. B **113**, 93 (2013).

[3.13] Z. Li, J. Rosell, M. Aldén, and M. Richter, "Simultaneous Burst Imaging of Dual Species Using Planar Laser-Induced Fluorescence at 50 kHz in Turbulent Premixed Flames," Appl. Spectrosc. **71**, 1363 (2017).

[3.14] B. R. Halls, J. R. Gord, T. R. Meyer, D. J. Thul, M. Slipchenko, and S. Roy, "20-kHz-rate three-dimensional tomographic imaging of the concentration field in a turbulent jet," Proc. Combust. Inst. **36**, 4611 (2017).

[3.15] B. R. Halls, P. S. Hsu, N. Jiang, E. S. Legge, J. J. Felver, M. N. Slipchenko, S. Roy, T. R. Meyer, and J. R. Gord, "kHz-rate four-dimensional fluorescence tomography using an ultraviolet-tunable narrowband burst-mode optical parametric oscillator," Optica **4**, 897 (2017).

[3.16] T. R. Meyer, B. R. Halls, N. Jiang, M. N. Slipchenko, S. Roy, and J. R. Gord, "High-speed, three-dimensional tomographic laser-induced incandescence imaging of soot volume fraction in turbulent flames," Opt. Express **24**, 29547 (2016).

[3.17] J. G. Mance, M. N. Slipchenko, and S. Roy, "Regenerative amplification and bifurcations in a burst-mode Nd: YAG laser," Opt. Lett. **40**, 5093 (2015).

[3.18] F. Fuest, M. J. Papageorge, W. R. Lempert, and J. A. Sutton, "Ultrahigh laser pulse energy and power generation at 10 kHz," Opt. Lett. **37**, 3231 (2012).

[3.19] http://www.edge-wave.de/.

[3.20] T. F. Johnston, "Beam propagation (M^2) measurement made as easy as it gets: the four-cuts method," Appl. Opt. **37**, 4840 (1998).

[3.21] S. J. Beresh, J. Henfling, and R. Spillers, “Postage-stamp PIV: small velocity fields at 400 kHz for turbulence spectra measurements,” AIAA Paper, 2017-0024 (2017).

[3.22] B. Coriton and J. H. Frank, “High-speed tomographic PIV measurements of strain rate intermittency and clustering in turbulent partially-premixed jet flames,” Proc. Combust. Inst. **35**, 1243 (2015).

4. ULTRAFAST BURST-MODE LASER DEVELOPMENT

M. E. Smyser, M. N. Slipchenko, T. R. Meyer, A. W. Caswell, and S. Roy, "Burst-mode laser architecture for the generation of high-peak-power MHz-rate femtosecond pulses," OSA Cont. **2**, 3490-3498 (2019).

J. M. Fisher, M. E. Smyser, M. N. Slipchenko, S. Roy, and T. R. Meyer, "Burst-mode femtosecond laser electronic excitation tagging for kHz-MHz seedless velocimetry," Opt. Lett. **45**, 335-338 (2020).

M. E. Smyser, E. L. Braun, V. Athmanathan, M. N. Slipchenko, S. Roy, and T. R. Meyer, "Dual-output fs/ps burst-mode laser for MHz-rate rotational coherent anti-Stokes Raman scattering." Opt. Lett. **45**, 5933-5936, (2020).

In this chapter, ultrafast (fs and ps) burst-mode laser advancements are reported on, which date from 2016 to 2020 at Purdue University. Publications used in this chapter are listed above.

4.1 Femtosecond Burst-Mode Laser

4.1.1 Background

Recent advances in burst-mode laser technologies have enabled kHz-rate velocity, temperature, and species concentration measurements using similar per pulse energies as high-power 10 Hz Nd:YAG lasers. This has allowed 100 kHz to MHz measurements in high-speed flows using techniques such as filtered Rayleigh scattering [4.1], Doppler velocimetry[4.2], laser-induced fluorescence (LIF) [4.3], particle image velocimetry (PIV) [4.4]-[4.7], laser-induced incandescence (LII) [4.8], and picosecond coherent anti-Stokes Raman scattering (CARS) [4.9] for burst durations up to 100 ms. Despite advances in per pulse energy, burst duration, repetition rate, and diversity of diagnostics, there have been challenges with reducing the temporal pulse width of these lasers from ns and ps to fs. Transform-limited master oscillators producing ns–ps pulses at the fundamental wavelength of 1064 nm have corresponding bandwidths that fit within the gain bandwidth of common power amplifiers such as Nd:YAG, allowing ns and ps pulses to be amplified [4.10]. However, the narrow spectral gain of Nd:YAG, while producing larger amplification, cannot provide the bandwidth required for fs pulse durations needed for extending nonlinear techniques such as fs two-photon laser-induced fluorescence (TP-LIF), fs/ps CARS, and fs laser electronic excitation tagging (FLEET) to similar rates of 100 kHz and higher.

Commercially available fs laser sources can operate at mJ/pulse energy levels for continuous pulsing at rates of 1–10 kHz with <100 fs pulse widths by using Ti:Sapphire regenerative amplifiers. Typical peak powers of the order 100 GW have been used for a range of nonlinear diagnostic techniques such as TP-LIF, CARS, and FLEET. In highly transient flows and many propulsion applications, however, rates of 1–10 kHz are not fast enough to capture the flow dynamics of key parameters such as velocity, temperature, and concentration of atomic and molecular species.

Commercial fs lasers based on fiber amplifiers are capable of operation at rates beyond 100 kHz and can achieve up to ~50 μJ/pulse at 1 MHz [4.11],[4.12]. With pulse widths ~500 fs, such fiber lasers can achieve somewhat low peak powers of ~100 MW, and the relatively long pulse widths limit spectral bandwidths to ~5 nm in the near infrared. Research on scaling up per pulse energy has led to development of multichannel fiber lasers with up to 16 channels and up to four pulse replicas per channel [4.13],[4.14]. While such lasers can produce MHz-rate fs pulses with mJ/pulse levels, they are relatively complex and have similar spectral bandwidth limitations, as do fs lasers based on thin-disk amplifiers [4.15],[4.16]. Shorter pulses and higher peak powers, driven by interest in attosecond science, have recently been achieved but require nonlinear compression techniques [4.17]. Moreover, outputting mJ/pulse energies at MHz rates continuously requires kW laser systems, which entails expensive multi-kW power diode pumping and complicated thermal management.

In contrast, laser systems based on the master-oscillator power-amplifier (MOPA) burst-mode architecture are available that have much higher energies per pulse at 100 kHz to MHz repetition rates compared to continuously pulsed lasers of similar average power because of low duty cycle operation [4.18]. As such, the burst-mode laser architecture has enabled a variety of ultra-high-speed measurements in dynamic flows with repetition rates beyond that achievable with conventional ns–ps sources [4.1]-[4.9]. To overcome the limited gain bandwidth of Nd:YAG-based amplifiers, as noted earlier, we report on a burst-mode system based on an Nd:glass amplifying medium. This new approach extends the MOPA burst-mode laser architecture to the generation of 100 kHz to 1 MHz fs laser pulse sequences at the fundamental wavelength of 1064.6 nm.

At the lowest repetition rate of 100 kHz, the current system generates a sequence of 100 pulses, each with an energy of ~290 μJ. At a pulse width of 234 fs, the peak power of 1.24 GW is

an order of magnitude higher than that achieved by high-power commercial fiber lasers at similar repetition rates [4.11],[4.12]. At 1 MHz, the energy per pulse of about 117 μJ represents a peak power of 0.5 GW for each pulse in a sequence of 1000 pulses. While not the highest peak power reported for a fs laser [4.13],[4.14], this approach results in a spectral bandwidth that is nearly twice that of other reported systems without nonlinear compression [4.11]-[4.15] while providing higher peak power than commercial fs fiber lasers at orders of magnitude lower average power for reduced complexity. System characteristics such as mode quality, shot-to-shot stability throughout the burst, beam profile, amplified spontaneous emission (ASE) minimization, and time-bandwidth attributes are investigated and reported.

4.1.2 Results

A diagram of the front end for the fs burst-mode laser is shown in Figure 4.1. The initial pulses are generated with a mode-locked fs fiber seed source at 50 MHz (Mendocino, Calmar Laser), which also acts as an RF master oscillator for the laser system. The seed source has an initial average power of 40 mW and a spectral bandwidth of 20 nm full-width at half-maximum (FWHM) centered at 1064.6 nm. The uncompressed seed pulses are ~4 ps long. The output of the seed is first gated with a fiber-coupled acousto-optic modulator (AOM1 in Figure 4.1, 150 MHz, 80 ns rise time, Brimrose) to produce a desired repetition rate of 100 kHz to 1 MHz. The AOM is synchronized with the seed through the delay generator (Quantum Composer, 9530 Series), which is phase-locked to the seed source. Because of the long rise time of AOM1, four pulses are gated out at set repetition rates. The pulses are passed through a preamplification stage consisting of a large-mode-area (25 μm core), broadband, Ytterbium fiber amplifier (Nuphoton, NP4000CO-RS-PM-37-4700-COLL-01). The gain of the fiber amplifier is optimized to minimize ASE contribution, which can dominate the output at high gain because of the low input seed power of about 1 mW at 1 MHz and 0.1 mW at 100 kHz. The fiber amplifier total gain is optimized by altering the driver current until the largest difference between ASE and total output is found. At optimal conditions, the fiber amplifier is operating in the unsaturated regime, and output powers of 150 mW (70% ASE) and 350 mW (30% ASE) are achieved at 100 kHz and 1 MHz, respectively. Based on the total fiber length and dispersion, the temporal duration of the laser pulse out of the fiber amplifier is calculated to be ~13 ps and the maximum output power is limited by the fiber damage threshold.

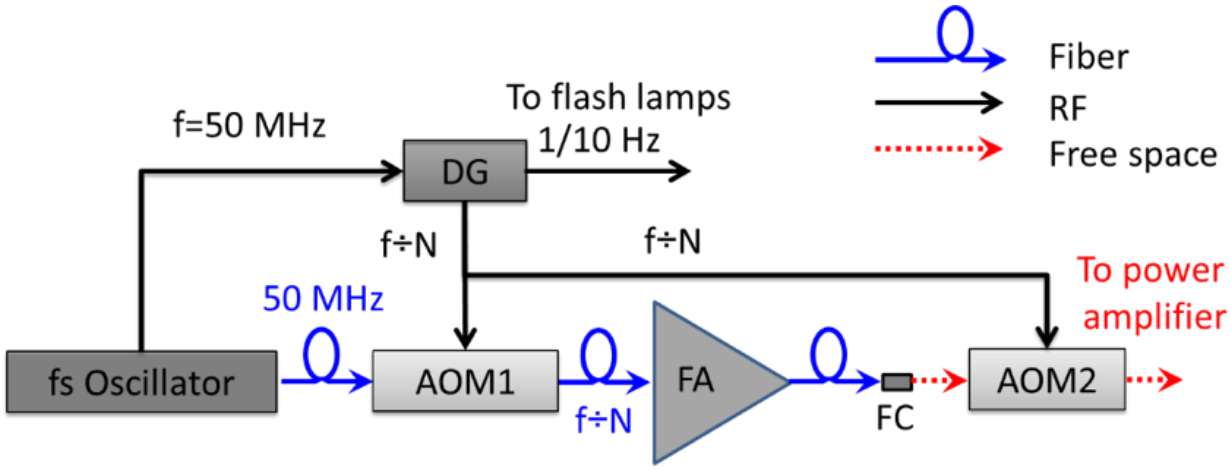

Figure 4.1. Electro-optic logic diagram. DG, delay generator; AOM, acousto-optic modulator; FA, fiber amplifier; FC, fiber collimator.

After fiber amplification, pulses are sent through the free-space power amplifier system shown in Figure 4.2. The pulses are collimated with a fiber collimator (FC, Thorlabs, C220TME-1064) and sent through an optical isolator (OI) to protect the fiber amplifier from back-propagating light. Then, the polarization of the pulses is tuned with a half-wave plate (HWP) for optimal AOM efficiency and sent through a free-space AOM (389 MHz, 4 ns rise time, Gooch and Housego), which is synchronized to the seed source via a delay generator. This AOM (AOM2 in Figure 4.1 and Figure 4.2) gates out a single pulse via first order diffraction at the desired repetition rate and has a total efficiency of 16%. AOM2 also removes fiber amplifier ASE background from the pulse train. After AOM2, the beam is polarization tuned again and reflected off a polarizing beam splitter (PBS). This allows for input energy adjustment before the free-space Nd:glass amplifying stages. The resultant beam is sent through a one-to-one spatial filter to improve beam quality and block scattering light from the AOM2 zeroth order beam.

The spatially filtered beam passes through an OI for ASE suppression in the power amplifier and to avoid feedback, and is double-passed through the first free-space amplification chain. The chain consists of two amplifiers, a one-to-one spatial filter, and a quarter-wave plate (QWP). As the beam double-passes through the QWP, the polarization is rotated 90˚ and the beam is reflected by the PBS.

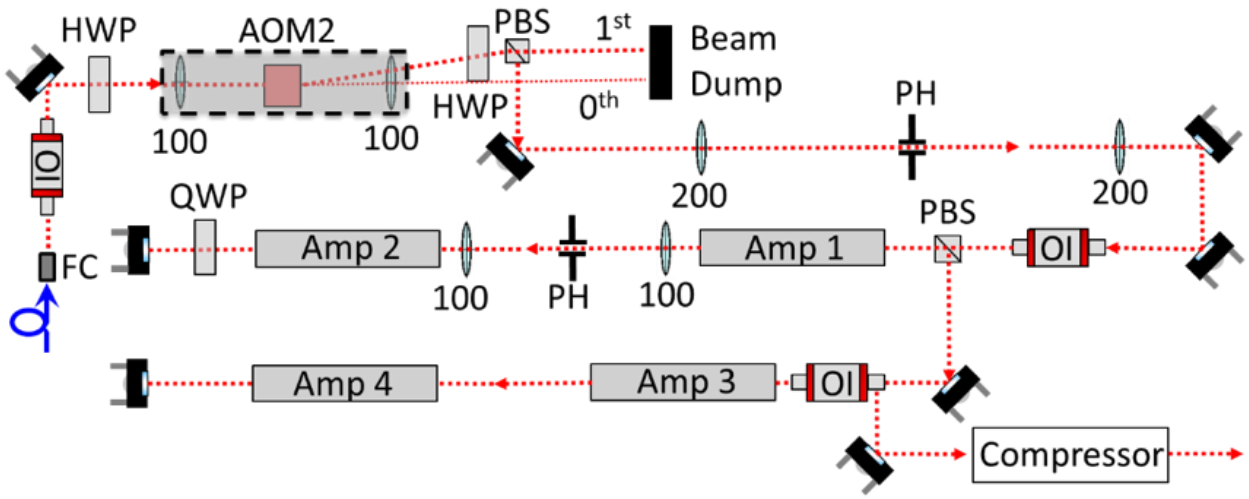

Figure 4.2. Free-space optical layout with f = 100 and 200 mm lenses. OI, optical isolator; HWP, half-wave plate; PBS, polarizing beam splitter; 0th, zeroth order beam; 1st, first order beam; PH, pinhole; QWP, quarter-wave plate. System size is 30 × 120 cm^2.

The beam is then double-passed through a second amplification chain, composed of an OI and two amplifiers. The OI is used to reduce ASE build-up and prevent feedback. Amplifiers 1-4 (IR Sources, Inc) are flashlamp pumped Q-246 Nd:glass (L3 Kigre, Inc.). The beam has a polarization extinction ratio (PER) of 21 dB. Note that in an attempt to maximize energy extraction, the second amplification chain initially had a QWP after amplifier 4 to try and quadruple pass amplifiers 1 and 2. However, this resulted in self-lasing, and the output was entirely ASE. After amplification, the beam is temporally compressed with two reflective diffraction gratings (1200 g/mm, 26˚ 44′blaze angle, Thorlabs). The compressor has an efficiency of 41%. With no amplification, total losses in the system are 90.2%. Major losses arise from the first spatial filter (21%) and second spatial filter (40% per pass). The measured input of the system is after the PBS following AOM2, and the measured output is after the compressor.

The spectrally broad gain of the Q-246 medium maintains the fs pulse characteristics throughout the amplification process, but at a cost of total small-signal gain, shown in Figure 4.3. The small-signal gain is measured near the maximum of the gain of Nd:glass using a narrowband ns pulsed source at 1064.4 nm. A ns laser is used to obtain peak small-signal gain for the central wavelength of the fs seed source. The first amplification chain has 3 mm diameter rods with lengths of 100 mm pumped by smaller energy flashlamps, while the second amplification chain has larger 4 mm diameter rods with lengths of 100 mm pumped by higher energy flashlamps to maintain

similar maximum small signal gain. Using 125 J electrical energy with the smaller rod setup, the small-signal gain reaches nearly 4.5 at a peak wavelength in the system, while the larger rod setup and 176 J electrical energy produces a small-signal gain ~5. By comparison, for the same pumping rate, Nd:YAG small-signal gain is around two orders of magnitude higher but is bandwidth limited and cannot be used for generating fs pulses.

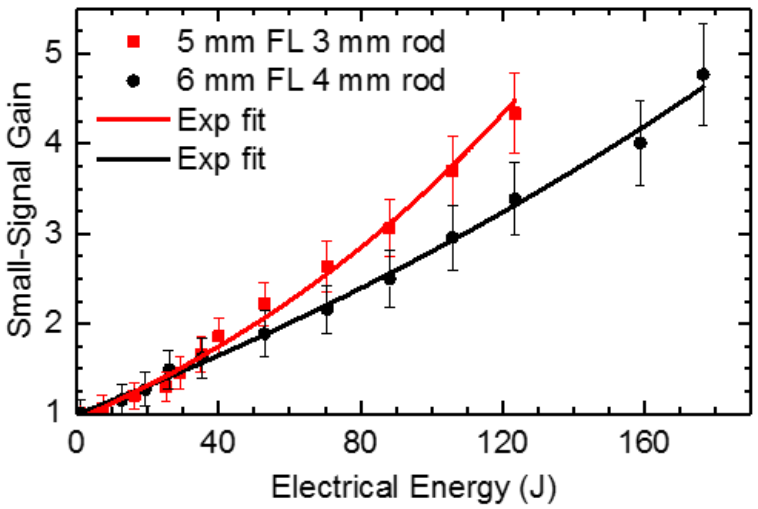

Figure 4.3. Single-pass small-signal gain measurements for different combinations of flashlamp diameters and rod diameters for Q-246 Nd:glass. Exponential growth fits are shown with R^2 = 0.998 for 5 mm flashlamps and 0.996 for 6 mm flashlamps.

The power amplifier total gain is characterized at 100 kHz and 1 MHz repetition rates for effective burst lengths of 1 ms (the flashlamps are fired for 1.5 ms to account for a 500 μs gain build up time), and the results are shown in Figure 4.4. For both repetition rates, the seed energy per pulse is tuned with the HWP, and the input energy is measured directly after the PBS. The maximum input energy per pulse is greater for 100 kHz due to lower repetition rates experiencing higher gain through the fiber preamplification stage. The maximum gain in the power amplifier is about 4000 and 3000 for 100 kHz and 1 MHz, respectively. A linear increase of output energy to input seed energy indicates that the system is operating in the small-signal gain regime. The 100 kHz repetition rate maintains this linear increase for all measured inputs, but the 1 MHz repetition rate starts to taper off indicating energy extraction from the rods.

At 100 kHz, the highest energy output is 290 μJ/pulse. Incorporating the losses in the system, 8 rod passes, and linear operation (small-signal gain regime), the effective small-signal

gain can be back calculated (averaged between the different sized rods) and is about 3.75. This recalculated small signal gain is inconsistent with the measured peak small-signal gain shown in Figure 4.3. This difference arises from the broadband pulse bandwidth, so the overall ratio of total energy post-amplification to preamplification is smaller than the narrowband 1064 nm small-signal gain.

The highest energy outputs for 100 kHz and 1 MHz repetition rates are acquired with flashlamp electrical energies at 125 J and 176 J for 5 mm and 6 mm diameter flashlamps, respectively. This energy output per pulse is calculated by subtracting the energy during the 500 μs gain build-up time and dividing the remaining energy by the number of remaining pulses. The overall ASE in the system is below the detection limit of 0.05 mJ/burst of the power meter head, and the maximum electrical energy for 1.5 ms burst duration is limited by the flashlamp damage threshold. The flash lamp damage threshold can be mitigated by reducing the overall burst length but at the penalty of limiting burst duration.

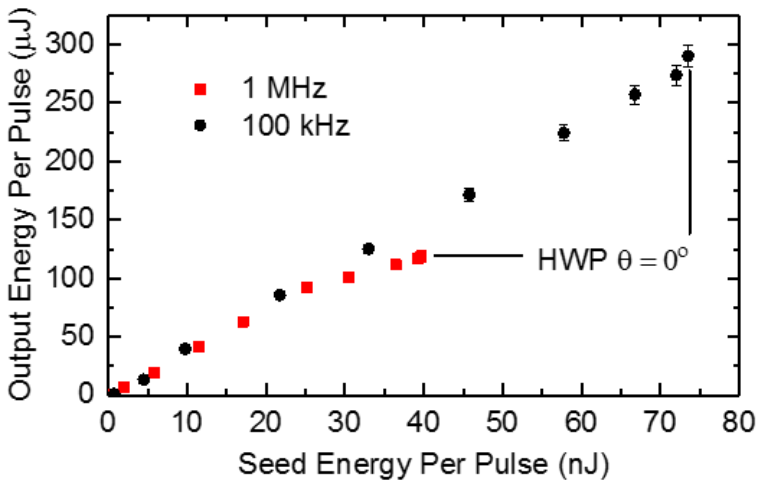

Figure 4.4. Dependence of power amplifier pulse energy output on the energy inputs at 100 kHz and 1 MHz repetition rates. HWP angle rotations from 0-45 degrees in increments of 5 degrees are used to generate different energy inputs.

Current system peak irradiance at the center portion of the beam at the output is 50 GW/cm^2 and 20 GW/cm^2 for 100 kHz and 1 MHz, respectively. The calculated B-integral for the current system is estimated by the B-integral through the last pass through the last rod of amplification, and is 0.27 and 0.11 for 100 kHz and 1 MHz, respectively. Self-focusing does not become a risk until the B-integral is greater than 1. If the system B-integral approaches 1, the pulses could be

stretched further in time prior to amplification for an additional safety factor. Hence, the current laser architecture can easily be scaled to even higher energies, although the current laser energies are already in a range that are sufficient for FLEET [4.19] and CARS [4.20],[4.21] signal generation at 100 kHz to MHz rates.

The total electrical energy per 1.5 ms burst is 600 J, while operation at every 10 seconds results in an average electrical power of 60 W. Figure 4.5 illustrates the pulse energy profiles in the burst at 100 kHz and 1 MHz. These profiles are measured with a photodiode (coupled with optical density filters) placed in the path of the beam. Over the 1 ms portion of the fully amplified pulses in the burst, the 100 kHz pulse energy has a standard deviation of 46.7 μJ (16.1% of the mean), and the MHz-rate pulse energy has a standard deviation of 11.3 μJ (9.7% of the mean). The oscillations are traced to the fiber amplifier and tentatively attributed to the onset of nonlinear optical effects in the fiber.

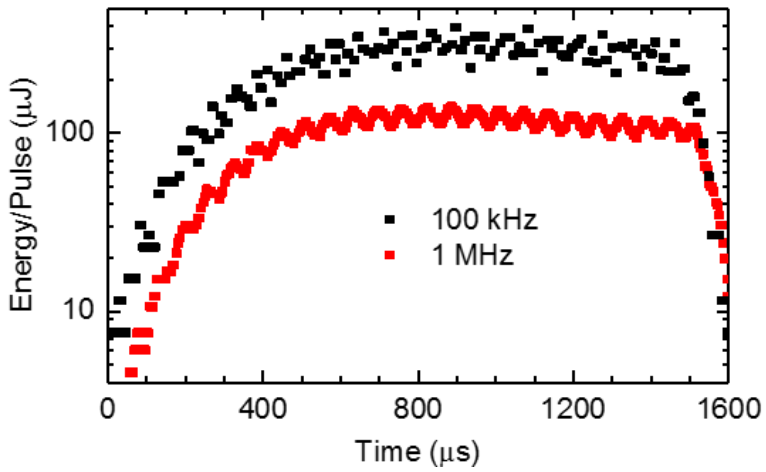

Figure 4.5. Burst profiles over a 1.5 ms duration for 100 kHz and 1 MHz.

The quality of the beam, M^2, is measured using time-averaged beam profile measurements from whole bursts (1.5 ms, 1 MHz repetition rate, and 117 μJ/pulse for the last 1 ms of the bursts) in the x and y directions, as shown in the near field and far field before temporal compression in Figure 4.6a and b, respectively. The laser beam is transmitted through a 50 mm focal length lens, and beam profiles are acquired along the optical axis for D4σ beam diameter measurements [4.22]. The results can be seen in Figure 4.6c, with resulting M^2 values for the x and y directions being

1.53 and 1.45, respectively. The overall beam spatial shape is circular with beam diameters around 1.7 mm in the x and y directions.

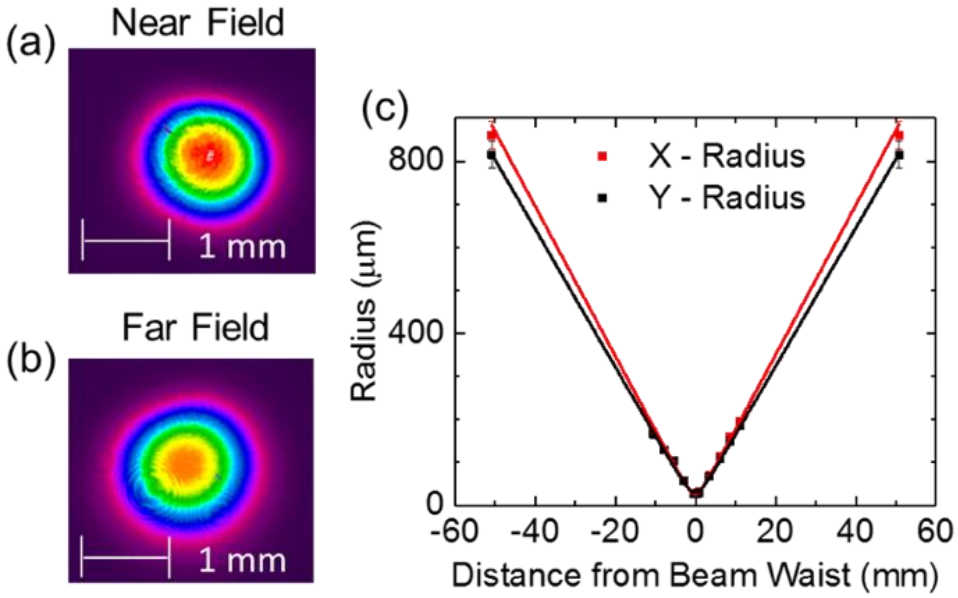

Figure 4.6. (a) Near field and (b) far field spatial beam profiles. (c) Divergence profiles of the burst-mode laser in the x and y directions before compression with M^2 = 1.53 and 1.45, respectively.

The time-averaged pulse widths and bandwidths of the temporally compressed beam are characterized and the results are shown in Figure 4.7. Both measurements were done with 1.5 ms bursts, 1 MHz repetition rate, and 117 μJ/pulse for the last 1 ms of the bursts. The bandwidth, shown in Figure 4.7a, is found using a spectrometer (Mightex, HRS-Series) with FWHM of 10.1 nm (89.8 cm^{-1}) centered at 1061 ±1 nm. The shift away from the central 1064.6 nm peak of the seed source is to be expected since Q-246 has a gain bandwidth centered around 1062 nm [4.23]. The pulse width is found using a TIPA Autocorrelator (Light Conversion), and the average FWHM from different bursts is 234 ± 10 fs, as shown in Figure 4.7b. A $Sech^2$ fit is used for the temporal domain, and a Lorentzian fit is used for the frequency domain. The experimental data are 1.4 and 2 times greater than the transform limited time-bandwidth product of a temporal Gaussian and $Sech^2$ distribution, respectively.

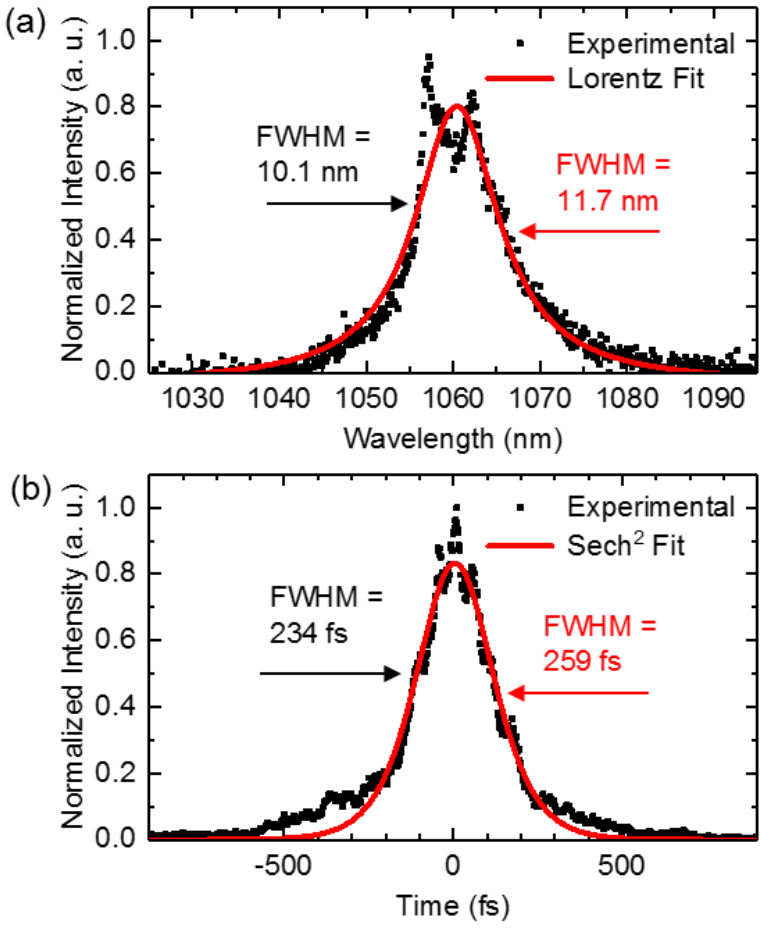

Figure 4.7. Time-bandwidth beam characteristics: (a) frequency domain and (b) time domain.

A new MHz-rate fs burst-mode laser has been demonstrated to produce >100 μJ per pulse energies, beam quality of M^2 = 1.5, and pulse-to-pulse deviations of less than 10%. With a 10.1 nm bandwidth and less than 0.5% ASE contribution, this laser exceeds the peak power and spectral bandwidth of commercial fiber amplifiers. As the demonstrated system is mostly operating in the small-signal gain regime, further increases in energy extraction and overall system efficiency can be achieved by incorporating more amplifiers, more amplifier passes, or utilizing a regenerative approach for extracting the stored energy in the rods. With just one more double pass through an additional rod in the small-signal gain regime, for example, output powers would increase by over an order of magnitude and reach greater than 17 GW/pulse and 7 GW/pulse at 100 kHz and 1 MHz, respectively. Because of the low average power of the burst-mode laser architecture, these output powers can be achieved with relatively low system complexity. Future work should also include efforts towards better pulse-to-pulse stability within the burst.

4.2 Femtosecond Burst-Mode Laser Diagnostics

4.2.1 FLEET Background

Accurate measurements of flow velocity in supersonic and hypersonic test facilities are important for the design and validation of performance models for high-speed flight vehicles. Probe based measurements traditionally used in subsonic facilities are not only limited in spatial and temporal resolution but can also significantly perturb the flow field around high-speed test articles. Optical techniques such as particle image velocimetry (PIV) have been demonstrated at high repetition rates in supersonic flows [4.24]; however, the accuracy is limited by particle lag in regions with high velocity gradients (*e.g.*, within the boundary layer or across shock fronts). Additional challenges such as limited optical access, particle seeding density issues, and desire to avoid hardware contamination discourages the application of PIV in many supersonic and hypersonic test facilities. Molecular-tagging-based velocimetry techniques have been developed to address the challenges of optical measurements in wind tunnel environments. Introducing a gas-phase tracer, such as nitric-oxide into the flow, allows for velocity measurements that are not subject to particle lag [4.25],[4.26]. However, flow mixing and diffusion limit the ability of tracers to get into the desired measurement region, and tracer injection can perturb the flow being analyzed. Recent progress in the Krypton tagging method has shown promise for reliable supersonic velocity measurements [4.27],[4.28] as it is chemically inert and less prone to alter flow physics.

Unseeded molecular tagging techniques take advantage of the fluorescence properties of molecules already present in flow and represent a promising approach for non-intrusive velocimetry in ground test facilities. Raman excitation and laser-induced electronic fluorescence (RELIEF) [4.29], Rayleigh scattering [4.30], and air photolysis and recombination tracking (APART) [4.31] have been demonstrated but are subject to their own limitations, such as complex setup requiring multiple lasers to be spatially overlapped.

Femtosecond (fs) laser electronic excitation tagging (FLEET) [4.32]-[4.35] is a technique that has been developed and demonstrated for velocimetry measurements based on the dissociation and tracking of the fluorescence that occurs during the subsequent recombination of nitrogen molecules. FLEET can be performed in a line-of-sight configuration with a single focused laser beam and camera, requiring only one small window for optical access [4.35]-[4.37]. While this approach has been shown to be applicable over a wide range of flow conditions and test facilities, data acquisition has generally been limited to a repetition rate of 1 kHz. This is not sufficient to

track the evolution of dynamical features in high-speed flows, such as turbulence and shock-flow interactions [4.38],[4.39]. This limitation was overcome recently by using a custom-built burst-mode laser that could operate at 100 kHz with 100 ps pulse durations in a 10 ms long burst [4.40]. Time-resolved flow measurements have been made using this technique, referred to as PLEET [4.41], but due to the longer pulse duration and lower peak power, the minimum energy threshold is around two orders of magnitude higher than FLEET and is not feasible at MHz rates with available laser energies.

4.2.2 FLEET Results

This work aims to increase the repetition rate of FLEET measurements by up to three orders of magnitude by employing a burst-mode fs laser capable of generating signals at rates up to 1 MHz. This laser is modified from a previous design that is described in detail in Ref. [4.42]. The current design enables a more compact laser architecture with fewer amplification stages and is described in further detail within the Supplementary Materials. Figure 4.8a and b show the time-bandwidth beam characteristics of the laser source, with a Gaussian transform limited pulse width of 274 fs at a central wavelength of 1063.6 nm. This differs from prior FLEET measurements using Ti:Sapphire lasers near 800 or 400 nm [4.32]-[4.39], which show an improvement in signal intensity at shorter wavelengths [4.33]. It is of interest, therefore, to evaluate FLEET measurements using the current laser because of differences in laser wavelength, beam quality, and pulse width. The quality of the compressed transform-limited beam was measured using a D4σ technique. The 4-mm-diameter beam was shown to diverge slightly astigmatically, resulting in an average M^2 of 3.15, as shown in Figure 4.8c. Burst profiles for 200 kHz and 1 MHz repetition rates can be seen in Figure 4.8d, with 200 ± 19.2 μJ/pulse and 120 ± 11.3 μJ/pulse, respectively. The burst duration of the laser is about 0.8 ms. However, the pulse energy of the laser during the beginning of the burst is too low to achieve sufficient signal. Therefore, FLEET measurements are only acquired for a duration of 0.5 ms. A +30 mm focal length achromatic lens doublet was used to produce a tightly focused spot, resulting in a calculated peak irradiance of 77.2 ± 7.4 TW/cm^2 and 46.3 ± 4.4 TW/cm^2, respectively, at the probe volume. The optical path of the laser was enclosed in lens tubes to mitigate environmental variations in the refractive index along the beam path. Optics were also placed on translating mounts to provide higher precision for focusing the laser spot to the desired measurement region of interest.

FLEET velocimetry was performed in a pressure-fed converging-diverging slot jet (see Figure 4.9) with a design Mach number 3.6 and perfect expansion to atmospheric pressure at 89 bar. Due to pressure losses in the system, supply pressures could be varied from 0 to 82.7 bar to attain a range from subsonic to supersonic velocities. FLEET has been shown to be quenched in intensity and lifetime in the presence of oxygen [4.32]. This is due to a tendency of dissociated nitrogen to recombine into nitric oxide rather than nitrogen molecules, which bypasses the FLEET emission mechanism. Hence, a gas mixing system allowed testing with either air or nitrogen to evaluate applicability for different wind tunnel conditions. The FLEET probe laser was aligned precisely across the exit of the supersonic nozzle to 2.8 mm from from the exit plane.

A high-speed CMOS camera (Photron, SA-Z Fastcam) was used to capture images of the FLEET signal as it propagated downstream. An image intensifier (LaVision, HS-IRO) with an S20 photocathode and P46 phosphor was used with the high-speed camera to provide precise time gating and increase in signal level. Sequences of tagged nitrogen spots were generated at both 200 kHz and 1 MHz rates. Images were captured at 200 kHz for all datasets. A pixel resolution of 384×160 was achieved with a Nikon 50 mm lens set to an f-stop of f / 1.2 and coupled with a 14 mm extension ring. The intensified camera was positioned above the nozzle to look downward onto the flow. The magnification of the imaging system was 32 μm/pixel. With a zoom lens and/or longer extension rings, the resolution can be improved. However, there is a trade-off between resolution and frame size since the signal can move significant distances in the high-speed flows being studied.

Originally, a 600 +/-25 nm bandpass filter was used to isolate the FLEET signal, but the reduction in signal posed a challenge at lower excitation energy. Instead of using a spectral filter to eliminate laser scattering, the gate of the camera was delayed to 70 ns after the laser pulses to ensure only the FLEET fluorescence was captured. This approach provided a significant improvement in signal level.

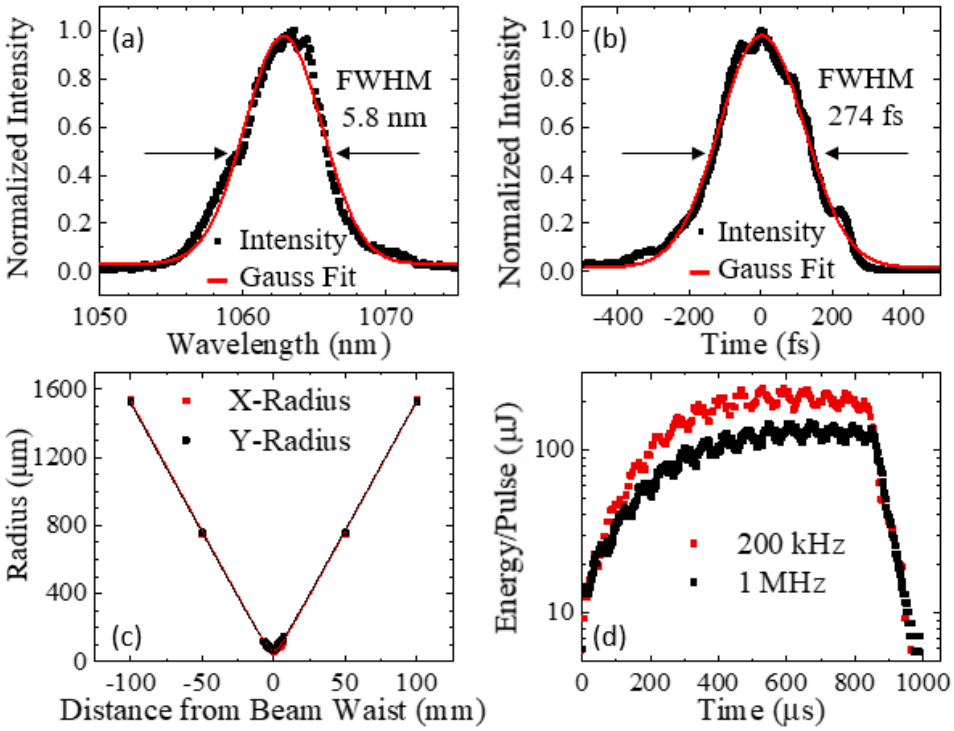

Figure 4.8. Parameters of fs laser, including (a) frequency domain bandwidth, (b) temporal domain pulse width, (c) beam quality divergence profiles after temporal compression with M^2 = 2.97 and 3.33 in *x* and *y* directions, respectively, and (d) burst profiles for 200 kHz and 1 MHz repetition rates.

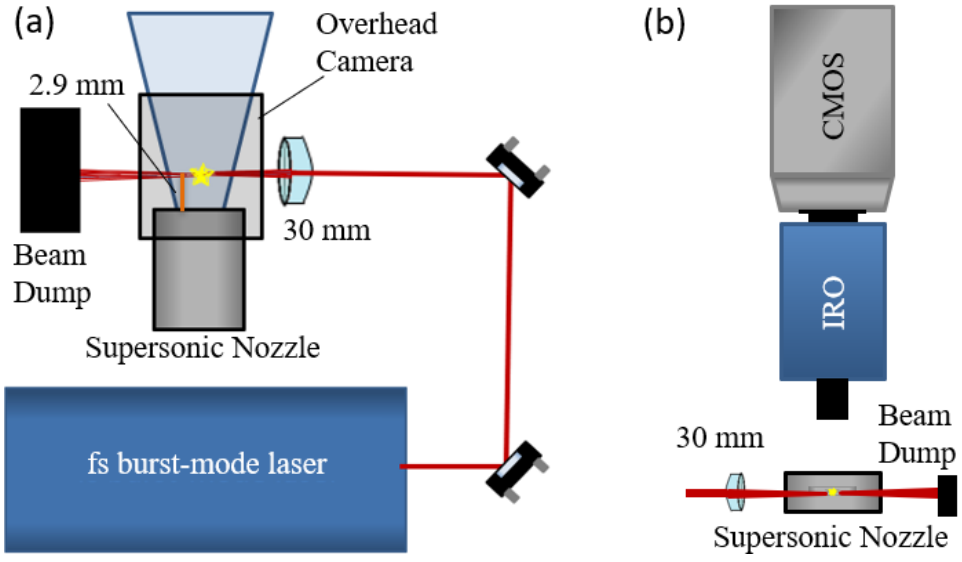

Figure 4.9. (a) Top view of FLEET experiment showing laser delivery to probe location through 30 mm focusing lens and (b) front view showing top-down placement of high-speed intensified camera.

Datasets were collected at upstream supply pressures of 30–70 bar to evaluate the measurement technique performance over a range of flow velocities (see Figure 4.10). For all of these operating conditions, the exit flow of the nozzle was slightly overexpanded. For the 68.9 bar condition, an intensifier gate of 800 ns was used with a gain of 65%, and for the 34.5 bar case the gate was 900 ns with a gain of 73%. A noticeable decrease in signal intensity was observed in the lower supply pressures. As there was no nitrogen co-flow, this was likely due to FLEET signal quenching from the entrainment of quiescent air. As such, the gain on the intensifier needed to be increased, leading to a lower signal to noise ratio. To evaluate the applicability of high-speed FLEET measurements to a wider range of facilities, the experiment was replicated with air as the supply fluid at 68.9 bar. Due to much higher signal quenching, the intensifier gate was set to 1500 ns with a gain of 85% to enable imaging of the less intense FLEET signals.

The tagged nitrogen molecules formed a spot at the focal point of the beam. With framing at 200 kHz, images of each spot could be taken every 5 µs. and the velocity obtained from the displacement of the spot between two successive frames. First the images were cropped to local regions around each spot with user input. A noise threshold for the image was found from the background values and any pixel below this threshold was set to zero. In FLEET velocimetry, a Gaussian intensity distribution can be fit across the spot to find the centroid location. Two dimensional Gaussian surface fitting was applied to the data collected in this experiment; however, this algorithm produced a large proportion of outlier velocity measurements due to poor fitting.

Three methods of centroid finding were then applied to the FLEET images, including a simple centroid, a bounding box centroid, and a weighted centroid. For each measurement, the largest discrepancy between centroid finding algorithms was taken to be the uncertainty in the velocity measurement. Figure 4.10a shows a trend of decreasing spot quality with decreasing supply pressure. Representative signals are shown for each supply pressure with associated results from the area centroid, bounding box centroid, and weighted centroid shown in cyan, red, and black, respectively. This leads to a correlated increase in the measurement uncertainty at lower pressures. Additionally, the uncertainty with the experiment in air was significantly higher due to poorer relative spot quality causing more relative error in centroid finding. As shown in Figure 4.10b, the uncertainties vary from 14.3 m/s at 34.5 bar (2.6%) to 7.3 m/s at 68.9 bar (1.14%), with the uncertainty for the air measurement being 53.2 m/s (8.3%).

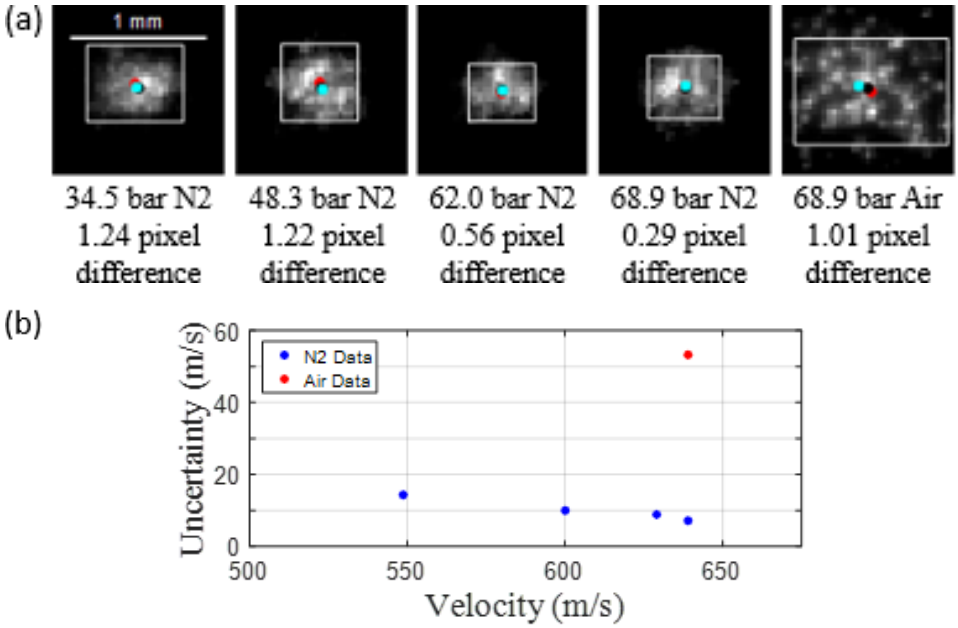

Figure 4.10. (a) Representative spot finding with area centroid (cyan dot), intensity weighted centroid (black dot), and bounding box (white box) with centroid (red dot); and (b) associated trend of uncertainty in velocity measurements for different pressures with pure N_2 and air.

Due to strong dependency on the binarization threshold and spot shapes associated with the area and bounding box centroid methods, an image correlation based velocity measurement method was implemented instead to further reduce uncertainty. The correlation method does not require thresholding, therefore it is insensitive to low signal levels. Between successive images of the same spot, a cross-correlation map of all possible displacements was created. The peak of this map was treated as the most likely displacement for the spot. A two pixel wide median filter was applied to each image before correlation was processed to eliminate small amounts of spatial non-uniformity. Bicubic interpolation near the correlation peak was applied to achieve sub-pixel accuracy on the displacement measurements. Figure 4.11 shows representative correlation maps for velocity measurements over the range of conditions tested. For the nitrogen cases, the correlation map is generally a Gaussian distribution about a clear peak, and the pixel shift is well defined. For the air case, the correlation map quality is lower, but a clear peak is still present.

In general, there was good agreement between the weighted centroid and correlation-based approaches. Ultimately, velocity is reported as the mean value of both methods, and the uncertainty is considered to be the absolute difference between both results at a given data point. Figure 4.12a shows the time history of measured velocity in nitrogen at 68.9 and 48.3 bar at the exit of the

nozzle. The mean values for these measurements are 639 and 600 m/s with standard deviations of 9.1 and 8.7 m/s, respectively. The uncertainties for these pressures using this method are 2.75 m/s (0.43%) and 3.32 m/s (0.55%), which is a marked improvement over using a centroid-only approach. Since the deviation of the measured flow velocity is larger than the uncertainty, it is concluded that this measurement method is sensitive enough to capture the unsteady flow fluctuations. Figure 4.12b shows the average trend of velocity with uncertainty bands.

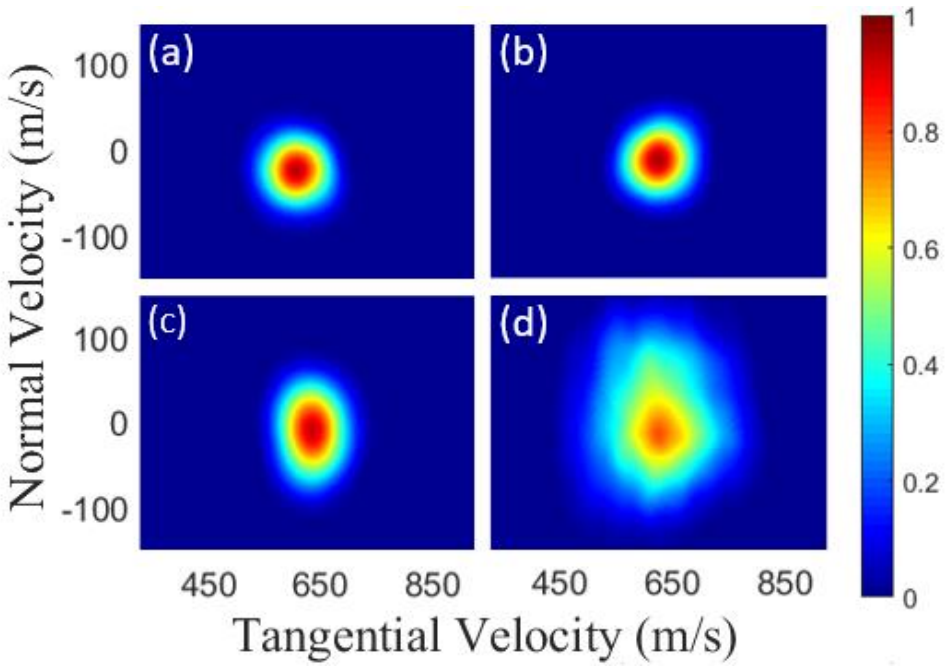

Figure 4.11. Correlation maps for displacement in (a) 34.5 bar nitrogen, (b) 48.3 bar Nitrogen, (c) 68.9 bar Nitrogen, and (d) 68.9 bar air.

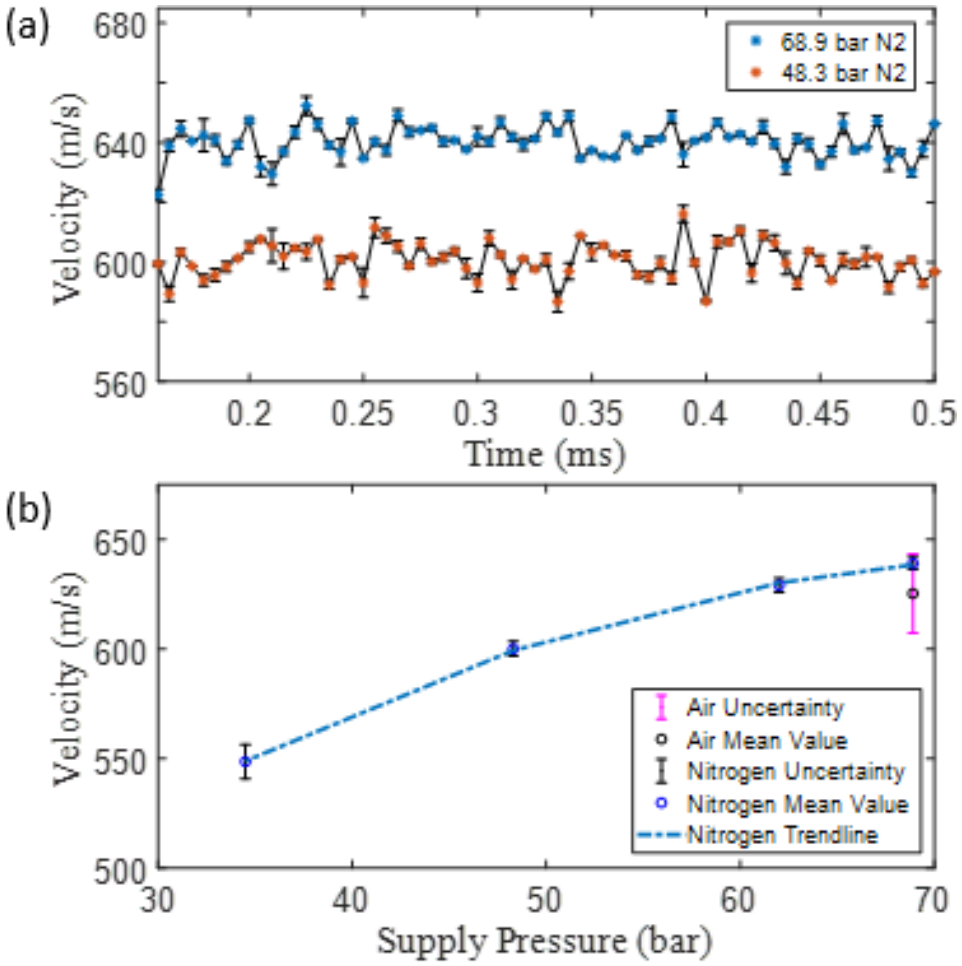

Figure 4.12. (a) Velocity time history for 68.9 and 48.3 bar supply pressures with nitrogen. (b) Average velocities and uncertainties for all tested conditions with nitrogen and air.

The uncertainty grows with decreasing pressure due to poorer spot quality. The expected velocity for a perfect expansion case for this nozzle at 89 bar is 651 m/s. While this condition could not be achieved with the experimental setup, the results trend toward this value as pressure increases showing good agreement between theory and measurements. The uncertainty of the air measurement is much larger as compared to the nitrogen measurements. To improve the accuracy of this technique for use in air, a more sensitive imaging system or higher laser energy is required.

Due to limitations in the framing rate of the imaging system, time-resolved data could not be taken above 200 kHz, but the laser was operated at 1 MHz to test the image quality that could be obtained for the pulse energies available at the highest possible repetition rate of the custom burst-mode fs laser. The gate and gain of the intensifier were set to 400 ns and 72%, respectively. Figure 6 shows results of two successive frames taken 5 μs apart with 1 MHz laser excitation. Each of the two

frames captures all of the spots generated by the 1 MHz laser that have convected downstream and which display sufficient fluorescence to be detected on the intensified camera. An example of five individual FLEET spots and their shift during the 5 μs time delay between images is marked in Figure 4.13a. Centroid finding is then performed as previously described to calculate all velocities, as shown in Figure 4.13b.

Unlike prior work with 1 kHz or even 100 kHz excitation, 1 MHz excitation allows for simultaneous measurement of velocity at multiple streamwise locations in supersonic flows without the use of beam-splitting optics. In addition, the measurement rate at each location is limited only by the framing rate of the imaging system. The rate of 200 kHz is higher than that demonstrated in prior work and is accomplished with two orders of magnitude lower excitation energy than prior 100 kHz PLEET measurements [4.36]. Moreover, with the current signal levels, available commercial MHz-rate image intensifiers and cameras will make it feasible to collect multi-point data at rates up to 1 MHz. Note that the signal-to-noise ratio for the images captured in this experiment is ~120, but the laser energy at the 1 MHz rate fluctuates above and below the lower signal threshold for FLEET, so only some acquisitions provide useful data at this repetition rate. As such further improvement in the laser energy amplitude and consistency would increase the data rate in these experiments.

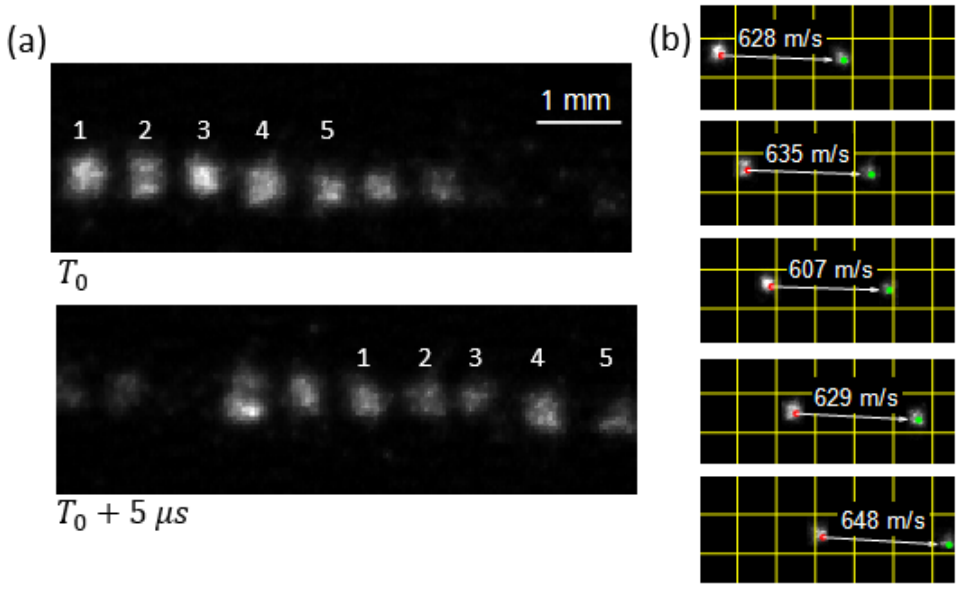

Figure 4.13. (a) Raw data collected with 1 MHz laser excitation. (b) Five velocities measured simultaneously along a streamline with 1 MHz laser excitation (grid spacing is 1 mm).

In conclusion, a compact burst-mode laser platform capable of producing high-energy femtosecond pulses has been demonstrated for excitation of FLEET signals at rates up to 1 MHz. A supersonic nozzle was used as a test case for proof-of-concept velocity measurements in supersonic flows with uncertainties of ~0.5%. Time-resolved velocimetry was conducted in unseeded nitrogen and air flows using the FLEET technique with laser excitation rates of 200 kHz to 1 MHz. The image collection rate of 200 kHz represents a significant improvement over prior FLEET measurements. However, single-shot measurements were achieved with 1 MHz laser excitation and demonstrate the feasibility for MHz-rate seedless velocimetry using intensified camera systems that are currently commercially available. With 1 MHz excitation and 200 kHz detection in the current work, five or more downstream locations could be tracked simultaneously for high-speed multipoint velocimetry. This work demonstrates an approach to increasing the spatio-temporal resolution of FLEET measurements, with the potential for further improvements in laser excitation energy, image collection efficiency, and framing rate of the intensified camera system in future work.

4.3 Femtosecond/Picosecond Burst-Mode Laser and CARS

4.3.1 Background

Coherent anti-Stokes Raman scattering (CARS) has been widely used for gas-phase thermometry and species concentration measurements in combusting and high-speed flows [4.43]-[4.45]. Early CARS measurements based on nanosecond (ns) laser systems were limited to rates ~10 Hz, with regenerative amplified femtosecond (fs) lasers later enabling measurements at 1–5 kHz [4.46]-[4.50]. While the latter represents a significant advancement for resolving slow to moderate-speed fluid dynamic instabilities, the various laser frequency conversion or pulse stretching processes needed to generate the CARS pump, Stokes, and probe pulses can incur significant optical losses, ultimately limiting the ability to resolve the dynamics in high-speed and turbulent flows. To achieve higher repetition rates, Roy et al. employed a high power ps burst-mode laser architecture for CARS measurements at 100 kHz [4.51]. Picosecond pulses, however, have a small spectral bandwidth of only a few wavenumbers, limiting the range of simultaneously accessible Raman transitions. Hence, these narrowband systems also incur significant losses in producing broadband pulses using dye lasers [4.52],[4.53] or non-linear parametric generation

[4.51]-[4.54]. As an alternative, electronically synchronized two-laser systems producing broadband fs and narrowband ps pulses can be used for efficient rotational CARS without extra frequency conversion or pulse stretching steps [4.55],[4.56]. A similar approach is to use spectrally narrowband amplification of part of the broadband fs pulse to produce inherently time-synchronized mJ-level narrowband ps pulses [4.57],[4.58]. Thus far, such fs/ps approaches relying on continuously pulsed fs/ps amplifiers have been limited to CARS measurements at low kHz rates.

4.3.2 Results

In this work, a broadband master oscillator is used as a common seed source for a dual-output burst-mode power amplifier that produces inherently synchronized fs and ps pulses with the inherent broadband and narrowband characteristics for MHz-rate CARS [4.59],[4.60]. System characteristics such as mode quality, shot-to-shot stability throughout the burst, and temporal and spectral profiles are discussed, along with proof-of-concept MHz fs/ps CARS at room temperature. This rate is an order of magnitude faster than previously reported using ps burst-mode systems [4.51] and two to three orders of magnitude faster than systems based on fs regenerative amplifiers [4.46]-[4.50],[4.55]-[4.58].

In the free-space power amplifier system shown in Figure 4.14, the output of a broadband master oscillator is split into two beams, the first of which is amplified by Nd:glass power amplifiers to produce broadband fs pulses. The second beam is amplified by a narrow gain bandwidth Nd:YAG power amplifier, which acts as a spectral filter and results in a narrowband ps output [4.58]. The master oscillator consists of a 20 nm spectral bandwidth, 50 MHz fs mode-locked fiber seed source (4 ps uncompressed pulsewidth) and an Ytterbium fiber amplifier (for details see Ref. [4.60]). The master oscillator output is gated down to 1 MHz by a 389 MHz bandwidth free-space AOM with a rise time of 4 ns (Gooch and Housego). The free-space AOM has a total efficiency of 16% and removes the continuous background due to amplified spontaneous emission (ASE) from the high-power fiber amplifier. After the free-space AOM, the beam is directed toward a polarizing beam splitter (PBS) to distribute the master oscillator pulse energy between the two power amplifier legs.

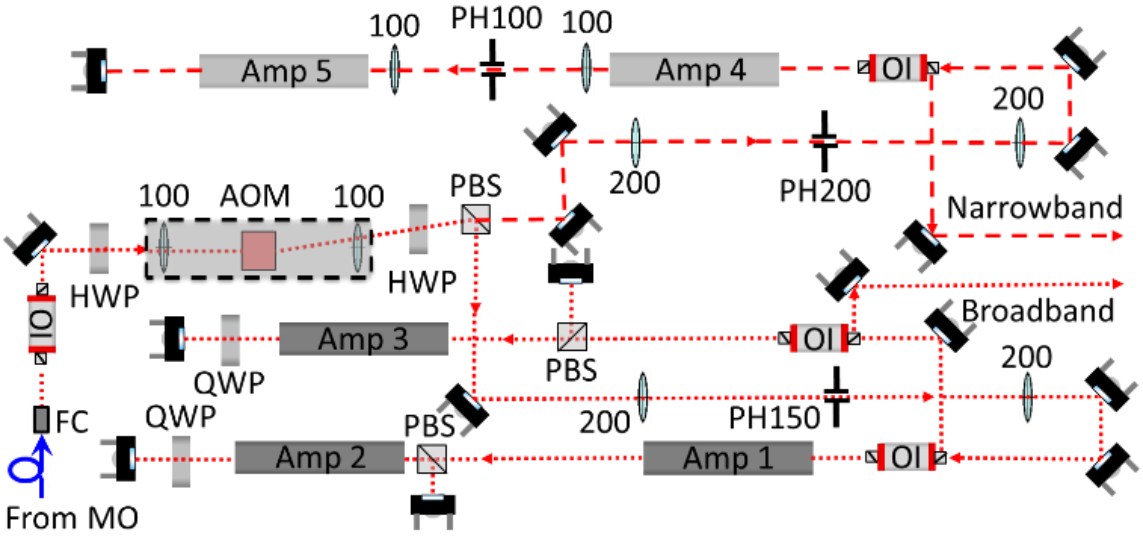

Figure 4.14. MHz-rate dual output fs/ps burst-mode system. Dashed lines represent the ps beam path and dotted lines represent the fs beam path. Lens focal lengths are indicated in mm. MO – master oscillator; FC - fiber collimator; OI - optical isolator; HWP - half-wave plate; AOM - acousto-optic modulator; PBS - polarizing beam splitter; PH# - pinhole with diameter in μm; QWP - quarter-wave plate. The system has a footprint of about 0.5 m x 1.2 m.

After the PBS, the reflected beam, designated as the fs beam, is sent through a one-to-one spatial filter to improve its beam quality and block any scattering light from the ASE leaking through the AOM. The spatially filtered beam passes through an optical isolator (OI) and is sent through the free-space amplification chain. The chain consists of three amplification steps: (i) Amplifier 1, which is passed twice; (ii) Amplifier 2, which is passed four times; and (iii) Amplifier 3, which is also passed four times (the attempt to pass both Amplifier 1 and 2 four times resulted in self lasing). The beam is then rejected by the OI and exits the system. The OI in each chain is used to prevent feedback. This fs leg is similar to the laser used in Fisher et al. [4.61]. Amplifiers 1–3 (IR Sources, Inc.) consist of flashlamp pumped Q-246 Nd:glass rods (L3 Kigre, Inc.). Amplifiers 1 and 2 have 3 mm diameter rods and 5 mm inside diameter flashlamps. Amplifier 3 has a 4 mm diameter rod and 6 mm inside diameter flashlamps (Xe, 450 torr, 79 mm arc length). The total electrical energy used for the fs beam per 1 ms burst is 700 J, and operation every 10 seconds results in an average electrical power of 70 W for this leg. All amplifiers are water cooled.

The beam traveling through the PBS directly after the AOM, designated as the ps beam, is sent through a one-to-one spatial filter to improve its beam quality and block any scattering light from the ASE leaking through the AOM. The spatially filtered beam passes through an OI to avoid

feedback and is sent through a free-space amplification chain. The chain consists of two amplifiers with a spatial filter between them. After the beam double passes the amplifiers, it is rejected by the OI and exits the system. Amplifiers 4 and 5 (IR Sources, Inc.) are composed of 3 mm diameter rods (Northrop Grumman Synoptics) and 4 mm inside diameter flashlamps (Xe, 450 torr, 79 mm arc length). The narrow gain bandwidth of Nd:YAG results in the amplification of only a narrow spectral portion of the broadband seed, resulting in a ps beam. The total electrical energy used for the ps beam per 1 ms burst is 80 J, and operation every 10 seconds results in an average electrical power of 8 W for this leg.

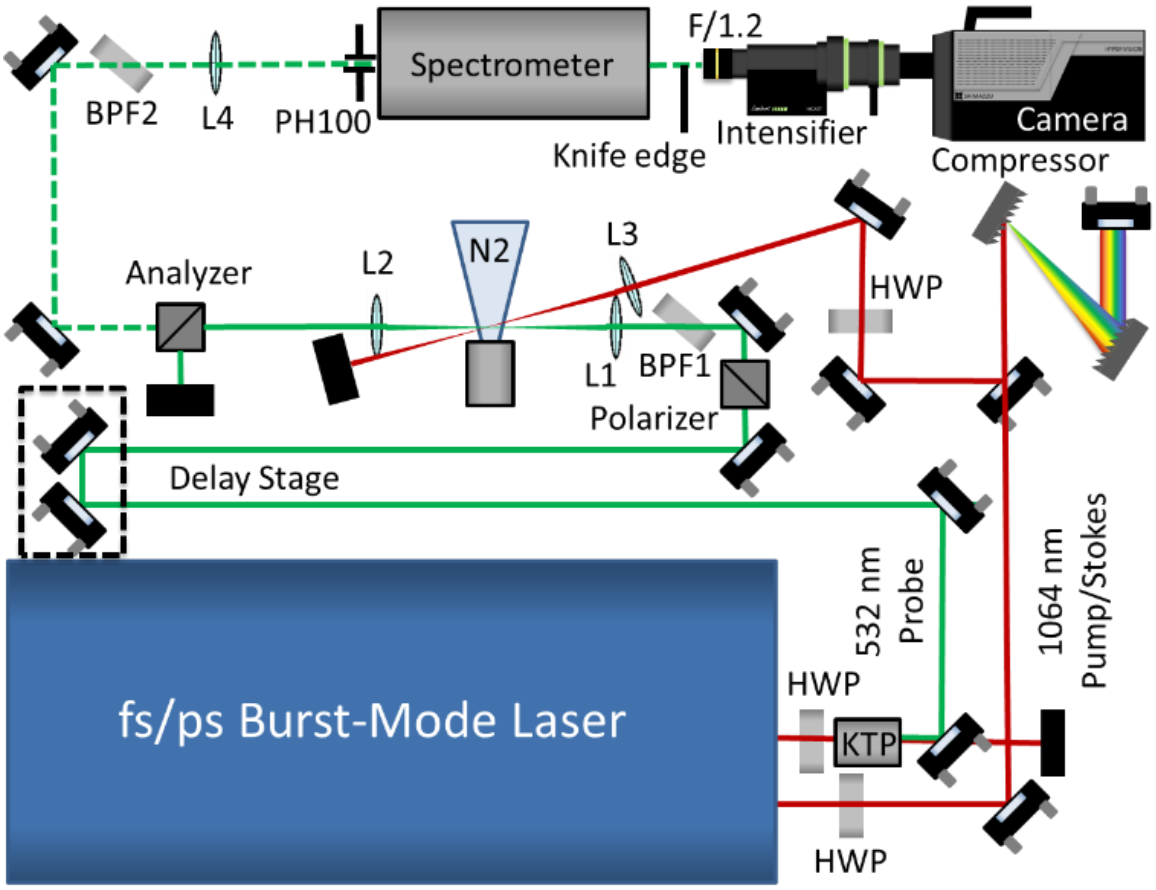

Figure 4.15. N_2 RCARS experimental layout. Solid green line is the probe beam, dashed green line is the CARS signal beam, and red line is the pump/Stokes beam. HWP - half-wave plate; KTP - potassium titanyl phosphate second harmonic generation crystal; BPF1/BPF2 - 532 nm bandpass filter; L1, L2, L3, L4 – 150, 200, 75, 150 mm focal length lenses, respectively; PH100 - 100 μm diameter pinhole; F/1.2 – *f*-stop 1.2, 50 mm Nikkor lens with 76 mm of extension rings.

The fs and ps beams exit the dual-output laser system and are prepared for RCARS signal generation, as shown in Figure 4.15. The fs beam is polarization tuned with a half-wave plate (HWP) to optimize 1st order diffraction in the diffraction grating compressor. The beam then travels over a mirror and negative temporal chirp is applied through two diffraction gratings (Thorlabs, 1200 g/mm, 26˚44' blaze angle). The compressor has an efficiency of 41%. The temporally compressed 274 fs beam is polarization rotated with another HWP and focused into the probe volume to act as the CARS pump/Stokes beam [4.55].

The ps beam is frequency doubled with a 12x12x10 mm potassium titanyl phosphate (KTP) crystal, and the 532 nm output with a vertical polarization is used as a probe beam for RCARS after passing through a temporal delay stage. Its polarization is cleaned by passing through a Glan-laser polarizer, and an angle-tuned 532 nm bandpass filter (Semrock, LL01-532-12.5) is used to suppress small peaks on the edge of the probe bandwidth. The pump/Stokes and probe beams are overlapped in the center of a nitrogen jet at 294 ± 2.2 K (Omega, Type K Thermocouple).

The RCARS phase matching scheme is similar to Bohlin et al. and Slipchenko et al. [4.55],[4.62]. With the pump/Stokes beam vertically polarized and probe beam polarization set to 45°, the polarization of the generated RCARS signal is at -27°, allowing it to be separated from the probe beam by the analyzer (Glan-laser) [4.55]. The residual probe light leaking through the analyzer is largely filtered out with a second angle-tuned 532 nm bandpass filter (Semrock, FF01-515/30), while the residual pump/Stokes beam is blocked with a beam dump. The signal beam is then focused into a spectrometer (Princeton Instruments, Acton SpectraPro SP-2500, 1200 g/mm), with any remaining probe-beam interference blocked with a knife edge before entering the MHz-rate intensified (Lambert Instruments, HiCatt 25) burst-mode camera (Shimadzu, HPV- X2) system. A 50 mm *f*/1.2 Nikkor lens with 76 mm of extension rings is attached to the camera system.

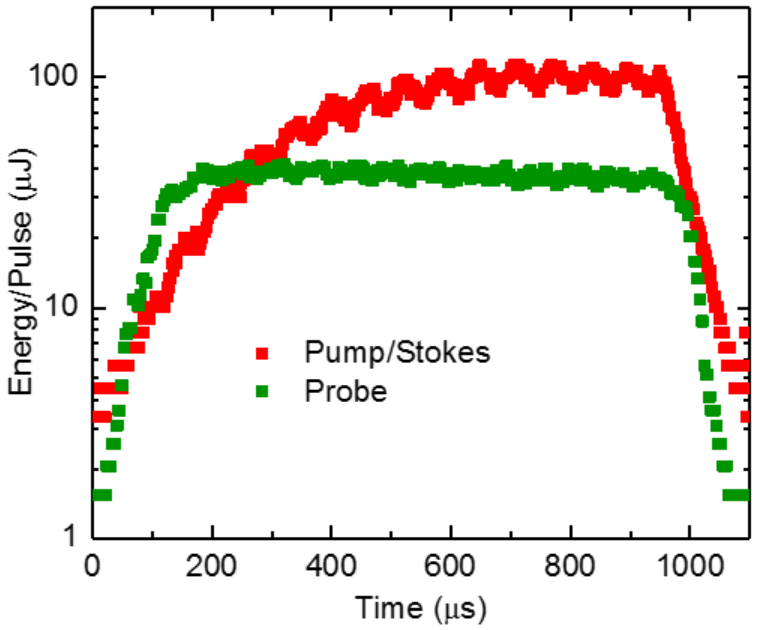

Figure 4.16. Experimental energy per pulse for temporally compressed 1064 nm pump/Stokes and 532 nm probe over a 1 ms burst. The master oscillator fs/ps splitting ratio is optimized for the best CARS signal.

The pump/Stokes beam is initially set close to maximum energy with the HWP after the AOM in Figure 4.14, since the CARS signal is linearly proportional to the strength of each of the pump, Stokes, and probe beams. The optimal splitting ratio between the fs leg beam and ps leg beam is then found by maximizing the CARS signal. Figure 4.16 shows the optimal pump/Stokes and probe energy per pulse over the entire burst duration. The peak energies of the pump/Stokes and probe beams are 95 ± 9 μJ and 38 ± 2 μJ per pulse, respectively. The oscillations in the pump/Stokes burst profile are traced to the fiber amplifier and tentatively attributed to the onset of nonlinear optical effects in the fiber. The ps beam second harmonic generation (SHG) conversion efficiency is 37%.

The fs and ps beam spatial characteristics are sampled immediately after exiting the laser and are found by transmitting the beams through a positive focal length lens to take a series of second-moment width (D4σ) beam diameter measurements [4.63]. The quality of the beam, M^2, is then found using the burst-averaged D4σ beam profile measurements in both the x- and y-directions shown in Figure 4.17. For the ps beam, the resulting M^2 values for the x- and y-directions are 1.95 and 2.07, respectively. For the fs beam, the resulting M^2 values for the x- and y- directions are 2.97 and 3.33, respectively. Thermal induced lensing due to high pump powers and imperfect

overlap between the effective mode area of the beam and pump areas in the rod are theorized to be the cause of the non-diffraction limited M^2 values. The overall beam spatial shape is circular with ps leg beam diameter around 2.4 mm and fs beam diameter around 3.1 mm.

The time-averaged temporal pulse widths and spectral bandwidths of the temporally compressed fs beam and ps beam are shown in Figure 4.18. For the fs beam, the spectral bandwidth is found using a spectrometer (Mightex, HRS-Series), and the temporal pulse width is found using an autocorrelator (Light Conversion, TiPA). For the ps beam, the spectral bandwidth is found using a wavemeter (Moglabs), and the temporal pulse width is found using a homebuilt autocorrelator based on the Michelson interferometer. In Figure 4.18a, the fs beam has a FWHM of 5.8 nm (51.5 cm-1) centered near 1061 nm. The nonuniform bandwidth is a result of large fiber amplifier input power creating higher order spectral phase components. Lowering the gain of the fiber amplifier by 3.5 provided a Gaussian profile, but the output energy was low for CARS. Figure 4.18b shows a 274 fs FWHM burst-averaged temporal pulse profile and is fit with a Gaussian. The time-bandwidth product (TBP) of the fs beam is 0.43, approximately the same as the transform limited Gaussian TBP of 0.44. The slight dip below 0.44 can be attributed to the nonuniform spectral bandwidth. Note that the fs beam bandwidth is smaller compared to the fs burst-mode system reported in Ref. [4.60] due to higher gain of the multi-pass Nd:glass amplifiers reported here, resulting in stronger gain narrowing [4.64]. The ps beam has a spectral FWHM of 0.077 nm (0.68 cm-1) centered at 1064.4 nm, shown in Figure 4.18c, and a temporal pulse width of 15.5 ± 2 ps FWHM, shown in Figure 4.18d. Both domains were fit to sech^2 functions for probe pulse time-bandwidth estimations. The TBP of the ps beam is 0.31, the same as the transform limited sech^2 TBP. It was not possible to directly measure the bandwidth and temporal profiles of the 532 nm probe beam. However, if we assume the ps beam is sech^2 in shape, the temporal pulse width is constant due to saturation [4.65], and the beam is transform limited, the resulting probe beam is centered at 532.19 nm with a spectral bandwidth upper estimate of 0.019 nm (0.68 cm-1).

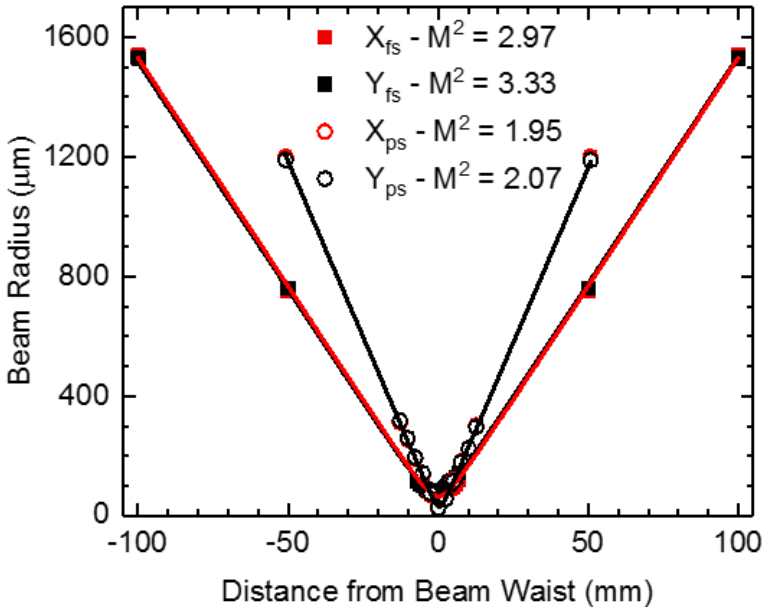

Figure 4.17. Burst-mode divergence profiles in the x- and y-directions for the uncompressed fs and ps beams.

Measurements are performed at 1 MHz repetition rate with the burst energy configuration shown in Figure 4.16. The focused irradiances are approximately 4.2 TW/cm^2 (52 μm radius at the focus) and 43 GW/cm^2 (43 μm radius at the focus) for the pump/Stokes and probe beams, respectively. The average x- and y-direction M^2 values are used in these calculations. The probe delay is set to 19 ps, approximately twice the pulse width of the 532 nm probe after SHG, to eliminate nonresonant contributions to the CARS signal. The intensifier gain voltage is set to 850 V, the intensifier gate is set to 600 ns, and the camera gate is set to 200 ns. 10 consecutive MHz-rate CARS spectra from a single burst are shown in Figure 4.19a. The spectra are taken 800 μs into the burst when the pulses are fully amplified. The signal at each time delay shows 7 distinct peaks spanning around 60 cm^{-1} with an average signal-to-noise ratio (SNR) of 176 (17600 peak single shot counts with 100 counts of noise). The temperature is obtained using a least-squares fitting routine to fit the experimental spectra with a phenomenological N_2 RCARS model, the details of which have been laid out previously [4.50],[4.66] and will not be discussed here. The best-fit simulations of these 10-shot spectra produce an average temperature of 293.4 ± 17 K, which is close to the thermocouple reading of 294 K. The uncertainty (~6%) is due to noise and nonlinearity in the detection system as well as shot-to-shot pump/Stokes bandwidth variations due to higher order spectral phase components from the fiber amplifier. Figure 4.19b shows the 10-shot signal

average with a best-fit simulation predicting a temperature of 288 K, which is within 2% of the thermocouple reading.

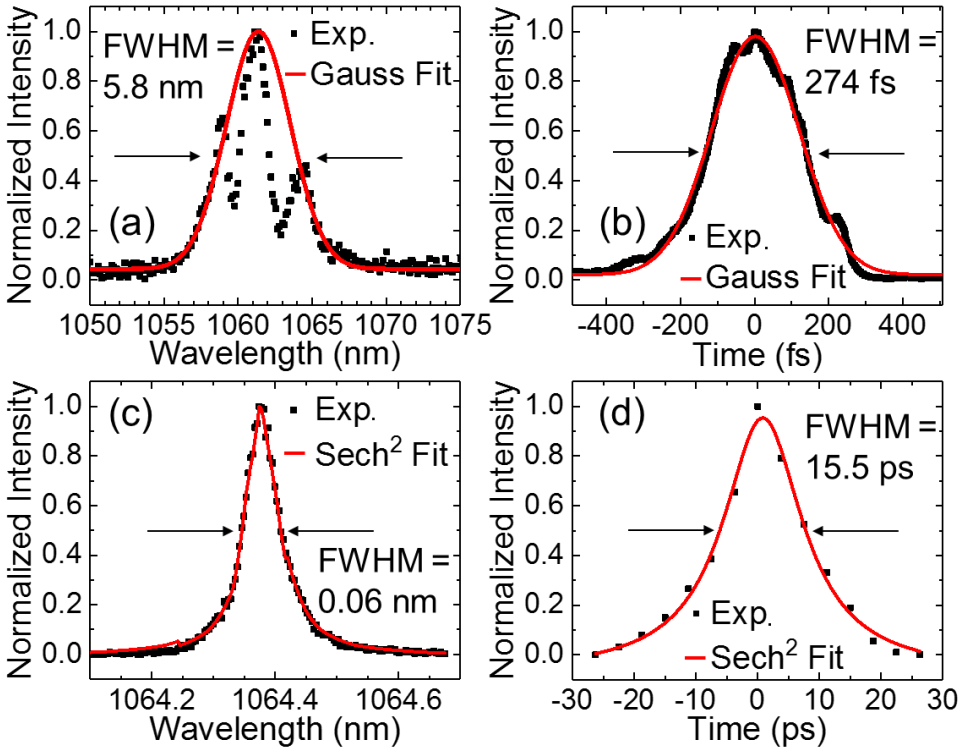

Figure 4.18. Time-bandwidth beam characteristics: (a) fs beam in the spectral domain; (b) fs beam in the temporal domain; (c) ps beam in the spectral domain; and (d) ps beam in the temporal domain.

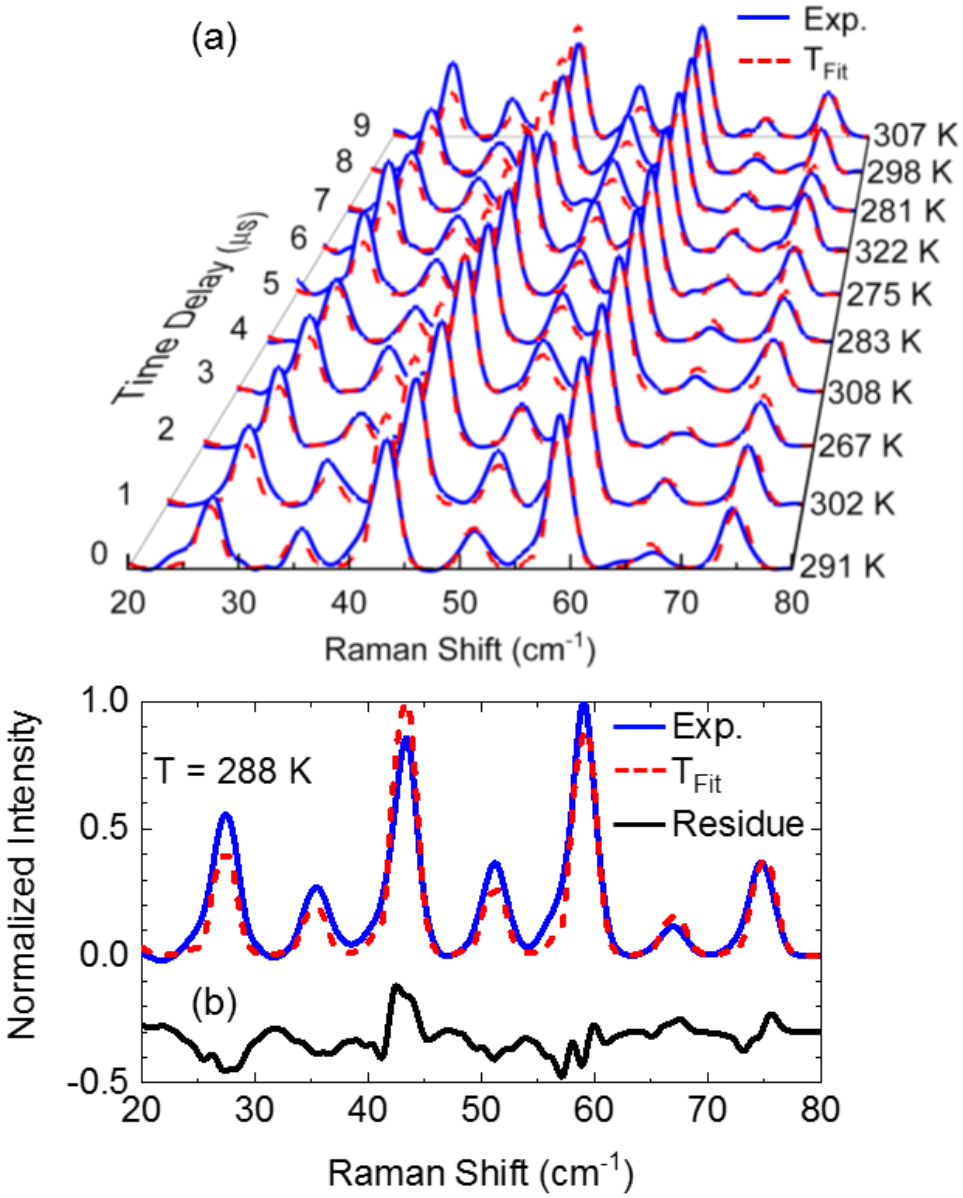

Figure 4.19. (a) 10 consecutive MHz CARS spectra 800 μs into a burst with corresponding best-fit simulations and (b) a 10-shot average.

In summary, a MHz-rate burst-mode laser has been characterized and demonstrated to produce inherently synchronized fs and ps pulses with sufficient peak irradiance for MHz-rate two-beam fs/ps RCARS. The rate exceeds prior ps burst-mode systems by an order of magnitude and continuously pulsed systems by two to three orders of magnitude. With inherent pulse synchronization and no complex frequency conversion systems, the CARS experimental arrangement is greatly simplified and the power requirements are reduced. Redesigning the

amplification scheme or adding more amplifiers would allow for more energy extraction in the system and lower the necessary input energies. This improvement may also correct spectral bandwidth perturbations and lower shot-to-shot variability in the CARS spectra, allowing for accurate temporally resolved thermometry in high-speed flows.

4.4 Regenerative Ultrafast Burst-Mode Laser Advances

4.4.1 Background

The motivation for this regenerative laser design stems from many different areas. In Smyser et al., a double-pass configuration with Q-246 Nd:glass was used to amplify broadband pulses, shown in the free-space optical layout in Figure 4.20 [4.60]. The small-signal gain (SSG) is small compared to other amplifiers like Nd:YAG, but it is necessary for total bandwidth amplification, as Nd:YAG has a narrowband gain medium and cannot be used for generating fs pulses. Since the SSG is small, and because the laser configuration is a double-pass, energy extraction from the rods is nonexistent. By utilizing a regenerative amplification scheme, much more energy can be extracted per pulse for the same amount of amplifying media and same pumping power, resulting in higher energy pulses.

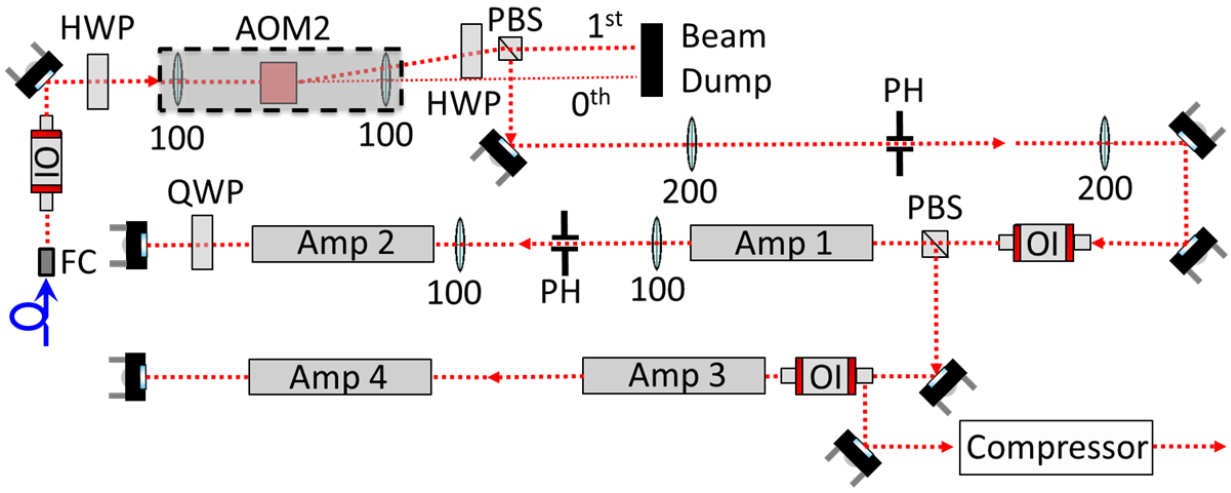

Figure 4.20. Free-space optical layout with f = 100 and 200 mm lenses. OI, optical isolator; HWP, half-wave plate; PBS, polarizing beam splitter; 0th, zeroth order beam; 1st, first order beam; PH, pinhole; QWP, quarter-wave plate. System size is 30 × 120 cm^2 [4.60].

The fiber amplifier was a necessary preamplifier but also a major concern for Smyser et al. and Fisher et al. [4.60],[4.61]. With appropriate voltage tuning, the fiber amplifier could produce higher input pulse energies with relatively low amounts of amplified spontaneous emission (ASE). In this scenario, however, the output pulses were plagued by nonlinear bandwidth degradation (self-phase modulation) and intensity oscillations between pulses. The results can be seen in Figure 4.21. By lowering the fiber amplifier voltage, the bandwidth degradation could be mitigated, but the intensity oscillations were always present, regardless of fiber amplifier voltage. Additionally, lowering the fiber amplifier voltage caused the output pulse energy to be too low for nonlinear techniques like FLEET and CARS. With a regenerative design, the fiber amplifier would not be needed for energy because enough passes could extract all the energy needed from the rods to have high energy pulses. This omits the bandwidth degradation and intensity oscillation problems. Additionally, regenerative amplifiers are known to produce excellent beam quality; this provides an added perk to this design.

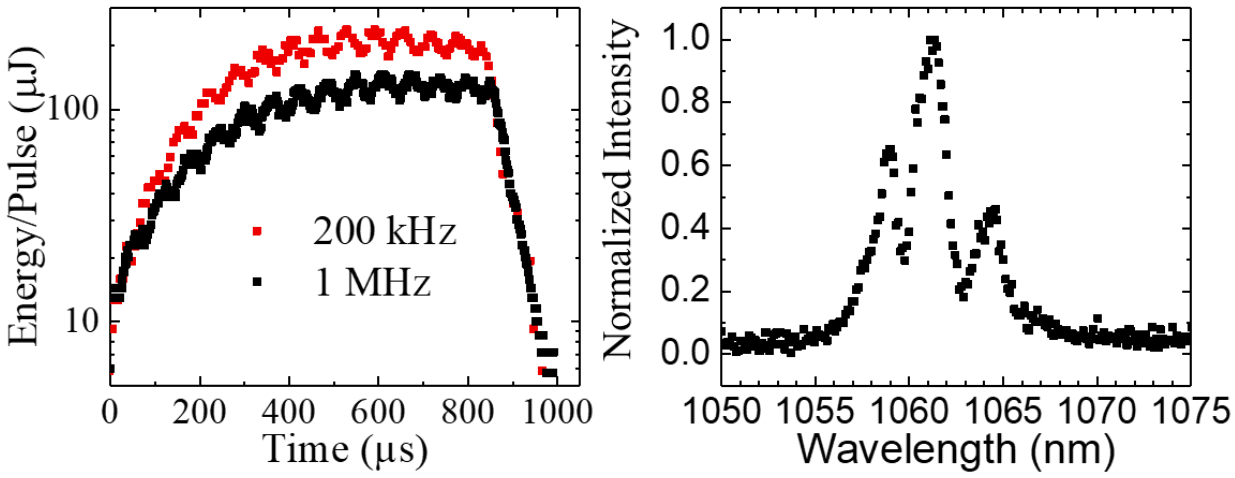

Figure 4.21. (left) 1 ms bursts at maximum flash lamp pump energy for 1 MHz and 200 kHz, and (right) the time-averaged frequency domain bandwidth of a 1 MHz repetition rate burst [4.61].

4.4.2 Results

The optical layout derives from the Mance et al. ns regen burst-mode laser and the Smyser et al. fs/ps burst-mode laser [4.67],[4.68], and this can be seen in Figure 4.22. The initial pulses are generated with a mode-locked fs fiber seed source at 50 MHz (Mendocino, Calmar Laser),

which also acts as an RF master oscillator for the laser system. The seed source has an initial average power of 40 mW and a spectral bandwidth of 20 nm full-width at half-maximum (FWHM) centered at 1064.6 nm. The uncompressed seed pulses are ~4 ps long. The output of the seed is first gated with a fiber-coupled acousto-optic modulator (150 MHz, 80 ns rise time, Brimrose) to produce a desired repetition rate of 100 kHz to 1 MHz. The AOM is synchronized with the seed through the delay generator (Quantum Composer, 9530 Series), which is phase-locked to the seed source. Because of the long rise time of the AOM, four pulses are gated out at set repetition rates.

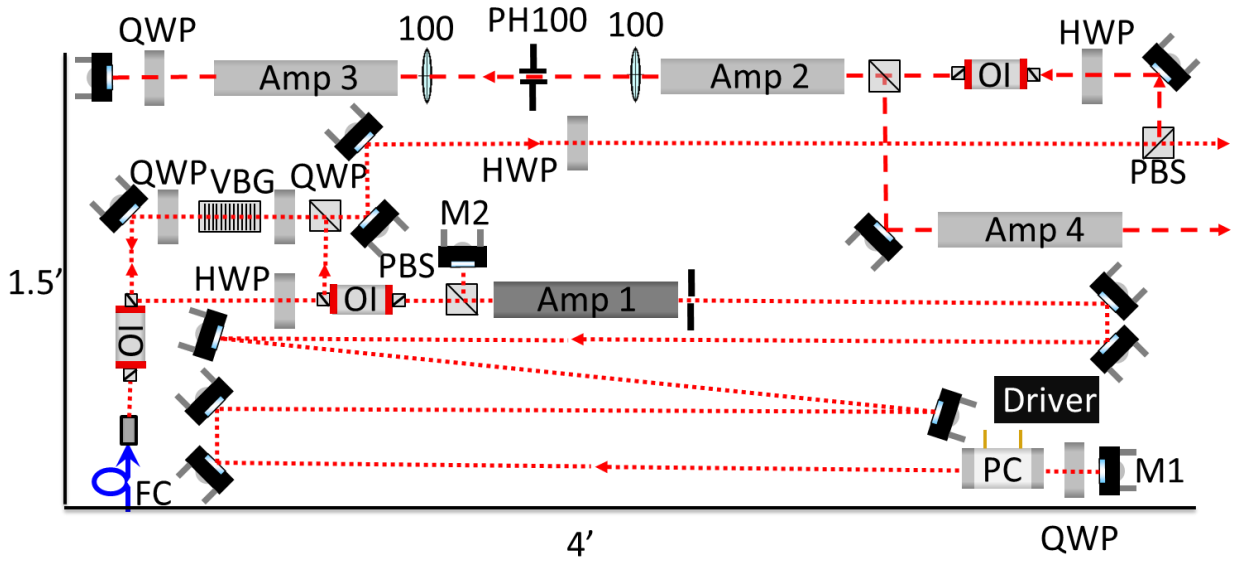

Figure 4.22. A synchronized fs regenerative amplified fs leg with a double-passed ps leg. FC, fiber collimator; OI, optical isolator; HWP, half-wave plate; VBG, volume Bragg grating; PBS, polarizing beam splitter; PH, pinhole; QWP, quarter-wave plate; PC, Pockels Cell; M1, convex mirror; M2, concave mirror. The system is 1.5' wide and 4' long.

The pulses are slightly focused (f ≈10 m) with a short focal length aspheric lens and sent through an optical isolator (OI) and into a volume Bragg grating (VBG). The OI is used to prevent feedback and reduce ASE in the system by polarization filtration. The VBG acts as a 3-dimensional diffraction grating, allowing different wavelengths to penetrate to different depths within the material. This phenomenon results in a temporally stretched pulse. The stretched broadband pulses are sent through another OI and enter the cavity by passing through a polarizing beam splitter (PBS). The PBS allows for cavitation and also improves the extinction ratio in the system. The cavity is created by a convex-concave mirror system, and pulses are locked in the cavity by a

Pockels Cell (3.5 mm aperture, 6.5 ns rise/fall time, Eksma Optics, Lithuania). The Pockels Cell rise/fall time is short enough to time gate 1 pulse from the remaining 4 pulses gated by the AOM. The cavity was designed in a similar way to Mance et al. [4.67], but the mirrors could be chosen to be different radii of curvature. The flashlamp-pumped (IR Sources, Inc.) 6 mm Nd:glass rod (L3 Kigre, Inc.) was placed near the concave mirror in the cavity to help mitigate possible Kerr effects (beam is largest here) and maintain TEM_{00} operation. The cavity length was initially theorized to be made long (~15 feet) to increase TEM_{00} mode volume (mode cross sectional area increases proportional with length for a given Fresnel number) since higher order spatial modes are prevalent in side-pumped configurations [4.64]. Figure 3 represents this length to scale. The iris is inserted to further improve beam mode quality.

The amplified pulses exit the cavity and are compressed by the VBG. The now compressed pulses (estimated 10 nm bandwidth and transform limited 167 fs pulse width) are polarization tuned to separate the energy between legs as needed for the different diagnostic techniques. The beam passes through an OI to avoid feedback, and is sent through a free-space amplification chain. The chain consists of two amplifiers with a spatial filter between them. After the beam double passes the chain, it is rejected by the PBS and is amplified in a single pass by a third amplifier. Amplifiers 2-4 (IR Sources, Inc.) are flashlamp pumped Nd:YAG (Northrop Grumman Synoptics), and are composed of 3 mm diameter rods and 4 mm inside diameter flash lamps. The narrow gain bandwidth of Nd:YAG causes the broadband seed to narrow, resulting in a narrowband ps beam.

ABCD law is used to calculate resonator stability and complex beam beam parameters in the system. Transfer matrices for different optical components can be seen in Table 4.1. Since the burst-mode regime is not in thermal steady state, it is assumed that the rod (~100 mm in length) is operating as a thermal lens with variable focal length for variable pumping powers. However, the system is first solved for no thermal lensing component for two reasons. First, the complexity of the system is reduced because of the omission of a variable focal length. Second, with certain stability optimization, it might be possible to significantly mitigate thermal lensing. Eq. 4.1 shows the stability of the cavity is a result of the first element of the overall transfer matrix, $T_{1,1}$, and the last element of the transfer matrix, $T_{2,2}$.

$$S = \frac{T_{1,1} + T_{2,2} + 2}{4} \tag{4.1}$$

A cavity is stable if $0 \leq S \leq 1$. Since cavity stability is a property of the cavity and not the number of passes, Eq. 4.1 is valid for 1 round trip in the system. If the cavity is optimized such that S = 0.5, the optical and mechanical axial perturbations, like pump-power-dependent thermal lensing and misalignment of the resonator mirrors, are minimized [4.69]. Regardless, it has been shown that, in general, stable cold convex-concave resonators maintain excellent stability conditions under strong end-pumped thermal lensing effects for a wide range of cavity lengths, which innately has stronger thermal lensing than side-pumped amplifiers [4.70]. So, a convex-concave resonator is a good choice for this system with or without thermal lensing.

The complex beam parameter, q, is needed to calculate the evolution of Gaussian beams through a series of optical elements, and is defined in Eq. 4.2:

$$\frac{1}{q} = \frac{1}{R(z)} - \frac{i\lambda_0}{\pi n \omega(z)^2} \tag{4.2}$$

where R(z) is the beam radius of curvature at z, λ_0 is the Gaussian beam's central wavelength (we will only use the central wavelength in our calculations), n is the index of refraction at z, and ω(z) is the beam radius at z. The input and output complex beam parameters are connected by Eq. 4.3, where $T_{i,j}$ represents different transfer matrix elements. A representation can be seen in Figure 4.23.

$$\frac{1}{q_{out}} = \frac{\left(T_{2,1} + \frac{T_{2,2}}{q_{in}}\right)}{T_{1,1} + \frac{T_{1,2}}{q_{in}}} \tag{4.3}$$

Figure 4.23. A representation of input and output complex beam parameters before and after a series of optical elements.

For our system, it is important that the beam radius of curvature matches the curvature of the first mirror in the cavity. For this reason, the preparation of the incident beam is vital. The overarching goal is to create a system with as few variables as possible separated into 3 different complex beam parameter compartments. The initial complex beam parameter, q_0, is designated before the interaction with the short aspheric collimating lens and directly at the end of the fiber optic relay system. We assume that the incident beam into the entire system is a wave with some short radius of curvature of R_0, λ_0 is 1064.6 nm, n is 1.5, and ω is the radius of the fiber optic. In this case, we will use a 0.125 mm diameter for a multimode fiber, but changing this is not detrimental to our solution. The distance between the aspheric lens and fiber optic output needs slight modification, but that is it. Thus, our q_0 complex beam parameter equation can be seen in Eq. 4.4.

$$\frac{1}{q_0} = \frac{1}{R_0} - \frac{i1064 * 10^{-6}}{\pi * 1.5 * \frac{0.125}{2}} \tag{4.4}$$

Because the aspheric lens is extremely short in focal length regardless of our choice in lens, the actual distance required to for radius of curvature evolution between the exit of the aspheric lens and the first mirror in the cavity changes on the order of a few mm and will be assumed to be insignificant. R_0 is left as a variable for now.

The second complex beam parameter, q_1, is the result of the preparation of the incident beam, and is located at M_1 in the regen cavity. The q_1 transfer matrix incorporates the fiber optic, the aspheric collimating lens, two QWP interactions, two OI interactions, a VBG interaction, a HWP interaction, an interaction with all components in the cavity once, and the distances between all of these components. This transfer matrix is shown in Eq. 4.5, with the only variables being the distance between the HWP and OI right before entering the cavity and the length of the cavity.

$$\begin{aligned} T_0 = T_{cavitylength} * T_d * T_{OI} * T_{d,variable} * T_{HWP} * T_d * T_{PBS} * T_d * T_{QWP} * T_d * T_{VBG} \\ * T_d * T_{QWP} * T_d * T_{OI} * T_d * T_{lens} * T_d * T_{fiber,face} \end{aligned} \tag{4.5}$$

For reference and an example, the T_{HWP} matrix consists of a refraction at a planar boundary matrix, a free-space propagation matrix, and another refraction at a planar boundary matrix.

The final complex beam parameter, q_2, is the result of our cavity calculations, shown in Eq. 4.6.

$$T_1 = T_{M1} * T_d * T_{PC} * T_{d,variable} * T_{rod} * T_d * T_{PBS} * T_{M2} * T_{PBS} * T_d * T_{rod} * T_{d,variable} * T_{PC} * T_d \quad 4.6$$

By choosing different complex/concave mirror combinations, we can ultimately have 4 variables in our system – a distance variable in our cavity, a distance variable outside our cavity, R_0, and the distance between the fiber optic and aspheric lens. The presented equations and logic are demonstrated in Appendix B.

In utilizing different mirrors, we try to obtain several goals for this regenerative burst-mode design. These goals include: (1) a shorter cavity length than Mance et al. produced (<3 m). This allows for a smaller overall laser footprint. (2) Beam diameters of 2 mm at M_1 and 4-4.5 mm at M_2. The beam diameter at M_1 is close to the aperture size of the Pockels Cell, allowing us to minimize beam fluence and best avoid damaging the Pockels Cell. The beam diameter at M_2 is a good size for optimal amplification through the rod (5-6 mm) in each double pass, while also mitigating damage possibilities from nonlinear effects like Kerr lensing and thermal lensing. (3) Stability criterion near 0.5 to best limit the effects of thermal lensing. (4) An incident beam radius of curvature onto M_1 that matches the radius of curvature of M_1. This is vitally important to the protection of the optical components in the cavity. If the radii of curvature do not match up, the beam diameter at each mirror will change in a sinusoidal fashion, creating the possibility of focusing on any/all of the optical components depending on the amount of double passes in the cavity. Figure 4.24 and Figure 4.25 illustrate this below using an example cavity that is not practical for our interests. The cavity consists of a convex mirror with R_1 = 2500 mm, a concave mirror with R_2 = -4000 mm, and nothing else. Figure 4.24 depicts severe changes in beam radius for each double pass due to cavity length miscalculation, while Figure 4.25 has constant beam radii due to correct cavity length calculations.

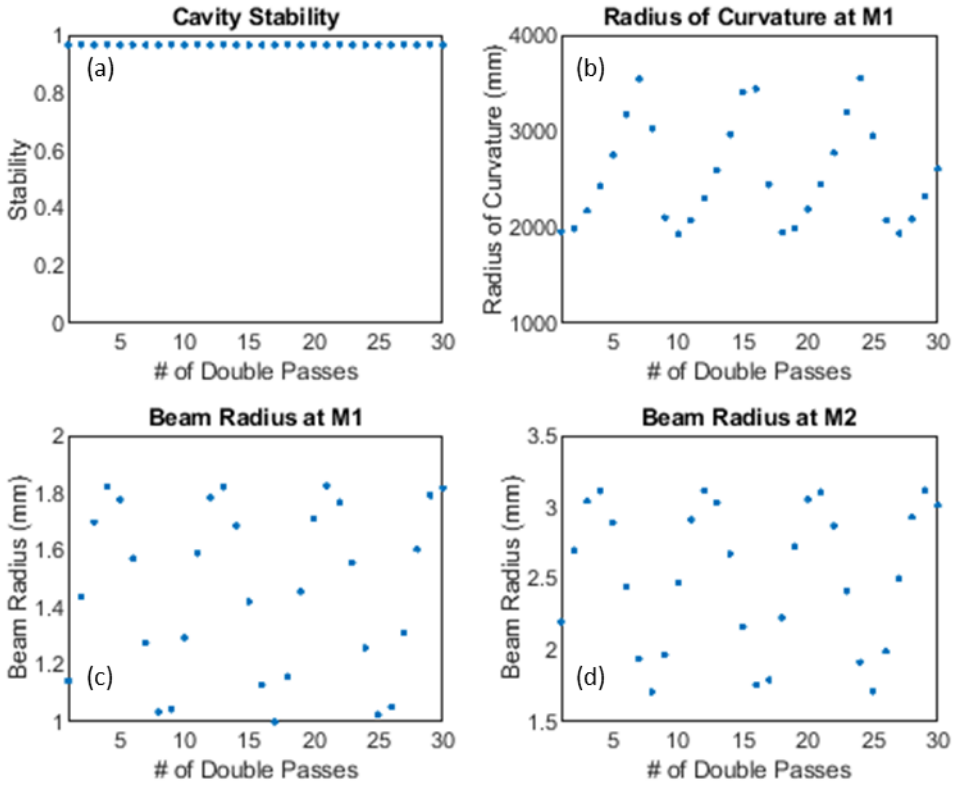

Figure 4.24. Regen cavity calculations over 30 cavity double passes done incorrectly. R1 = 2500 mm, R2 = -4000 mm, and the distance between the mirrors is 1700 mm. (a) The cavity stability; (b) The beam's radius of curvature after each double pass at M1; (c) The beam's radius after each double pass at M1; and (d) the beam's radius after each double pass at M2.

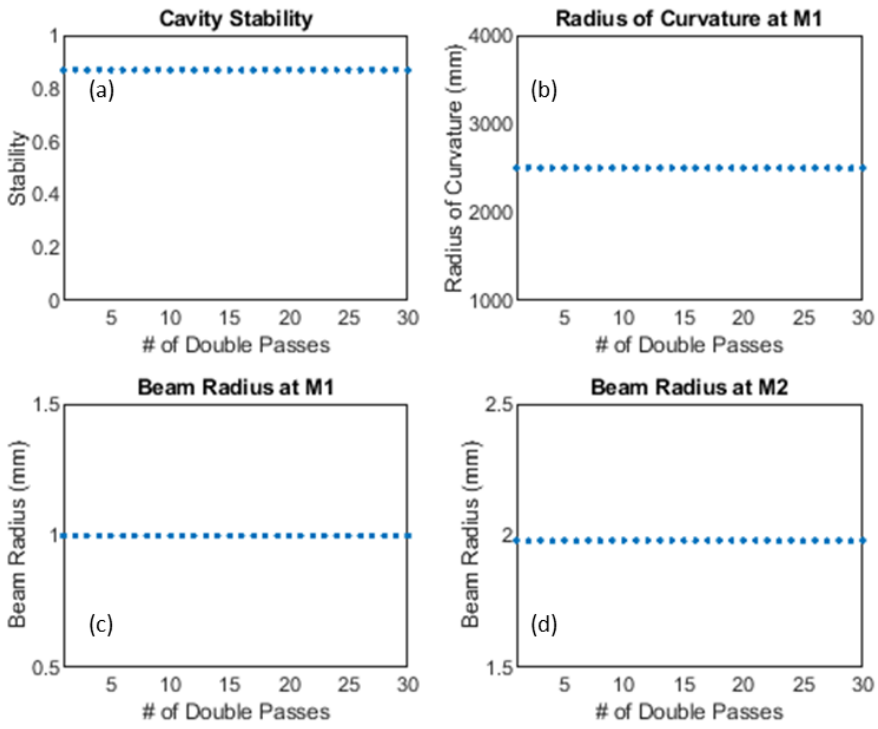

Figure 4.25. Regen cavity calculations over 30 cavity double passes done correctly. R1 = 2500 mm, R2 = -4000 mm, and the distance between the mirrors is 2118.7 mm (a) The cavity stability; (b) The beam's radius of curvature after each double pass at M1; (c) The beam's radius after each double pass at M1; and (d) the beam's radius after each double pass at M2.

The first step in the optimization process is to choose 2 mirrors, assume q_1 is perfect in both radius of curvature ($R_{beam} = R_1$) and beam diameter, and focus on optimizing the cavity distance. The variable distance in the cavity is a component of the total cavity length matrix used in Eq. 5, and is the only variable in Eq. 6 after choosing our 2 mirrors. The cavity length must be at least 750 mm shorter than the total length of the system to account for the added length of the constant distance + variable distance outside the cavity, and should be closer to 1 m if possible. The convex mirror radius of curvature is a good starting point to set the total distance required from the aspheric lens to M_1, and the iterative calculation to get the correct distance between M_1 and M_2 with the chosen radii of curvature will allow us to solve for the variable distance set outside of the cavity. The correct variable distance outside of the cavity should generate a beam radius of curvature that equals the radius of curvature of M_1 at M_1.

The last optimizations include R_0 adjustments and distance adjustments between the aspheric lens and fiber optic. These will minimally affect the real component of the complex beam

parameter, but vastly affect the imaginary component. Iterate between these 2 adjustments to create a beam diameter equal to the theoretical perfect beam diameter at M_1.

Creating a practical cavity that adequately satisfies our 4 goals is difficult and might be impossible. We will try utilizing the same cavity mirrors as Mance et al. (R_1 = 6200 mm and R_2 = -6800 mm). We nearly satisfy 3 of the 4 conditions, and the results can be seen in Figure 4.26 below. The cavity stability through the first double pass is 0.55 (nearly satisfies the 0.5 condition), the M_1 beam diameter is a constant 2 mm, the M_2 beam diameter is a constant 4.7 mm, and the M_1 beam radius fluctuates in a helix-like fashion close to the M_1 radius of curvature. The cavity length, however, is approaching 5 m. Furthermore, the variable distance between the HWP and OI is set at 980 mm. The results indicate an excellent and feasible optical layout if the laser footprint goal is thrown out the door. Shifting to different mirrors that allow for a shorter cavity length could prove problematic with the additional thermal lensing possibilities.

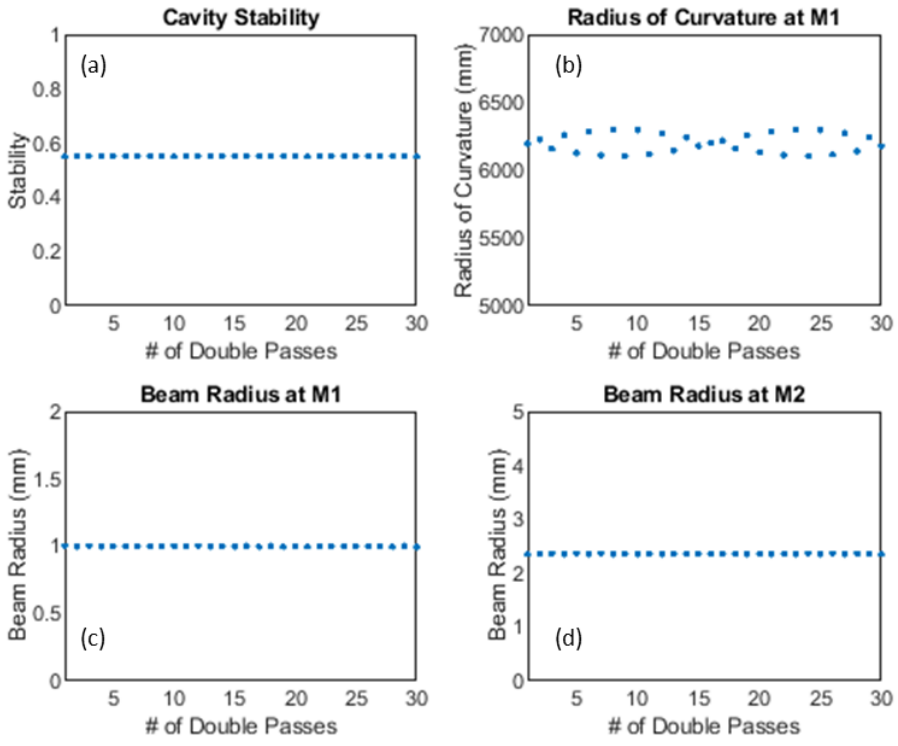

Figure 4.26. Regen cavity calculations over 30 cavity double passes. R1 = 6200 mm, R2 = -6800 mm, and the distance between the mirrors is 4712.5 mm (a) The cavity stability; (b) The beam's radius of curvature after each double pass at M1; (c) The beam's radius after each double pass at M1; and (d) the beam's radius after each double pass at M2.

Table 4.1. Transfer matrices of optical components.

Element	Matrix	Notes
Free-space propagation	$\begin{bmatrix} 1 & d \\ 0 & 1 \end{bmatrix}$	d is the distance between the last element and the next element
Refraction at a planar boundary	$\begin{bmatrix} 1 & 0 \\ 0 & \frac{n_1}{n_2} \end{bmatrix}$	n_1 is the preceding index of refraction and n_2 is the proceeding index of refraction
Refraction at a spherical boundary	$\begin{bmatrix} 1 & 0 \\ -\frac{n_2 - n_1}{n_2 R} & \frac{n_1}{n_2} \end{bmatrix}$	Convex: R>0 Concave: R<0
Transmission through a thin lens	$\begin{bmatrix} 1 & 0 \\ -\frac{1}{f} & 1 \end{bmatrix}$	Convex: f>0 Concave: f<0
Reflection from a planar mirror	$\begin{bmatrix} 1 & 0 \\ 0 & 1 \end{bmatrix}$	
Reflection from a spherical mirror	$\begin{bmatrix} 1 & 0 \\ \frac{2}{R} & 1 \end{bmatrix}$	Convex: R>0 Concave: R<0

4.5 References

[4.1] P. Wu, W. Lempert, and R. Miles, "Megahertz pulse-burst laser and visualization of shock-wave/boundary-layer interaction", AIAA J. **38**, 672-674 (2000).

[4.2] B. Thurow, N. Jiang, M. Samimy, and W. Lempert, "Narrow-linewidth megahertz-rate pulse-burst laser for high-speed flow diagnostics", Appl. Opt. **43**, 5064-5073 (2004).

[4.3] N. Jiang, M. Webster, W. Lempert, J. Miller, T. Meyer, C. Ivey, and P. Danehy, "MHz-rate nitric oxide planar laser-induced fluorescence imaging in a Mach 10 hypersonic wind tunnel", Appl. Opt. **50**, A20-A28 (2011).

[4.4] B. Brock, R. H. Haynes, B. S. Thurow, G. Lyons, and N. E. Murray, "An examination of MHz rate PIV in a heated supersonic jet", AIAA Paper 2014-1102, 52nd Aerospace Sciences Meeting, National Harbor, Maryland, Jan. 13-17, 2014.

[4.5] M. Smyser, K. Rahman, M. Slipchenko, S. Roy, and T. Meyer, "Compact burst-mode Nd: YAG laser for kHz-MHz bandwidth velocity and species measurements", Opt. Lett. **43**, 735-738 (2018).

[4.6] J. Miller, N. Jiang, M. Slipchenko, J. Mance, T. Meyer, S. Roy, and J. Gord, "Spatiotemporal analysis of turbulent jets enabled by 100-kHz, 100-ms burst-mode particle image velocimetry", Exp. Fluids **57**, 192 (2016).

[4.7] S. J. Beresh, J. F. Henfling, and R. W. Spillers, "Postage-stamp PIV:" small velocity fields at 400 kHz for turbulence spectra measurements," AIAA Paper 2017-0024, 55th Aerospace Sciences Meeting, Grapevine, TX, Jan. 9-13, (2017).

[4.8] J. Michael, P. Venkateswaran, C. Shaddix, and T. Meyer, "Effects of repetitive pulsing on multi-kHz planar laser-induced incandescence imaging in laminar and turbulent flames", Appl. Opt. **54**, 3331-3344 (2015).

[4.9] S. Roy, P. S. Hsu, N. Jiang, M. N. Slipchenko, and J. R. Gord, "100-kHz-rate gas-phase thermometry using 100-ps pulses from a burst-mode laser", Opt. Lett. **40**, 5125-5128 (2015).

[4.10] S. Roy, J. D. Miller, M. N. Slipchenko, P. S. Hsu, J. G. Mance, T. R. Meyer, and J. R. Gord, "100-ps-pulse-duration, 100-J burst-mode laser for kHz-MHz flow diagnostics", Opt. Lett. **39**, 6462-6465 (2014).

[4.11] www.ipgphotonics.com

[4.12] www.imra.com

[4.13] Marco Kienel, Michael Müller, Arno Klenke, Jens Limpert, and Andreas Tünnermann, "12 mJ kW-class ultrafast fiber laser system using multidimensional coherent pulse addition," Opt. Lett. **41**, 3343-3346 (2016)

[4.14] M. Mueller, A. Klenke, H. Stark, J. Buldt, T. Gottschall, A. Tünnermann, and J. Limpert, "1.8-kW 16-channel ultrafast fiber laser system", Proc. SPIE **10512**, Fiber Lasers XV: Technology and Systems, 1051208 (2018).

[4.15] P. Russbueldt, T. Mans, G. Rotarius, J. Weitenberg, H. D. Hoffman, and R. Poprawe, "400 W Yb: YAG Innoslab fs-amplifier", Opt. Express **17**, 12230-12245 (2009).

[4.16] M. Schulz, R. Riedel, A. Willner, S. Düsterer, M. J. Prandolini, J. Feldhaus, B. Faatz, J. Rossbach, M. Drescher, and F. Tavella, "Pulsed operation of a high average power Yb:YAG thin-disk multipass amplifier," Optics Express **20**, 5038-5043 (2012).

[4.17] S. Hädrich, M. Kienel, M. Müller, A. Klenke, J. Rothhardt, R. Klas, T. Gottschall, T. Eidam, A. Drozdy, P. Jójárt, Z. Várallyay, E. Cormier, K. Osvay, A. Tünnermann, and J. Limpert, "Energetic sub-2-cycle laser with 216 W average power", Opt. Lett. **41**, 4332-4335 (2016).

[4.18] W. R. Lempert, P. F. Wu, R. B. Miles, B. Zhang, J. L Lowrance, V. Mastrocola, and W. F. Kosonocky, “Pulse-burst laser system for high-speed flow diagnostics,” AIAA Paper 96-0179, 34th Aerospace Sciences Meeting, Reno, NV, Jan. 15-18, 1996.

[4.19] J. M. Fisher, M. E. Smyser, T. R. Meyer, M. N. Slipchenko, A. W. Caswell, J. R. Gord, and S. Roy, "Burst-Mode 100 kHz – 1 MHz FLEET Velocimetry in Supersonic and Hypersonic Flows," AIAA Paper 2019-1822, AIAA Scitech 2019 Forum, San Diego, CA, Jan. 7-11, 2019.

[4.20] J. D. Miller, S. Roy, J. R. Gord, and T. R. Meyer, “Communication: Time-domain measurement of high-pressure N2 and O2 self-broadened linewidths using hybrid femtosecond/picosecond coherent anti-Stokes Raman scattering,” J. Chem. Phys. **135**, 201104 (2011).

[4.21] M. E. Smyser, M. N. Slipchenko, T. R. Meyer, A. Caswell, J. R. Gord, and S. Roy, "MHz-Rate Ultrafast Laser for Nonlinear Spectroscopy in Transient and Nonequilibrium Hypersonic Flows," AIAA Paper 2019-1088, AIAA Scitech 2019 Forum, San Diego, CA, Jan. 7-11, 2019.

[4.22] T. F. Johnston, “Beam propagation (M^2) measurement made as easy as it gets: the four-cuts method”, Appl. Opt. **37**, 4840-4850 (1998).

[4.23] W. Koechner, *Solid-State Laser Engineering*, 4th Ed. (Springer Berlin, 1996).

[4.24] Bryan Brock, Randall H. Haynes, Brian S. Thurow, Gregory W. Lyons, and Nathan E. Murray. "*An examination of MHz rate PIV in a heated supersonic jet,*" AIAA Paper 2014-1102, 52nd Aerospace Sciences Meeting, National Harbor, Maryland, January 13-17, 2014, https://doi.org/10.2514/6.2014-1102.

[4.25] Paul M. Danehy, Sean O', Byrne, A. Frank P. Houwing, Jodie S. Fox, and Daniel R. Smith, *“Flow-Tagging Velocimetry for Hypersonic Flows Using Fluorescence of Nitric Oxide,”* AIAA Journal 41:2, 263-271, (2003), https://doi.org/10.2514/2.1939.

[4.26] Rodrigo Sánchez-González, Ravi Srinivasan, Rodney D.W. Bowersox, Simon W. North, *“Simultaneous velocity and temperature measurements in gaseous flow fields using the VENOM technique,”* Optics Letters 36. 196-8. (2011), https://doi.org/10.1364/OL.36.000196.

[4.27] M. A. Mustafa, N. J. Parziale, “*Simplified read schemes for krypton tagging velocimetry in N2 and Air*” Optics Letters 43. 2909-2912 12, (2018) https://doi.org/10.1364/OL.43.002909.

[4.28] M.A. Mustafa, D. Shehktman, N. J. Parziale, "*Single-Laser Krypton Tagging Velocimetry Investigation of Supersonic Air and N2 Boundary-Layer Flows over a Hollow Cylinder in a Shock Tube"* Physical Review Applied, 11, 064013, (2019) DOI: 10.1103/PhysRevApplied.11.064013.

[4.29] Richard B. Miles, C. Cohen, J. Connors, P. Howard, S. Huang, E. Markovitz, and G. Russell, "*Velocity measurements by vibrational tagging and fluorescent probing of oxygen*," Optics Letters 12, 861-863 (1987). https://doi.org/10.1364/OL.12.000861.

[4.30] Joseph N. Forkey, Noah D. Finkelstein, Walter R. Lempert, and Richard B. Miles. "*Demonstration and characterization of filtered Rayleigh scattering for planar velocity measurements*," AIAA Journal 34:3, 442-448 (1996). https://doi.org/10.2514/3.13087.

[4.31] Nanna M. Sijtsema, Nico J. Dam, Robert J. H. Klein-Douwel, J. J. Ter Meulen, "*Air Photolysis and Recombination Tracking: A New Molecular Tagging Velocimetry Scheme,"* AIAA Journal, 40:2, 1061-1064, (2002), https://doi.org/10.2514/2.1788.

[4.32] James B. Michael, Matthew R. Edwards, Arthur Dogariu, and Richard B. Miles, "Femtosecond laser electronic excitation tagging for quantitative velocity imaging in air," Applied Optics 50, 5158-5162 (2011), https://doi.org/10.1364/AO.50.005158.

[4.33] Nicholas J. DeLuca, Richard B. Miles, Waruna D. Kulatilaka, Naibo Jiang, and James R. Gord. "*Femtosecond Laser Electronic Excitation Tagging (FLEET) Fundamental Pulse Energy and Spectral Response*," AIAA Paper 2014-2227, 30th AIAA Aerodynamic Measurement Technology and Ground Testing Conference, Atlanta, Georgia, June 16-20, 2014, https://doi.org/10.2514/6.2014-2227.

[4.34] Paul M. Danehy, Brett F. Bathel, Nathan D. Calvert, Arthur Dogariu, and Richard B. Miles. "*Three Component Velocity and Acceleration Measurement Using FLEET*," AIAA Paper 2014-2228, 30th AIAA Aerodynamic Measurement Technology and Ground Testing Conference, Atlanta, Georgia, June 16-20, 2015, https://doi.org/10.2514/6.2014-2228.

[4.35] Ross A. Burns, Paul M. Danehy, Stephen B. Jones, Benjamin R. Halls, and Naibo Jiang. "*Application of FLEET Velocimetry in the NASA Langley 0.3-Meter Transonic Cryogenic Tunnel,"* AIAA Paper 2015-2566, 31st AIAA Aerodynamic Measurement Technology and Ground Testing Conference, Dallas, Texas, June 22-26, 2015, https://doi.org/10.2514/6.2015-2566.

[4.36] Ross A. Burns, Paul M. Danehy, Benjamin R. Halls, and Naibo Jiang, "*Femtosecond Laser Electronic Excitation Tagging Velocimetry in a Transonic, Cryogenic Wind Tunnel,"* AIAA Journal 55:2, 680-685, (2017), https://doi.org/10.2514/1.J055325.

[4.37] Ross. A. Burns and Paul. M. Danehy, "*Unseeded Velocity Measurements Around a Transonic Airfoil Using Femtosecond Laser Tagging,* AIAA Journal 55:12, 4142-4154, (2017), https://doi.org/10.2514/1.J056154.

[4.38] Naibo Jiang, Munetake Nishihara, and Walter R. Lempert, "*Quantitative NO2 molecular tagging velocimetry at 500 kHz frame rate*," Applied Physics Letters 97, 221103 (2010), https://doi.org/10.1063/1.3522654.

[4.39] Naibo Jiang, Matthew Webster, Walter R. Lempert, Joseph D. Miller, Terrence R. Meyer, Christopher B. Ivey, and Paul M. Danehy, "*MHz-rate nitric oxide planar laser-induced fluorescence imaging in a Mach 10 hypersonic wind tunnel*," Applied Optics 50, A20-A28 (2011), https://doi.org/10.1364/AO.50.000A20.

[4.40] Sukesh Roy, Joseph D. Miller, Mikhail N. Slipchenko, Paul S. Hsu, Jason G. Mance, Terrence R. Meyer, and James R. Gord, "*100-ps-pulse-duration, 100-J burst-mode laser for kHz–MHz flow diagnostics*," Optics Letters 39, 6462-6465 (2014), https://doi.org/10.1364/OL.39.006462.

[4.41] Naibo Jiang, Jason G. Mance, Mikhail N. Slipchenko, Josef J. Felver, Hans U. Stauffer, Tongxun Yi, Paul M. Danehy, and Sukesh Roy, "*Seedless velocimetry at 100 kHz with picosecond-laser electronic-excitation tagging*," Optics Letters 42, 239-242 (2017), https://doi.org/10.1364/OL.42.000239.

[4.42] Michael E. Smyser, Mikhail N. Slipchenko, Terrence R. Meyer, Andrew W. Caswell, and Sukesh Roy, "Burst-mode laser architecture for generation of high-peak-power MHz-rate femtosecond pulses," Under Review in Optics Letters, 2019.

[4.43] S. Roy, J. Gord, and A. Patnaik, "Recent advances in coherent anti-Stokes Raman scattering spectroscopy: Fundamental developments and applications in reacting flows", Progress in Energy and Combustion Science **36**, 280-306 (2010).

[4.44] G. Magnotti, A. D. Cutler, and P. M. Danehy, "Development of a dual-pump coherent anti-Stokes Raman spectroscopy system for measurements in supersonic combustion," Appl. Opt. **52**, 4779-4791 (2013).

[4.45] A. D. Cutler, L. M. L. Cantu, E. C. A. Gallo, R. Baurle, P. M. Danehy, R. Rockwell, C. Goyne, and J. McDaniel, "Nonequilibrium Supersonic Freestream Studied Using Coherent Anti-Stokes Raman Spectroscopy," AIAA J. 53, 2762-2770 (2015).

[4.46] S. Roy, W. D. Kulatilaka, D. R. Richardson, R. P. Lucht, and J. R. Gord, "Gas-phase single-shot thermometry at 1 kHz using fs-CARS spectroscopy," Opt. Lett. **34**, 3857-3859 (2009).

[4.47] J. D. Miller, M. N. Slipchenko, T. R. Meyer, H. U. Stauffer, and J. R. Gord, "Hybrid fs/ps coherent anti-Stokes Raman scattering for high-speed gas-phase thermometry," Opt. Lett. **35**, 2430-2432 (2010).

[4.48] D. R. Richardson, D. Bangar, and R. P. Lucht, "Polarization suppression of the nonresonant background in femtosecond coherent anti-Stokes Raman scattering for flame thermometry at 5 kHz," Opt. Exp. **20**, 21495-21504 (2012).

[4.49] S. P. Kearney and D. J. Scoglietti, "Hybrid femtosecond/picosecond rotational coherent anti-Stokes Raman scattering at flame temperatures using a second-harmonic bandwidth-compressed probe," Opt. Lett. 38, 833-835 (2013).

[4.50] C. E. Dedic, T. R. Meyer, and J. B. Michael, "Single-shot ultrafast coherent anti-Stokes Raman scattering of vibrational/rotational nonequilibrium," Optica 4, 563-570 (2017).

[4.51] S. Roy, P. S. Hsu, N. Jiang, M. N. Slipchenko, and J. R. Gord, "100-kHz-rate gas-phase thermometry using 100-ps pulses from a burst-mode laser", Opt. Lett. **40**, 5125-5128 (2015).

[4.52] S. Roy, T. R. Meyer, and J. R. Gord, "Broadband coherent anti-Stokes Raman scattering spectroscopy of nitrogen using a picosecond modeless dye laser," Opt. Lett. **30**, 3222-3224 (2005).

[4.53] T.R. Meyer, S. Roy, and J. R. Gord, "Improving Signal-to-Interference Ratio in Rich Hydrocarbon-Air Flames Using Picosecond Coherent Anti-Stokes Raman Scattering," Appl. Spectr. **61**, 1135-1140 (2007).

[4.54] H. Graener, A. Laubereau, and J. W. Nibler, "Picosecond coherent anti-Stokes Raman spectroscopy of molecules in free jet expansions," Opt. Lett. **9**, 165-167 (1984).

[4.55] A. Bohlin, B. D. Patterson, and C. J. Kliewer, "Communication: Simplified two-beam rotational CARS signal generation demonstrated in 1D", J. Chem. Phys. **138**, 081102 (2013).

[4.56] J. D. Miller, M. N. Slipchenko, J. G. Mance, S. Roy, and J. R. Gord, "1-kHz two-dimensional coherent anti-Stokes Raman scattering (2D-CARS) for gas-phase thermometry," Opt. Exp. **24**, 24971-24979 (2016).

[4.57] R. Santagata, M. Scherman, M. Toubeix, M. Nafa, B. Tretout, and A. Bresson, "Ultrafast background-free ro-vibrational fs/ps-CARS thermometry using an Yb:YAG crystal-fiber amplified probe," Opt. Exp. **27**, 32924-32937 (2019).

[4.58] K. A. Rahman, E. L. Braun, M. N. Slipchenko, S. Roy, and T. R. Meyer, "Flexible chirp-free probe pulse amplification for kHz fs/ps rotational CARS," Opt. Lett. **45**, 503-506 (2020).

[4.59] S. Roy, J. D. Miller, M. N. Slipchenko, P. S. Hsu, J. G. Mance, T. R. Meyer, and J. R. Gord, "100-ps-pulse-duration, 100-J burst-mode laser for kHz-MHz flow diagnostics," Opt. Lett. **39**, 6462-6465 (2014).

[4.60] M. E. Smyser, M. N. Slipchenko, T. R. Meyer, A. W. Caswell, and S. Roy, "Burst-mode laser architecture for the generation of high-peak-power MHz-rate femtosecond pulses," OSA Cont. **2**, 3490-3498 (2019).

[4.61] J. M. Fisher, M. E. Smyser, M. N. Slipchenko, S. Roy, and T. R. Meyer, "Burst-mode femtosecond laser electronic excitation tagging for kHz-MHz seedless velocimetry," Opt. Lett. **45**, 335-338 (2020).

[4.62] M. N. Slipchenko, B. D. Prince, S. C. Ducatman, and H. U. Stauffer, "Development of a Simultaneously Frequency- and Time-Resolved Raman-Induced Kerr Effect Probe," J. Phys. Chem. A **113**, 135-140 (2009).

[4.63] T. F. Johnston, "Beam propagation (M^2) measurement made as easy as it gets: the four-cuts method", Appl. Opt. **37**, 4840-4850 (1998).

[4.64] W. Koechner, *Solid-State Laser Engineering*, 4th Ed. (Springer Berlin, 1996).

[4.65] J. Zhang, J. Y. Huang, H. Wang, K. S. Wong, and G. K. Wong, "Second-harmonic generation from regeneratively amplified femtosecond laser pulses in BBO and LBO crystals," J. Opt. Soc. Am. B **15**, 200-209 (1998).

[4.66] H. U. Stauffer, J. D. Miller, M. N. Slipchenko, T. R. Meyer, B. D. Prince, S. Roy, and J. R. Gord, "Time- and frequency-dependent model of time-resolved coherent anti-Stokes Raman scattering (CARS) with a picosecond-duration probe pulse," J. Chem. Phys. **140**, 024316 (2014).

[4.67] J. G. Mance, M. N. Slipchenko, and S. Roy, "Regenerative amplification and bifurcations in a burst-mode Nd:YAH laser," Opt. Lett. 40, 5093-5096 (2015).

[4.68] M. E. Smyser, E. L. Braun, V. Athmanathan, M. N. Slipchenko, S. Roy, and T. R. Meyer, "Dual-output fs/ps burst-mode laser for MHz-rate rotational coherent anti-Stokes Raman scattering." Opt. Lett. **45**, ????, (2020).

[4.69] W. Koechner and M. Bass, Solid-State Lasers: A Graduate Text, (2006).

[4.70] P. H. Tuan, C. C. Chang, C. Y. Lee, C. Y. Cho, H. C. Liang, and Y. F. Chen, "Exploiting concave-convex linear resonators to design end-pumped solid-state lasers with flexible cavity lengths: application for exploring the self-mode-locked operation," Opt. Exp. 24, 26024-26034 (2016).

5. CONCLUSION

The purpose of this dissertation was to demonstrate advances in burst-mode laser technology development and its applications for MHz-rate measurements in high-speed gas-phase environments. This dissertation illustrated the fundamental background of the burst-mode laser, a universal burst-mode laser model applicable to any pulse width, direct improvements in the nanosecond (ns) and ultrafast regimes, and the design parameters and results for MHz-rate operation. MHz-rate FLEET and hybrid RCARS are applications that were performed and analyzed.

A computational model was composed for the purpose of comparison to experimental hardware and the prediction of future hardware outputs. The overarching goal was to create a comprehensive model that can accurately predict energy, temporal, spectral, and spatial outputs for a novel laser design given relatively few inputs. This model has shown the capability to output, within reasonable uncertainty, the energy, temporal, and spectral profiles of the ns burst-mode laser and fs burst-mode laser. For the ns laser, the energy output was within a factor of 2, and input power and small-signal gain discrepancies can shift the output energy to match the experimental output. The temporal domain skewed positively in an expected manner due to long pulse lengths. The initial portion of the pulse was able to extract energy on the backwards passes before the latter portions of the pulse were able to undergo the forward pass, affecting their overall gain. The spectral domain was expected to remain a near constant, and this was the case. The narrow seed bandwidth was centered on the orders of magnitude broader gain bandwidth of the Nd:YAG rod, so spectral shifting should not occur. For the fs laser, the energy output was nearly identical between the model and the experimental output, falling with 1.7% of each other. Small changes of approximately 0.01 to 0.05 of small-signal gain measurements would result in that type of energy fluctuation. The FWHM modeled bandwidth was 9 nm compared to the experimental bandwidth of 10.1 nm. The offset was attributed to unaccounted for nonlinear spectral phase components. The temporal pulse shapes of the model did not change throughout amplification because no temporal stretching physics package was implemented, and the pulses were too short to affect parts of themselves.

In the ns regime, a simplified burst-mode laser architecture with a 0.18 m^2 footprint has been demonstrated to produce sufficient pulse energy, mode quality, and pulse-to-pulse stability for accurate measurements of velocity and species with kHz–MHz bandwidth for a duration up to 10 ms. The design allows for flexible use of the fundamental 1064 nm or frequency-doubled 532 nm output, along with custom pulse patterns such as doublets or singlets for use in various measurement techniques. Future improvements of this laser architecture include pumping of a tunable source, extension to UV wavelengths, and use of shorter pulse widths to enhance the second-harmonic generation efficiency.

In the fs regime, a new MHz-rate fs burst-mode laser has been demonstrated to produce >100 µJ per pulse energies, beam quality of $M^2 = 1.5$, and pulse-to-pulse deviations of less than 10%. With a 10.1 nm bandwidth and less than 0.5% ASE contribution, this laser exceeds the peak power and spectral bandwidth of commercial fiber amplifiers. As the demonstrated system is mostly operating in the small-signal gain regime, further increases in energy extraction and overall system efficiency can be achieved by incorporating more amplifiers, more amplifier passes, or utilizing a regenerative approach for extracting the stored energy in the rods. With just one more double pass through an additional rod in the small-signal gain regime, for example, output powers would increase by over an order of magnitude and reach greater than 17 GW/pulse and 7 GW/pulse at 100 kHz and 1 MHz, respectively. Because of the low average power of the burst-mode laser architecture, these output powers can be achieved with relatively low system complexity. Future work should also include efforts towards better pulse-to-pulse stability within the burst.

An adaptation of this laser has been demonstrated for excitation of FLEET signals at rates up to 1 MHz. A supersonic nozzle was used for proof-of-concept velocity measurements with uncertainties of ~ 0.5%. Time-resolved velocimetry was conducted in unseeded nitrogen and air flows with laser excitation rates of 200 kHz to 1 MHz. The image collection rate of 200 kHz represents a significant improvement over prior FLEET measurements. Single-shot measurements achieving 1 MHz laser excitation demonstrate the feasibility for MHz-rate seedless velocimetry using intensified camera systems that are currently commercially available. With 1 MHz excitation and 200 kHz detection in the current work, five or more downstream locations could be tracked simultaneously for high-speed multipoint velocimetry. This work demonstrates an approach to increasing the spatiotemporal resolution of FLEET measurements, with the potential for further

improvements in laser excitation energy, image collection efficiency, and framing rate in future work.

This fs laser system was improved to include a ps leg, and was demonstrated to produce inherently synchronized fs and ps pulses with sufficient peak irradiance for MHz-rate two-beam fs/ps RCARS. The rate exceeds prior ps burst-mode systems by an order of magnitude and continuously pulsed systems by two to three orders of magnitude. With inherent pulse synchronization and no complex frequency conversion systems, the CARS experimental arrangement is greatly simplified and the power requirements are reduced. Redesigning the amplification scheme or adding more amplifiers would allow for more energy extraction in the system and lower the necessary input energies. This improvement may also correct spectral bandwidth perturbations and lower shot-to-shot variability in the CARS spectra, allowing for accurate temporally resolved thermometry in high-speed flows.

A regenerative fs burst-mode laser was discussed in detail, with the primary motivation being higher energy extraction per pulse for the same amount of amplifying media and same pumping power. Other motivation stems from the nonlinear bandwidth degradation and intensity oscillations of the previous fs laser output, caused by the initial fiber amplifier. With a regenerative design, the fiber amplifier would not be needed for energy because enough passes could extract all the energy needed from the rods to have high energy pulses, eliminating the bandwidth and intensity oscillation problems. Preliminary construction of the system with a ns seed source is underway to iron out the details and avoid unnecessary optical damage due to Kerr lensing or other nonlinear effects.

6. FUTURE WORK

There are several improvements that can be made to the computational model in the near future to improve its fidelity. In general, there is a need for sensitivity analysis to confirm the model is valid for many specific cases. Inserting loss elements in random places and comparing experimental to computational results is a direct approach to this that should yield easily quantifiable results. Other approaches, like comparing to different constructed burst-mode lasers, would also work. Additional improvements will be discussed in some detail in the following subsections.

6.1 Computational Fluid Dynamics Approach

Computational Fluid Dynamics (CFD) involve the application of the governing partial differential equations of fluid flow (i.e. conservation of mass, conservation of momentum, and conservation of energy) to applied fluid dynamic problems [6.1]. The fluid flow is discretized in the form of a mesh with some resolution, and the governing equations are applied at each point to simulate the fluid dynamics of the system. This discretized time and space approach for solving the governing equations can be used in the same fashion for solving solid state lasing equations and other beam propagation equations. This approach can and should be applied to the burst-mode systems described in this dissertation and in future systems.

Most laser propagation models use a lot of assumptions that can generate large errors in outputs. Spectral bandwidths cannot be assumed to be monochromatic and need to have their entire bandwidths accounted for, especially in the case of high-pumped high-density materials that can produce large nonlinear spectral phase perturbations. Assuming uniform temporal pulse shapes and spatial shapes throughout the system can be a huge source of error, since these spectral perturbations can majorly affect the temporal phase of the pulse and the spatial domain. Nonlinear effects, like Kerr lensing and thermal lensing, can greatly affect the fluence of the pulse at each point throughout the rod propagation. A change in fluence can alter the spectral and temporal domains further, and the cycle continues. Additionally, not only will the model be incorrect, but materials can also get damaged in the process.

Figure 6.1 illustrates the discretization of a 2-dimensional slice of some representative amplifying medium. The spectral and temporal domains of an ultrafast pulse are exhibited from a lower energy density portion of the spatial profile (top) and high energy density portion of the spatial profile (bottom). The simulated effect is a dispersion based self-phase modulation, and this exhibition demonstrates how different portions of the spatial domain can have different intensities, and therefore, can have different spectral and temporal lineshapes for a single slice of the rod. Figure 6.2 extends the display into 3-dimensions, separating each 2-dimensional slice by a small incremental length value. The finalized mesh will have some value of resolution in the spatial, temporal, and spectral domains.

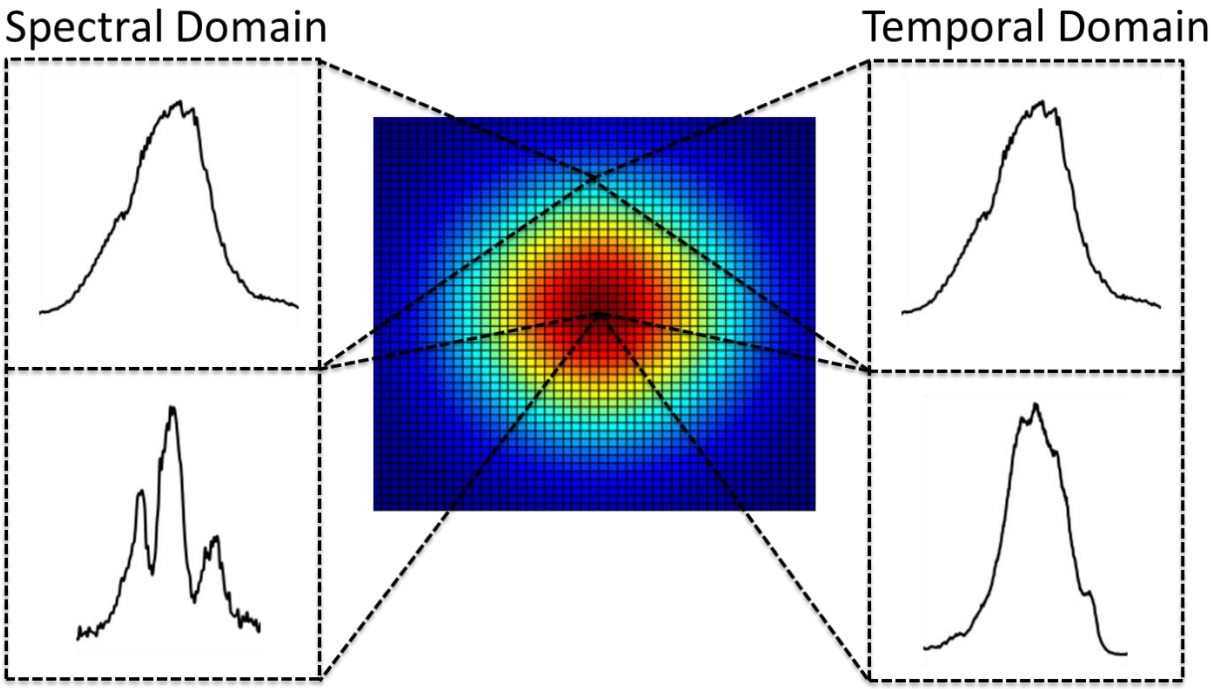

Figure 6.1. A representation of the CFD concept in a 2-dimensional slice of an amplifying medium. The spectral and temporal domains of an ultrafast pulse are exhibited from a lower energy density portion of the spatial profile (top) and high energy density portion of the spatial profile (bottom).

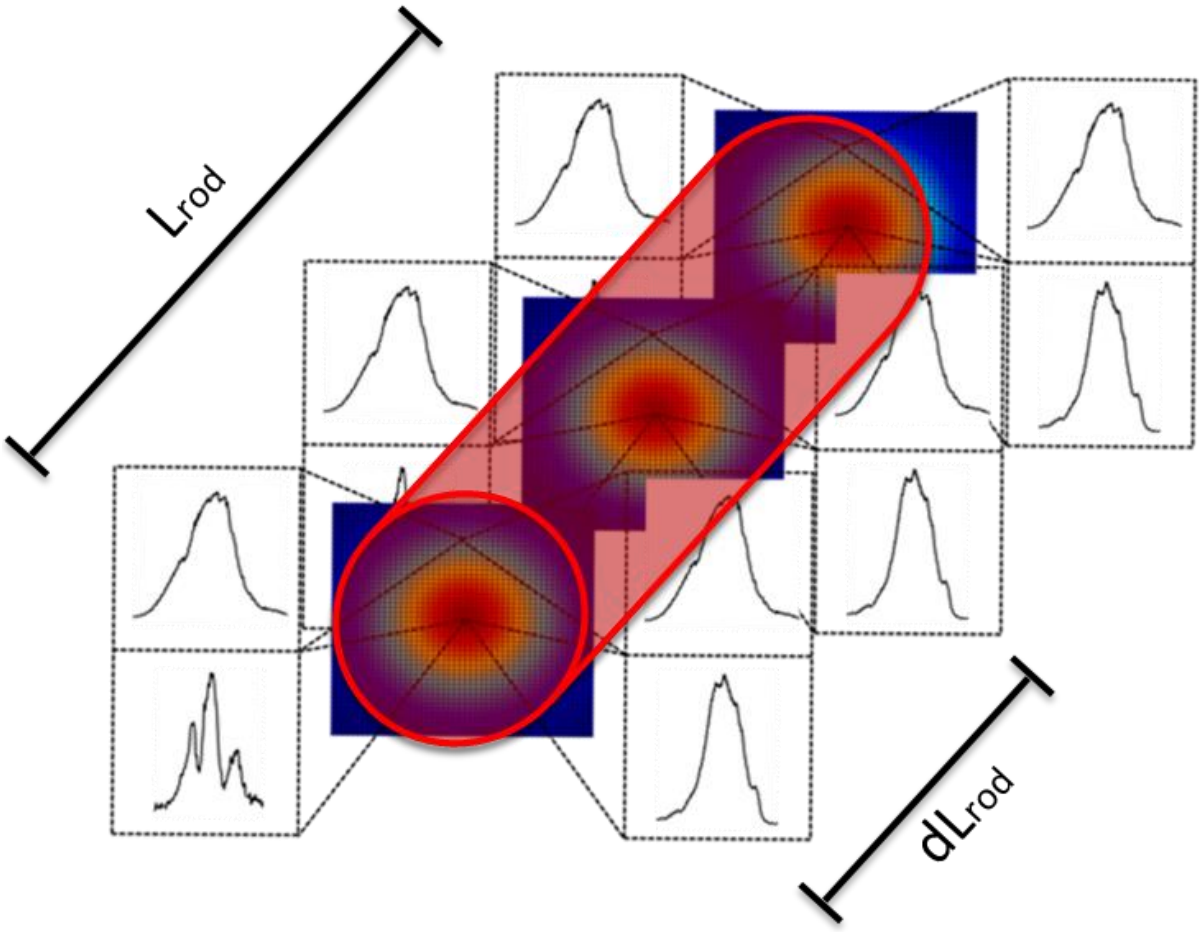

Figure 6.2. A representation of the CFD in 3-dimensions for a rod amplifying medium. The 2-dimensional slices are separated by a small increment in length, dL_{rod}, for the entire length of the rod, L_{rod}.

6.2 Self-Phase Modulation

Self-phase modulation is a phenomenon in which a high irradiance pulse alters the local refractive index of a material via the optical Kerr effect. This refractive index modulation affects the temporal phase of the pulse which causes dynamic shifts in the instantaneous frequency [6.2]. Equations 6.1-6.5 show the steps necessary to calculate self-phase modulation in a system [6.2]. Equation 6.1 depicts the nonlinear propagation equation, where a is the field amplitude, z is the propagation length in the medium, t is the retarded time, β_2 is a 2nd order spectral phase component, and γ is a proportionality constant. By omitting the spectral phase term so that dispersion is neglected, the propagation equation can be transformed into Eq. 6.2, where $\Delta\omega$ is the instantaneous frequency phase shift. The value, $|a|^2$, can be expressed in the form of an output intensity profile

in Eq. 6.3, where τ is the pulse width. The proportionality constant is expanded upon in Eq. 6.4, where ω_0 is the instantaneous frequency, n_0 is the wavelength dependent index of refraction, n_2 is the nonlinear index of refraction, β_0 is the 0^{th} order spectral phase term, and A_{eff} is typically on the order of 1.5 to 2.5 the fiber core area. Equation 6.5 expand upon the 0^{th} order spectral phase component.

$$\frac{\partial a}{\partial z} = \frac{j\beta_2}{2}\frac{\partial^2 a}{\partial t^2} - j\gamma|a|^2 a \tag{6.1}$$

$$\Delta\omega(z,t) = -\frac{\partial}{\partial t} = -\gamma|a|^2 z \tag{6.2}$$

$$|a|^2 = P(t) = \exp\left(-\frac{t^2}{\tau^2}\right) \tag{6.3}$$

$$\gamma = \frac{\omega_0^2 n_0 n_2}{\beta_0 c^2 A_{eff}} \tag{6.4}$$

$$\beta_0 = \frac{\omega n(\omega)}{c} \tag{6.5}$$

The equations here are used in tandem with the method laid out by Finot et al. to get a spectral lineshape similar to what we are experiencing with the ultrafast burst-mode laser inputs [6.3]. The methodology can be seen in Appendix. C. Preliminary results can be seen in Figure 6.3, where the bandwidth clearly resembles a fingering shape for higher B-integral values (similar qualitatively to the experimental findings). The Sellmeier equation was modeled after BAK1 glass since it has similar material properties to Q246 glass, and known laser properties were used. Implementing dispersion will lead to more accurate spectral bandwidth model.

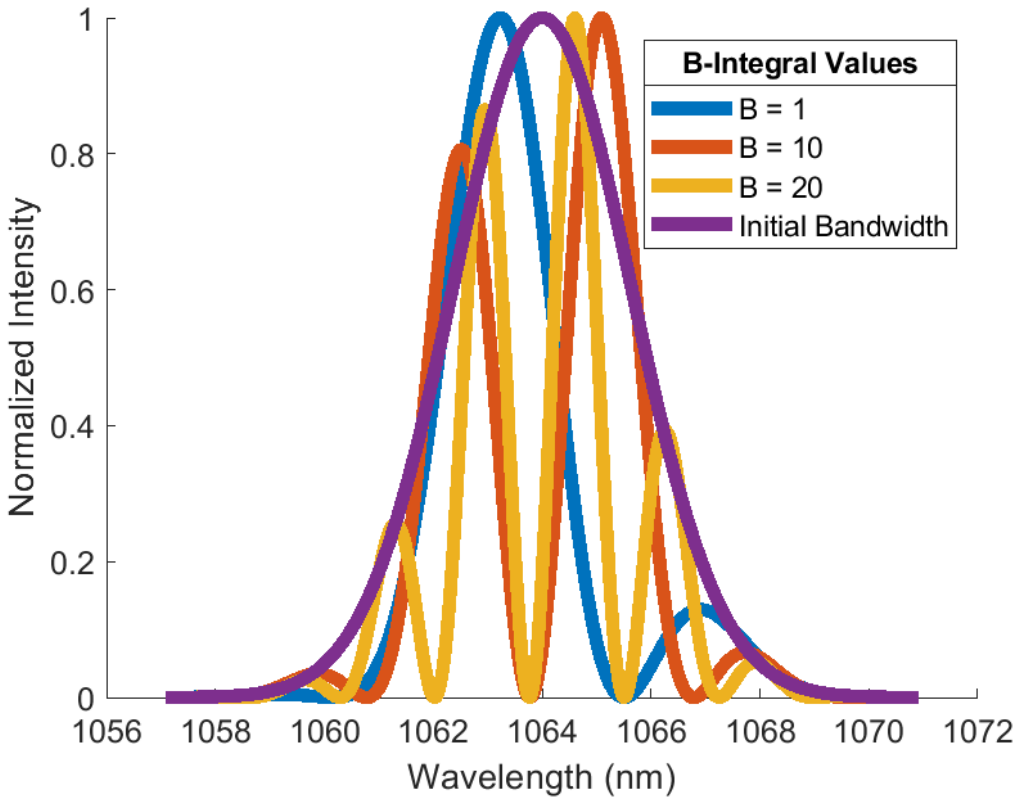

Figure 6.3. Modeled spectral bandwidth for an intense laser pulse after propagating through a laser rod.

Self-phase modulation has been entirely described throughout this dissertation as a problematic phenomenon, but it can also be used to some advantage. It has been widely shown that the frequency domain can be spectrally broadened in solid lasing elements like free space amplifiers and fibers, and it has also been demonstrated in liquids and gases. Applying a physics package that can predict accurate bandwidth broadening in a gaseous environment would be instrumental in generating RCARS in many environments, especially flames that require large bandwidths for low uncertainty resolution.

6.3 Nonlinear Thermal Effects

Solid state lasing elements operating in any capacity will dissipate heat. The thermal conductivity of the material, the pumping rate, and the coolant involved all play a role in the temperature and quantum properties of the lasing element. Two thermal related phenomena are of

immediate interest and can greatly benefit the model's fidelity – thermal lensing and thermally dependent stimulated emission cross sections.

Thermal lensing is the phenomenon in which a laser rod causes thermal distortion of the laser beam due to temperature and stress dependent variation of the refractive index [6.4]. This is often prompted by a circumferential cooling of a cylindrical rod causing a radial thermal gradient in the material. Figure 6.4 displays how the temperature dependent refractive index causes a collimated light beam to bend through the medium. This is of particular interest to the regenerative cavity since thermal lensing changes the required cavity length for optimal stability.

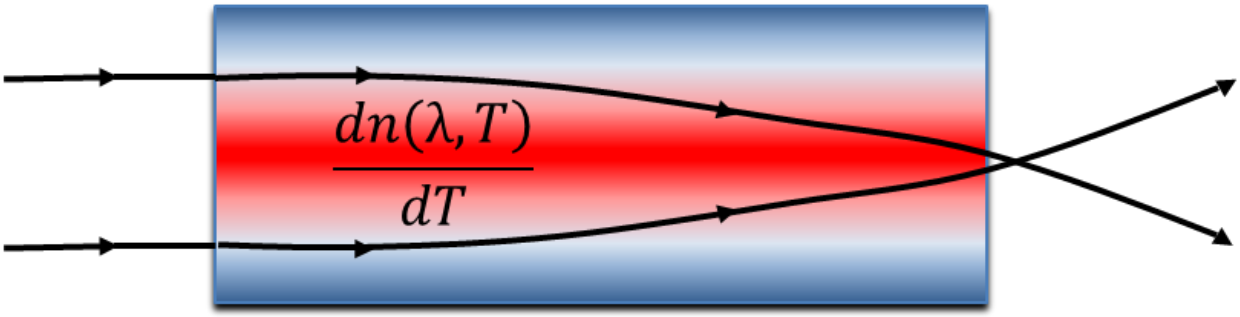

Figure 6.4. A representation of the wavelength and temperature dependent refractive index changing with temperature and causing a lensing effect.

Using a series of equations laid out by Koechner [6.5], the radial index of refraction can be modeled based off pumping power. In this model, we assume that the heat generated in the rod is directly proportional to the power input to the flashlamps, and that that water coolant is negligible during the burst. Equations 6.6 and 6.7 show the index of refraction radial dependence due to thermal additions. In Eq. 6.6, $n_0(\lambda)$ is the steady state wavelength depending index of refraction found from a Sellmeier equation, $\frac{\delta n(\lambda,T)}{\delta T}$ is a known material property, T(r) is the radially dependent temperature, and T_0 is the steady state temperature. In Eq. 6.7, η is the fraction of the electrical input power, P_{in}, which is dissipated as heat by the rod, r is the radial distance from the center, K is the material thermal conductivity, L is the length of the rod, and r_0 is the radius of the rod. Kushner documented fractional heat dissipation from total electrical input power for xenon based flashlamps [6.5].

$$n(r,\lambda) = n_0(\lambda) + \frac{\delta n(\lambda,T)}{\delta T}[T(r) - T_0] \quad 6.6$$

$$T(r) - T_0 = \frac{\eta P_{in} r^2}{4K\pi L r_0^2} \quad 6.7$$

Thermally dependent stimulated emission cross sections work in tandem with the maximum average thermal load that the solid state lasing elements can tolerate in limiting the output of a burst-mode laser. The Nd:YAG stimulated emission cross section temperature dependence was documented by Rapaport et al.[6.6], and phosphate doped Nd:glass stimulated emission cross section temperature dependence was documented by Dong et al. [6.7]. Both show approximately linear fits, where the cross section decreases as temperature increases, indicating that it is better to pump colder rods. The radial temperature calculated in Eq. 6.7 can be applied to this concept and adapted to the overall model.

6.4 Errors in Wavefront Propagation

The quality of the beam is an important parameter to keep track of, especially for the sake of predicting accurate laser diagnostics. An amplified beam with poor beam quality will not focus its energy to a Gaussian spot necessarily, and the spot size can vary greatly from the diffraction limited spot size due to optically induced deviations from a perfect wavefront. This will affect the signal generation of techniques like FLEET and CARS greatly, since they depend on input irradiance nonlinearly.

Deviations occur due to an optical path difference between an aberrated wavefront and ideal unaberrated wavefront [6.8]. Since the incident laser beam for all optical interactions is nearly collimated, only on-axis aberrations need to be considered, greatly simplifying the wavefront propagation analysis. Simple first order aberrations like tilt, defocus, and piston, can also be neglected as they are simply errors in magnification, image plane location, and phase, respectively. These can each be corrected for with relative ease. The only on-axis 3rd order optical aberration, spherical aberration, exists (like the other aberrations) because of errors in the paraxial approximation. Rays close to the pupil edge converge faster, proportional to the entrance pupil diameter to the 4th power. An example of this can be seen in Figure 6.5a and b. Figure 6.5a shows a system with no induced aberrations, and each ray focuses to a perfect diffraction limited point.

Figure 6.5b shows how spherical aberration affects the system, causing rays farther from the central vertex of the lens to focus quicker.

Different wavelengths interact with electric susceptibility of materials differently. This gives rise to a wavelength dependent index of refraction, or material dispersion. Due to material dispersion, different wavelengths refract at different angles at the same optical interface. This results in different focal points for different wavelengths from the same lens, called chromatic dispersion. Off-axis broadband light will be discounted again, so the on-axis light will produce axial chromatic dispersion, shown in Figure 6.5c and d. Figure 6.5c shows a system with no induced chromatic dispersion, and each color focuses to the same location. Figure 6.5d depicts axial chromatic dispersion, and shorter wavelengths typically refract at a larger angle and focus closer.

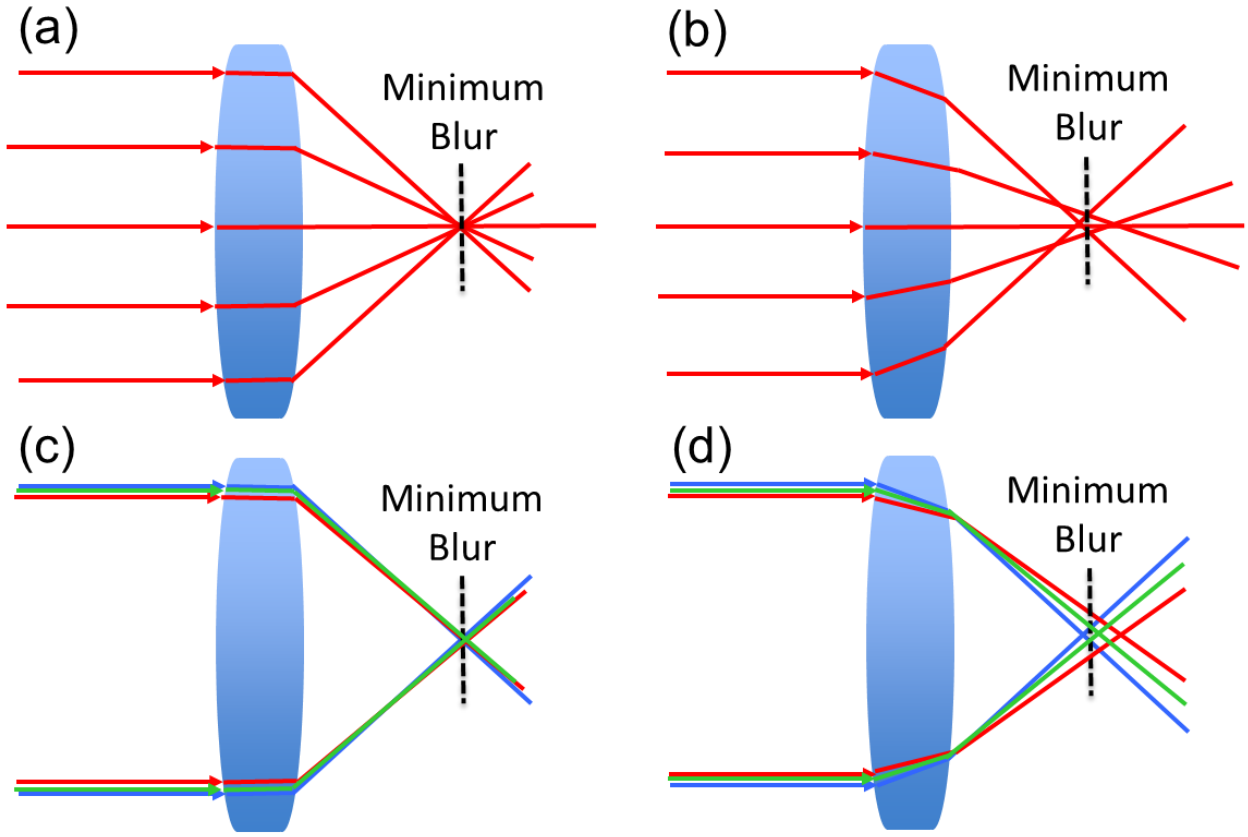

Figure 6.5. A comparison between perfect optical wavefronts and distorted wavefronts: (a) A perfect monochromatic wavefront focusing to a tight spot; (b) A representation of spherical aberration affecting the minimum blur spot size; (c) A perfect broadband wavefront focusing to a tight spot; and (d) A representation of axial chromatic dispersion affecting the minimum blur spot size.

We can utilize the CFD idea to this concept's advantage. Since the beam is already being spectrally and temporally accounted for at each small mesh area through amplification, the spatial domain has already been constructed. The same concept can be continued throughout the system. All lenses and other optical components in the system have known parameters, and Sellmeier equations can be used to identify material dispersion. For spatial filtering purposes, a super Gaussian function can be applied across the spatial domain, and the beam can be assumed to be perfectly re-collimated entering the next rod to avoid other optical aberration calculations.

At the output of the laser, the beam can have its spatial quality quantified by using a series of equations published by Siegman [6.9]. However, the domains that are already being meticulously tracked can be tracked through any exterior focusing lens, and the time-averaged spectral domain and intensity can be catalogued over a focusing distance. The D4σ beam diameter and wavelength dependent focal shifts can be calculated, and this can be compared to the theoretical diffraction limited spot size for a quantitative and predictive M^2 output.

6.5 References

[6.1] J. Wendt, J. Anderson, G. Degrez, J. Degroote, E. Dick, R. Grundmann, and J. Vierendeels, *Computational Fluid Dynamics*, 3rd Ed. (Springer Berlin, 2009).

[6.2] A. Weiner, *Ultrafast Optics*, (John Wiley & Sons, Inc. 2009).

[6.3] C. Finot, F. Chaussard, and S. Boscolo, "Simple guidelines to predict self-phase modulation patterns." J. Opt. Soc. Am. B **35**, 3143-3152, (2018).

[6.4] W. Koechner, "Thermal Lensing in a Nd:YAG Laser Rod," Appl. Opt. **9**, 2548-2553, (1970).

[6.5] M. Kushner, "Arc expansion in xenon flashlamps." Journal of Applied Physics **57**, 2486-2500, (1985).

[6.6] A. Rapaport, S. Zhao, G. Xiao, A. Howard, and M. Bass, "Temperature dependence of the 1.06-μm stimulated emission cross section of neodymium in YAG and in GSGG." Appl. Opt. **41**, 7052-7057, (2002).

[6.7] J. Dong, M. Bass, and C. Walters, "Temperature-dependent stimulated-emission cross section and concentration quenching in Nd^{3+} -doped phosphate glasses." J. Opt. Soc. Am. B **21**, 454-457, (2004).

[6.8] J. Wyant and K. Creath, *Basic wavefront Aberration Theory for Optical Metrology*, (Academic Press, Inc., 1992).

[6.9] A. Siegman, "Analysis of laser beam quality degradation caused by quartic phase aberrations," Appl. Opt. **32**, 5893-5901 (1993).

APPENDIX A. BURST-MODE MODEL CODE

```
clc, clear, close all

cprintf('_red','Let''s build a laser! We will start with pulse input parameters. \n') %initial
statement to begin
lambda_0_laser = input('Please enter your laser''s central wavelength in meters: '); %central
wavelength input
pulse_width = input('Please enter the initial pulse width of your laser in seconds: '); %pulse
width input
bandwidth = input('Please enter the initial bandwidth of your laser in meters: '); %laser
bandwidth input
beam_diameter = input('Please enter the intial beam diameter of your laser in meters: '); %laser
beam diameter input

[laser_pulse_width_0, laser_bandwidth, laser_spatial, lambda, time, space,increment] =
time_bandwidth_spatial_input(lambda_0_laser, pulse_width, bandwidth, beam_diameter);

figure() %Creates a normalized plot for input pulse frequency domain
subplot(2,1,1)
plot(lambda,laser_bandwidth)
title('Input Pulse Frequency Domain')
xlabel('Wavelength (m)')
ylabel('Normalized Intensity')
xlim([lambda_0_laser-bandwidth lambda_0_laser+bandwidth])
ylim([0 1])
set(gcf, 'color', 'w');

subplot(2,1,2) %Creates a normalized plot for input pulse temporal domain
plot(time,laser_pulse_width_0)
```

```
title('Input Pulse Temporal Domain')
xlabel('time (s)')
ylabel('Normalized Intensity')
xlim([-pulse_width pulse_width])
ylim([0 1])
set(gcf, 'color', 'w');

figure() %Creates a spatial plot of the initial beam
x = linspace(-beam_diameter,beam_diameter,length(laser_spatial));
y = linspace(-beam_diameter,beam_diameter,length(laser_spatial));
[X,Y] = meshgrid(x,y);
R = laser_spatial;
surf(R,'Edgecolor','None')
view(2);
pcolor(X,Y,R)
colormap(jet)
title('Input Pulse Spatial Profile')
xlabel('Distance from Center (m)')
ylabel('Distance from Center (m)')
colorbar
set(gcf, 'color', 'w');
laser_pulse_width = laser_pulse_width_0;
clc

cprintf('_red','Now we will need system parameters! \n')
rep_rate = input('Please enter your repetition rate in Hz (e.g. 1 MHz = 1000000): '); %rep rate
input
burst_length = input('Please enter your burst length in seconds: '); %burst duration input
cw_power = input('Please enter your seed input power in Watts: '); %beam initial cw power input
pulses = burst(burst_length,rep_rate); %calculated total pulses to keep track of time
```

```
input_energy_dummy = energy(cw_power, rep_rate)./(pi*(beam_diameter/2)^2); %scalar fluence/pulse
cw_energy_individual = input_energy_dummy.*laser_bandwidth; %dummy fluence per wavelength
cw_pulse = trapz(lambda, cw_energy_individual); %dummy pulse power
cw_energy_individual = cw_energy_individual.*input_energy_dummy./cw_pulse; %corrected fluence per wavelength
cw_pulse = trapz(lambda, cw_energy_individual); %corrected pulse power for verification
input_energy = repmat(input_energy_dummy, pulses,1); %creates scalar initial values for all pulses in burst for passes function
clc

% Before First Rod

cprintf('_red','It is time to build the first leg of the laser! \n')
loss = input('Is there a loss element before your rod? Hit 1 for yes and 0 for no: '); %asking if there are losses before first rod
while (loss ~= 0) && (loss ~= 1) %loops code until you press 0 or 1
    clc
    cprintf('blue','You didn''t input 0 or 1. \n')
    loss = input('Is there a loss element before your rod? Hit 1 for yes and 0 for no: ');
end
loss_element_initial = []; %Establish initial loss element matrix. This particular matrix is crucial for loss element matrix.
if loss == 0 %Defines no loss elements as a 0 in matrix
    loss_element_initial = [loss_element_initial,0];
end
while loss == 1 %loop for loss elements before first rod
    specific_loss = input('Enter 1 for OI, 2 for spatial_filter, or 3 for PBS: '); %asking for specific loss elements
```

```
    while (specific_loss ~= 1) && (specific_loss ~= 2) && (specific_loss ~= 3) %loops code until
you press the right thing
        clc
        cprintf('blue','You didn''t input 1, 2, or 3. \n')
        specific_loss = input('Enter 1 for OI, 2 for spatial_filter, or 3 for PBS: ');
    end
    if specific_loss == 1
        loss_element_initial = [loss_element_initial, losses(1)];
        cprintf('blue','You''ve chosen an OI \n')
    elseif specific_loss == 2
        loss_element_initial = [loss_element_initial, losses(2)];
        cprintf('blue','You''ve chosen a spatial filter \n')
    elseif specific_loss == 3
        loss_element_initial = [loss_element_initial, losses(3)];
        cprintf('blue','You''ve chosen a PBS \n')
    end
    loss = input('Is there another loss element before your rod? Hit 1 for yes and 0 for no:
'); %Asking if there are more loss elements before first rod
    while (loss ~= 0) && (loss ~= 1) %loops until you press the right thing
        clc
        cprintf('blue','You didn''t input 0 or 1. \n')
        loss = input('Is there another loss element before your rod? Hit 1 for yes and 0 for no: ');
    end
end

clc

% First Leg
% First Rod

cprintf('_red','Rod 1 \n')
```

```
m = 1; %leg count
rod_diameter = {}; %establish rod_diameter cell
rod_diameter_dummy = []; %establish rod_diameter matrix dummy
distance = {}; %establish distance cell
distance_dummy = []; %establish dummy distance matrix
ssg = {}; %establish small-signal gain (ssg) cell for tracking ssg through legs
ssg_dummy = []; %establish dummy matrix for tracking ssg through this leg
rod_prop = {}; %establish rod property cell for tracking rod properties through legs
rod_prop_dummy = []; %establish dummy matrix for tracking rod properties through this leg
rod_length = {}; %establish rod length cell for tracking rod lengths through legs
rod_length_dummy = []; %establish dummy matrix for tracking rod lengths through this leg
loss_element = {}; %establish loss element cell for tracking loss elements through legs
ssg_prompt = input('Enter this rod"s maximum small-signal-gain: '); %ssg input for first rod
ssg_dummy = [ssg_dummy, small_signal_gain(ssg_prompt, burst_length, pulses)]; %adding to
ssg dummy matrix
rod_prop_dummy=[rod_prop_dummy,input('Enter 1 for Nd:YAG or 2 for q246 material
properties for this rod: ')]; %rod  property input
for i = 1:length(rod_prop_dummy) %loops until you press the right thing
   while (rod_prop_dummy(i,1) ~= 1) && (rod_prop_dummy(i,1) ~= 2)
      clc
      disp('You didn"t input 1 or 2.')
      rod_prop_dummy(i,1)=input('Enter 1 for Nd:YAG or 2 for q246 material properties for this
rod: ');
   end
end
rod_length_dummy = [rod_length_dummy,input('Enter this rod"s length in meters: ')]; %adding
to rod length dummy matrix
rod_diameter_dummy = [rod_diameter_dummy,input('Enter this rod"s diameter in meters: ')];
[c,h,delta_lambda,lambda_0_prop,density,M,M_p,kb,A21, sigma_se] =
Matprops(rod_prop_dummy); %calling rod properties
loss_element_added = []; %establish matrix to add to the loss element matrix
```

```
loss = input('Is there a loss element after your rod? Hit 1 for yes and 0 for no: '); %asking for losses after this first rod
while (loss ~= 0) && (loss ~= 1) %loops until you press the right thing
    clc
    disp('You didn''t input 0 or 1, dumbass.')
    loss = input('Is there a loss element after your rod? Hit 1 for yes and 0 for no: ');
end
if loss == 0
    while length(loss_element_initial)>length(loss_element_added)
        loss_element_added = [loss_element_added,0];
    end
end
while loss == 1
    specific_loss = input('Enter 1 for OI, 2 for spatial_filter, or 3 for PBS: ');
    while (specific_loss ~= 1) && (specific_loss ~= 2) && (specific_loss ~= 3) %loops until you press the right thing
        clc
        disp('You didn''t input 1, 2, or 3, dumbass.')
        specific_loss = input('Enter 1 for OI, 2 for spatial_filter, or 3 for PBS: ');
    end
    if specific_loss == 1
        loss_element_added = [loss_element_added, losses(1)];
        disp('You''ve chosen an OI')
    elseif specific_loss == 2
        loss_element_added = [loss_element_added, losses(2)];
        disp('You''ve chosen a spatial filter')
    elseif specific_loss == 3
        loss_element_added = [loss_element_added, losses(3)];
        disp('You''ve chosen a PBS')
    end
    while length(loss_element_initial)<length(loss_element_added)
```

```
        loss_element_initial = [loss_element_initial,0];
    end
    loss = input('Is there another loss element after your rod? Hit 1 for yes and 0 for no: ');
    while (loss ~= 0) && (loss ~= 1) %loops until you press the right thing
        clc
        disp('You didn''t input 0 or 1, dumbass.')
        loss = input('Is there another loss element after your rod? Hit 1 for yes and 0 for no: ');
    end
end
while length(loss_element_initial)>length(loss_element_added)
    loss_element_added = [loss_element_added,0];
end
loss_element_dummy = [loss_element_initial;loss_element_added];

% Consecutive rods

rod_prompt = input('Is there another rod in the leg? Hit 1 for yes and 0 for no: ');
while (rod_prompt ~= 0) && (rod_prompt ~= 1) %loops until you press the right thing
    clc
    disp('You didn''t input 0 or 1.')
    rod_prompt = input('Is there another rod in the leg? Hit 1 for yes and 0 for no: ');
end
k = 1;
while rod_prompt == 1
    clc
    disp(['Rod ', num2str(k+1)])
    loss_element_added = [];
    ssg_prompt = input('Enter this rod''s maximum small-signal-gain: ');
    ssg_dummy = [ssg_dummy; small_signal_gain(ssg_prompt, burst_length, pulses)];
    rod_prop_dummy=[rod_prop_dummy; input('Enter 1 for Nd:YAG or 2 for q246 material
properties for this rod: ')];
```

```
    while (rod_prop_dummy(k+1,1) ~= 1) && (rod_prop_dummy(k+1,1) ~= 2) %loops until you
press the right thing
        clc
        disp('You didn''t input 1 or 2.')
        rod_prop_dummy(k+1,1)=input('Enter 1 for Nd:YAG or 2 for q246 material properties for
this rod: ');
    end
    [c,h,delta_lambda,lambda_0_prop,density,M,M_p,kb,A21,
sigma_se]=Matprops(rod_prop_dummy(k+1,1));
    rod_length_dummy = [rod_length_dummy,input('Enter this rod''s length in meters: ')];
    rod_diameter_dummy = [rod_diameter_dummy,input('Enter this rod''s diameter in meters: ')];
    distance_dummy = [distance_dummy,input('Enter the distance between this rod and the
previous rod in meters: ')];
    loss = input('Is there a loss element after your rod? Hit 1 for yes and 0 for no: ');
    while (loss ~= 0) && (loss ~= 1) %loops until you press the right thing
        clc
        disp('You didn''t input 0 or 1.')
        loss = input('Is there a loss element after your rod? Hit 1 for yes and 0 for no: ');
    end
    if loss == 0
        while length(loss_element_initial)>length(loss_element_added)
            loss_element_added = [loss_element_added,0];
        end
    end
    while loss == 1
        specific_loss = input('Enter 1 for OI, 2 for spatial_filter, or 3 for PBS: ');
        while (specific_loss ~= 1) && (specific_loss ~= 2) && (specific_loss ~= 3) %loops until
you press the right thing
            clc
            disp('You didn''t input 1, 2, or 3.')
            specific_loss = input('Enter 1 for OI, 2 for spatial_filter, or 3 for PBS: ');
```

```
    end
    if specific_loss == 1
      loss_element_added = [loss_element_added, losses(1)];
      disp('Youve chosen an OI')
    elseif specific_loss == 2
       loss_element_added = [loss_element_added, losses(2)];
       disp('Youve chosen a spatial filter')
    elseif specific_loss == 3
       loss_element_added = [loss_element_added, losses(3)];
       disp('Youve chosen a PBS')
    end
    while length(loss_element_dummy(1,:))<length(loss_element_added)
       nada = zeros(1,length(loss_element_dummy));
       loss_element_dummy = [loss_element_dummy,nada'];
    end
    loss = input('Is there another loss element after your rod? Hit 1 for yes and 0 for no: ');
    while (loss ~= 0) && (loss ~= 1) %loops until you press the right thing
       clc
       disp('You didn''t input 0 or 1.')
       loss = input('Is there another loss element after your rod? Hit 1 for yes and 0 for no: ');
    end
end
while length(loss_element_dummy(1,:))>length(loss_element_added)
    loss_element_added = [loss_element_added,0];
end
loss_element_dummy = [loss_element_dummy;loss_element_added];
disp(['This leg now has ', num2str(k+1), ' rods'])
rod_prompt = input('Is there another rod in the leg? Hit 1 for yes and 0 for no: ');
while (rod_prompt ~= 0) && (rod_prompt ~= 1) %loops until you press the right thing
    clc
    disp('You didn''t input 0 or 1.')
```

```
        rod_prompt = input('Is there another rod in the leg? Hit 1 for yes and 0 for no: ');
    end
    k = k + 1;
end

ssg(1,m) = {ssg_dummy};
rod_prop(1,m) = {rod_prop_dummy};
rod_length(1,m) = {rod_length_dummy};
rod_diameter(1,m) = {rod_diameter_dummy};
loss_element(1,m) = {loss_element_dummy};

clc
mode = input('Is this a single-pass, double pass, or regen? Hit 1 for single, 2 for double, or 3 for
regen: ');
if mode == 2
    distance_dummy = [distance_dummy,input('Enter the distance between this rod and the
previous rod in meters: ')];
    distance(1,m) = {distance_dummy};
end
[Gaussian_prop,Gaussian_final_prop,Es_correct,Es_max,Es,Es_check,P,E_stored,scatter_y,lamb
da,output_energy,output_time] =
Passes(rod_diameter,rod_prop,lambda,ssg,pulses,mode,rod_length,loss_element,rep_rate,input_e
nergy,lambda_0_laser, bandwidth,m,laser_pulse_width,time,distance,pulse_width);

% Losses between legs

loss_element_added = [];
loss = input('Is there a loss element after this leg? Hit 1 for yes and 0 for no: ');
while (loss ~= 0) && (loss ~= 1) %loops until you press the right thing
    clc
    disp('You didn''t input 0 or 1.')
```

```
    loss = input('Is there a loss element after this leg? Hit 1 for yes and 0 for no: ');
end
if loss == 0
    while length(loss_element_initial)>length(loss_element_added)
        loss_element_added = [loss_element_added,0];
    end
end
while loss == 1
    specific_loss = input('Enter 1 for OI, 2 for spatial_filter, or 3 for PBS: ');
    while (specific_loss ~= 1) && (specific_loss ~= 2) && (specific_loss ~= 3) %loops until you
press the right thing
        clc
        disp('You didn''t input 1, 2, or 3.')
        specific_loss = input('Enter 1 for OI, 2 for spatial_filter, or 3 for PBS: ');
    end
    if specific_loss == 1
       loss_element_added = [loss_element_added, losses(1)];
       disp('Youve chosen an OI')
    elseif specific_loss == 2
        loss_element_added = [loss_element_added, losses(2)];
        disp('Youve chosen a spatial filter')
    elseif specific_loss == 3
        loss_element_added = [loss_element_added, losses(3)];
        disp('Youve chosen a PBS')
    end
    while length(loss_element_dummy(1,:))<length(loss_element_added)
        nada = zeros(1,length(loss_element_dummy));
        loss_element_dummy = [loss_element_dummy,nada'];
    end
    loss = input('Is there another loss element after this leg? Hit 1 for yes and 0 for no: ');
    while (loss ~= 0) && (loss ~= 1) %loops until you press the right thing
```

```
        clc
        disp('You didn''t input 0 or 1.')
        loss = input('Is there another loss element after this leg? Hit 1 for yes and 0 for no: ');
    end
end
while length(loss_element_initial)>length(loss_element_added)
    loss_element_added = [loss_element_added,0];
end
loss_element_dummy = [loss_element_dummy;loss_element_added];
for i = 1:length(loss_element_dummy(end,:))
    if loss_element_dummy(end,i) > 0
        output_energy = output_energy.*loss_element_dummy(end,i);
        scatter_y = scatter_y.*loss_element_dummy(end,i);
    end
end

% More Legs

leg_prompt = input('Is there another leg in the laser? Hit 1 for yes and 0 for no: ');
while (leg_prompt ~= 0) && (leg_prompt ~= 1) %loops until you press the right thing
    clc
    disp('You didn''t input 0 or 1.')
    leg_prompt = input('Is there another leg in the laser? Hit 1 for yes and 0 for no: ');
end

if leg_prompt == 0
    scatter_x = linspace(1, pulses, pulses)*burst_length;
    figure()
    scatter(scatter_x,scatter_y*pi*(beam_diameter/2)^2);
    set(gcf, 'color', 'w');
    title('Output Burst Profile')
```

```
xlabel('Time (ms)')
ylabel('Energy/Pulse (J)')

figure()
subplot(2,1,1)
hold on
bandwidth_plot = output_energy(end,:)/max(output_energy(end,:));
plot(lambda, laser_bandwidth, '-k', 'Linewidth', 2)
plot(lambda,bandwidth_plot, '--r', 'Linewidth', 2)
title('Frequency Domain')
xlabel('Wavelength (m)')
ylabel('Normalized Intensity')
legend('Input Bandwidth','Final Bandwidth')
legend('Location','south')
legend('boxoff')
hold off
k = 1;
while bandwidth_plot(1,k)<.1
    k = k + 1;
end
xlim_low = lambda(1,k);
k = length(bandwidth_plot);
while bandwidth_plot(1,k)<.1
    k = k - 1;
end
xlim_high = lambda(1,k);
xlim([xlim_low xlim_high])
ylim([0 1])
set(gcf, 'color', 'w');
set(gca,'FontSize',12)
subplot(2,1,2)
```

```
    hold on
    pulse_width_plot = output_time(:,end)/max(output_time(:,end));
    plot(time,laser_pulse_width_0, '-k', 'Linewidth', 2)
    plot(time, pulse_width_plot,'--r', 'Linewidth', 2)
    title('Temporal Domain')
    xlabel('Time (s)')
    ylabel('Normalized Intensity')
    legend('Input Pulse Width','Final Pulse Width')
    legend('Location','south')
    legend('boxoff')
    set(gca,'FontSize',12)
%     title(legend, 'Temporal Pulse Widths')
    hold off
end

while leg_prompt == 1
    m = m + 1;
    input_energy = output_energy;
    laser_pulse_width = output_time(:,end);
    disp(['Leg ', num2str(m)])
    loss = input('Is there a loss element before your first rod? Hit 1 for yes and 0 for no: ');
    while (loss ~= 0) && (loss ~= 1) %loops until you press the right thing
        clc
        disp('You didn''t input 0 or 1.')
        loss = input('Is there a loss element before your rod? Hit 1 for yes and 0 for no: ');
    end
    loss_element_initial = [];
    if loss == 0
        loss_element_initial = [loss_element_initial,0];
    end
    while loss == 1
```

```
        specific_loss = input('Enter 1 for OI, 2 for spatial_filter, or 3 for PBS: ');
        while (specific_loss ~= 1) && (specific_loss ~= 2) && (specific_loss ~= 3) %loops until
you press the right thing
            clc
            disp('You didn''t input 1, 2, or 3.')
            specific_loss = input('Enter 1 for OI, 2 for spatial_filter, or 3 for PBS: ');
        end
        if specific_loss == 1
            loss_element_initial = [loss_element_initial, losses(1)];
            disp('You''ve chosen an OI')
        elseif specific_loss == 2
            loss_element_initial = [loss_element_initial, losses(2)];
            disp('You''ve chosen a spatial filter')
        elseif specific_loss == 3
            loss_element_initial = [loss_element_initial, losses(3)];
            disp('You''ve chosen a PBS')
        end
        loss = input('Is there another loss element before your rod? Hit 1 for yes and 0 for no: ');
        while (loss ~= 0) && (loss ~= 1) %loops until you press the right thing
            clc
            disp('You didn''t input 0 or 1.')
            loss = input('Is there another loss element before your rod? Hit 1 for yes and 0 for no: ');
        end
    end
    clc

    disp('Rod 1')
    ssg_dummy = [];
    rod_prop_dummy = [];
    rod_length_dummy = [];
    rod_diameter_dummy = [];
```

```
    ssg_prompt = input('Enter this rod"s maximum small-signal-gain: ');
    ssg_dummy = [ssg_dummy, small_signal_gain(ssg_prompt, burst_length, pulses)];
    rod_prop_dummy=[rod_prop_dummy,input('Enter 1 for Nd:YAG or 2 for q246 material
properties for this rod: ')];
    for i = 1:length(rod_prop_dummy)
        while (rod_prop_dummy(i,1) ~= 1) && (rod_prop_dummy(i,1) ~= 2) %loops until you
press the right thing
            clc
            disp('You didn"t input 1 or 2.')
            rod_prop_dummy(i,1)=input('Enter 1 for Nd:YAG or 2 for q246 material properties for
this rod: ');
        end
    end
    rod_length_dummy = [rod_length_dummy,input('Enter this rod"s length in meters: ')];
    rod_diameter_dummy = [rod_diameter_dummy,input('Enter this rod"s diameter in meters: ')];
    [c,h,delta_lambda,lambda_0_prop,density,M,M_p,kb,A21, sigma_se] =
Matprops(rod_prop_dummy);
    loss_element_added = [];
    loss = input('Is there a loss element after your rod? Hit 1 for yes and 0 for no: ');
    while (loss ~= 0) && (loss ~= 1) %loops until you press the right thing
        clc
        disp('You didn"t input 0 or 1.')
        loss = input('Is there a loss element after your rod? Hit 1 for yes and 0 for no: ');
    end
    if loss == 0
        while length(loss_element_initial)>length(loss_element_added)
            loss_element_added = [loss_element_added,0];
        end
    end
    while loss == 1
        specific_loss = input('Enter 1 for OI, 2 for spatial_filter, or 3 for PBS: ');
```

```
    while (specific_loss ~= 1) && (specific_loss ~= 2) && (specific_loss ~= 3) %loops until
you press the right thing
        clc
        disp('You didn"t input 1, 2, or 3.')
        specific_loss = input('Enter 1 for OI, 2 for spatial_filter, or 3 for PBS: ');
    end
    if specific_loss == 1
        loss_element_added = [loss_element_added, losses(1)];
        disp('You"ve chosen an OI')
    elseif specific_loss == 2
        loss_element_added = [loss_element_added, losses(2)];
        disp('You"ve chosen a spatial filter')
    elseif specific_loss == 3
        loss_element_added = [loss_element_added, losses(3)];
        disp('You"ve chosen a PBS')
    end
    while length(loss_element_initial)<length(loss_element_added)
        loss_element_initial = [loss_element_initial,0];
    end
    loss = input('Is there another loss element after your rod? Hit 1 for yes and 0 for no: ');
    while (loss ~= 0) && (loss ~= 1) %loops until you press the right thing
        clc
        disp('You didn"t input 0 or 1.')
        loss = input('Is there another loss element after your rod? Hit 1 for yes and 0 for no: ');
    end
end
while length(loss_element_initial)>length(loss_element_added)
    loss_element_added = [loss_element_added,0];
end
loss_element_dummy = [loss_element_initial;loss_element_added];
```

```
% Consecutive rods

rod_prompt = input('Is there another rod in the leg? Hit 1 for yes and 0 for no: ');
while (rod_prompt ~= 0) && (rod_prompt ~= 1) %loops until you press the right thing
    clc
    disp('You didn''t input 0 or 1.')
    rod_prompt = input('Is there another rod in the leg? Hit 1 for yes and 0 for no: ');
end
k = 1;
while rod_prompt == 1
    clc
    disp(['Rod ', num2str(k+1)])
    loss_element_added = [];
    ssg_prompt = input('Enter this rod''s maximum small-signal-gain: ');
    ssg_dummy = [ssg_dummy; small_signal_gain(ssg_prompt, burst_length, pulses)];
    rod_prop_dummy=[rod_prop_dummy; input('Enter 1 for Nd:YAG or 2 for q246 material
properties for this rod: ')];
    while (rod_prop_dummy(k+1,1) ~= 1) && (rod_prop_dummy(k+1,1) ~= 2) %loops until
you press the right thing
        clc
        disp('You didn''t input 1 or 2.')
        rod_prop_dummy(k+1,1)=input('Enter 1 for Nd:YAG or 2 for q246 material properties
for this rod: ');
    end
    [c,h,delta_lambda,lambda_0_prop,density,M,M_p,kb,A21,
sigma_se]=Matprops(rod_prop_dummy(k+1,1));
    rod_length_dummy = [rod_length_dummy,input('Enter this rod''s length in meters: ')];
    rod_diameter_dummy = [rod_diameter_dummy,input('Enter this rod''s diameter in meters:
')];
    loss = input('Is there a loss element after your rod? Hit 1 for yes and 0 for no: ');
    while (loss ~= 0) && (loss ~= 1) %loops until you press the right thing
```

```
        clc
        disp('You didn''t input 0 or 1.')
        loss = input('Is there a loss element after your rod? Hit 1 for yes and 0 for no: ');
    end
    if loss == 0
        while length(loss_element_initial)>length(loss_element_added)
            loss_element_added = [loss_element_added,0];
        end
    end
    while loss == 1
        specific_loss = input('Enter 1 for OI, 2 for spatial_filter, or 3 for PBS: ');
        while (specific_loss ~= 1) && (specific_loss ~= 2) && (specific_loss ~= 3) %loops until
you press the right thing
            clc
            disp('You didn''t input 1, 2, or 3.')
            specific_loss = input('Enter 1 for OI, 2 for spatial_filter, or 3 for PBS: ');
        end
        if specific_loss == 1
          loss_element_added = [loss_element_added, losses(1)];
          disp('Youve chosen an OI')
        elseif specific_loss == 2
            loss_element_added = [loss_element_added, losses(2)];
            disp('Youve chosen a spatial filter')
        elseif specific_loss == 3
            loss_element_added = [loss_element_added, losses(3)];
            disp('Youve chosen a PBS')
        end
        while length(loss_element_dummy(1,:))<length(loss_element_added)
            nada = zeros(1,length(loss_element_dummy));
            loss_element_dummy = [loss_element_dummy,nada'];
        end
```

```
        loss = input('Is there another loss element after your rod? Hit 1 for yes and 0 for no: ');
        while (loss ~= 0) && (loss ~= 1) %loops until you press the right thing
            clc
            disp('You didn"t input 0 or 1.')
            loss = input('Is there another loss element after your rod? Hit 1 for yes and 0 for no: ');
        end
    end
    while length(loss_element_dummy(1,:))>length(loss_element_added)
        loss_element_added = [loss_element_added,0];
    end
    loss_element_dummy = [loss_element_dummy;loss_element_added];
    disp(['This leg now has ', num2str(k+1), ' rods'])
    rod_prompt = input('Is there another rod in the leg? Hit 1 for yes and 0 for no: ');
    while (rod_prompt ~= 0) && (rod_prompt ~= 1) %loops until you press the right thing
        clc
        disp('You didn"t input 0 or 1.')
        rod_prompt = input('Is there another rod in the leg? Hit 1 for yes and 0 for no: ');
    end
    k = k + 1;
end
ssg(1,m) = {ssg_dummy};
rod_prop(1,m) = {rod_prop_dummy};
rod_length(1,m) = {rod_length_dummy};
rod_diameter(1,m) = {rod_diameter_dummy};
loss_element(1,m) = {loss_element_dummy};
clc
mode = input('Is this a single-pass, double pass, or regen? Hit 1 for single, 2 for double, or 3
for regen: ');


[Gaussian_prop,Gaussian_final_prop,Es_correct,Es_max,Es,Es_check,P,E_stored,scatter_y,lamb
```

```
da,output_energy,output_time] =
Passes(rod_diameter,rod_prop,lambda,ssg,pulses,mode,rod_length,loss_element,rep_rate,input_e
nergy,lambda_0_laser, bandwidth,m,laser_pulse_width,time,pulse_width);

    % Losses between legs

    loss_element_added = [];
    loss = input('Is there a loss element after this leg? Hit 1 for yes and 0 for no: ');
    while (loss ~= 0) && (loss ~= 1) %loops until you press the right thing
        clc
        disp('You didn''t input 0 or 1.')
        loss = input('Is there a loss element after this leg? Hit 1 for yes and 0 for no: ');
    end
    if loss == 0
        while length(loss_element_initial)>length(loss_element_added)
            loss_element_added = [loss_element_added,0];
        end
    end
    while loss == 1
        specific_loss = input('Enter 1 for OI, 2 for spatial_filter, or 3 for PBS: ');
        while (specific_loss ~= 1) && (specific_loss ~= 2) && (specific_loss ~= 3) %loops until
you press the right thing
            clc
            disp('You didn''t input 1, 2, or 3.')
            specific_loss = input('Enter 1 for OI, 2 for spatial_filter, or 3 for PBS: ');
        end
        if specific_loss == 1
          loss_element_added = [loss_element_added, losses(1)];
          disp('Youve chosen an OI')
        elseif specific_loss == 2
            loss_element_added = [loss_element_added, losses(2)];
```

```
        disp('Youve chosen a spatial filter')
    elseif specific_loss == 3
        loss_element_added = [loss_element_added, losses(3)];
        disp('Youve chosen a PBS')
    end
    while length(loss_element_dummy(1,:))<length(loss_element_added)
        nada = zeros(1,length(loss_element_dummy));
        loss_element_dummy = [loss_element_dummy,nada'];
    end
    loss = input('Is there another loss element after this leg? Hit 1 for yes and 0 for no: ');
    while (loss ~= 0) && (loss ~= 1) %loops until you press the right thing
        clc
        disp('You didn''t input 0 or 1.')
        loss = input('Is there another loss element after this leg? Hit 1 for yes and 0 for no: ');
    end
end
while length(loss_element_initial)>length(loss_element_added)
    loss_element_added = [loss_element_added,0];
end
loss_element_dummy = [loss_element_dummy;loss_element_added];
for i = 1:length(loss_element_dummy(end,:))
    if loss_element_dummy(end,i) > 0
        output_energy = output_energy.*loss_element_dummy(end,i);
        scatter_y = scatter_y.*loss_element_dummy(end,i);
    end
end
leg_prompt = input('Is there another leg in this laser? Hit 1 for yes and 0 for no: ');
while (leg_prompt ~= 0) && (leg_prompt ~= 1) %loops until you press the right thing
    clc
    disp('You didn''t input 0 or 1.')
    leg_prompt = input('Is there another leg in this laser? Hit 1 for yes and 0 for no: ');
```

```
end
if leg_prompt == 0
    scatter_x = linspace(1, pulses, pulses)*burst_length;
    figure()

    scatter(scatter_x,scatter_y*pi*(beam_diameter/2)^2);
    set(gcf, 'color', 'w');
    title('Output Burst Profile')
    xlabel('Time (ms)')
    ylabel('Energy/Pulse (J)')

    figure()
    subplot(2,1,1)
    hold on
    bandwidth_plot = output_energy(end,:)/max(output_energy(end,:));
    plot(lambda, laser_bandwidth, '-k', 'Linewidth', 2)
    plot(lambda,bandwidth_plot, '--r', 'Linewidth', 2)
    title('Frequency Domain')
    xlabel('Wavelength (m)')
    ylabel('Normalized Intensity')
    legend('Input Bandwidth','Final Bandwidth')
    legend('Location','south')
    legend('boxoff')
%     title(legend, 'Spectral Bandwidths')
    hold off
    k = 1;
    while bandwidth_plot(1,k)<.1
        k = k + 1;
    end
    xlim_low = lambda(1,k);
    k = length(bandwidth_plot);
```

```
        while bandwidth_plot(1,k)<.1
            k = k - 1;
        end
        xlim_high = lambda(1,k);
        xlim([xlim_low xlim_high])
        ylim([0 1])
        set(gcf, 'color', 'w');
        set(gca,'FontSize',12)
        subplot(2,1,2)
        hold on
        pulse_width_plot = output_time(:,end)/max(output_time(:,end));
        plot(time,laser_pulse_width_0, '-k', 'Linewidth', 2)
        plot(time, pulse_width_plot,'--r', 'Linewidth', 2)
        title('Temporal Domain')
        xlabel('Time (s)')
        ylabel('Normalized Intensity')
        legend('Input Pulse Width','Final Pulse Width')
        legend('Location','south')
        legend('boxoff')
        set(gca,'FontSize',12)
    %     title(legend, 'Temporal Pulse Widths')
        hold off
    end
end

function [loss_element] = losses(input)

OI = 0.95; %Optical Isolator
spatial_filter = 0.8;
PBS = 0.95; %Polarizing beamsplitter
Mirror = 0.999;
```

```
if input == 1
   loss_element = OI;
elseif input == 2
   loss_element = spatial_filter;
elseif input == 3
   loss_element = PBS;
end

end

function pulses = burst(burst_length,rep_rate)

pulses = burst_length*rep_rate; %total pulses is a function of the period and burst length

end

function
[Gaussian_prop,Gaussian_final_prop,Es_correct,Es_max,Es,Es_check,P,E_stored,scatter_y,lamb
da,output_energy,output_time] =
Passes(rod_diameter,rod_prop,lambda,ssg,pulses,mode,rod_length,loss_element,rep_rate,input_e
nergy,lambda_0_laser, bandwidth,m,laser_pulse_width,time,distance,pulse_width)
Gaussian_prop = []; %establish matrix for tracking gain bandwidth of rod
Gaussian_final_prop = []; %establish matrix for tracking normalized gain bandwidth of rod
Es_correct = []; %establish a matrix for displaying the correct value of the saturation fluence
Es_max = []; %establish a matrix displaying the peak saturation fluence
Es = {}; %establish a cell for saturation fluence
Es_check = []; %establish a matrix to double check the area under the curve is equal to the
correct value
P = {}; %establish a cell for pumping power
E_stored = {}; %establish a cell for stored rod energy
```

```
A21_matrix = {}; %establish a cell for the Einstein coefficient
sigma_se = []; %establish a matrix for the stimulated emission coefficient
scatter_y = []; %establish a matrix for output fluence values
eta = {}; %establish a cell for rod extraction efficiency
g0 = {}; %establish a cell for the small-signal gain coefficent
linspace_count = 50; %generic incremental value
lambda2 = []; %establish a matrix for another set of lambda values
output_energy = []; %establish a matrix for output fluence
cw_energy_individual = []; %establish a matrix for input fluence
output_time = []; %establish a matrix for output temporal domain

total = 0;
increment = lambda(2)-lambda(1); %generic increment value for lambda
time_increment = time(2)-time(1); %generic increment value for time
   function [c,h,delta_lambda,lambda_0_prop,density,M,M_p,kb,A21,
sigma_se]=Matprops(laser_prop)

   if laser_prop == 1
      c = 3E8; % speed of light (m/s)
      h = 6.626E-34; % Planck's constant (J*s)
      delta_lambda = 4.5E-10; % Nd:YAG linewidth (m)
      lambda_0_prop = 1064.45E-9; % Nd:YAG central wavelength (m)
      density = 4560; % Nd:YAG density (kg/m^3)
      M = 593.7; % YAG molecular weight (kg/kmol)
      M_p = 1.6727E-27; % mass of proton (kg)
      kb = 1.381E-23; % Boltzmann's constant (m^2*kg*s^-2*K^-1)
      A21 = 1/230E-6; % Einstein coefficient (s^-1)
      sigma_se = 2.8E-23; % m^2
   end
   if laser_prop == 2
      c = 3E8; % m/s
```

```
        h = 6.626E-34; % J*s
        delta_lambda = 27.7E-9; % m
        lambda_0_prop = 1062E-9; %m
        density = 4560; % kg/m^3
        M = 593.7; %kg/kmol
        M_p = 1.6727E-27; %kg
        kb = 1.381E-23; %m^2*kg*s^-2*K^-1
        A21 = 1/340E-6; % s^-1
        sigma_se = 2.9E-24; % m^2
    end
    end
for i = 1:length(rod_prop{1,m})
    [c,h,delta_lambda,lambda_0_prop,density,M,M_p,kb,A21,
sigma_se]=Matprops(rod_prop{1,m}(i,1));
    A21_matrix(1,i) = {A21}; %Einstein coefficients allocated to correct rods
end
for i = 1:length(lambda)
    laser_bandwidth = 2./((bandwidth./(2.*sqrt(2.*log(2)))).*sqrt(2.*pi)).*exp(-(lambda-
lambda_0_laser).^2./(2.*(bandwidth./(2.*sqrt(2.*log(2)))).^2)); %creating laser bandwidth with
respect to lambda values
end

for i = 1:pulses
    if m == 1 %if this is the first leg
        cw_energy_individual_dummy = input_energy(i,1).*laser_bandwidth; %apply laser
bandwidth spectrum to each pulse
        cw_pulse = trapz(lambda, cw_energy_individual_dummy); %area under the curve
        cw_energy_individual =
[cw_energy_individual;cw_energy_individual_dummy.*input_energy(i,1)./cw_pulse]; %creates
the proper total fluence under the curve per pulse
    else
```

```
        cw_energy_individual = [cw_energy_individual;input_energy(i,:)]; %input fluence is
already correctly setup for new legs
    end
end

for i = 1:length(rod_prop{1,m})
    [c,h,delta_lambda,lambda_0_prop,density,M,M_p,kb,A21,
sigma_se]=Matprops(rod_prop{1,m}(i,1));
    Gaussian_prop_dummy = 2./((delta_lambda./(2.*sqrt(2.*log(2)))).*sqrt(2.*pi)) ...
    .*exp(-(lambda-lambda_0_prop).^2./(2.*(delta_lambda./(2.*sqrt(2.*log(2)))).^2)); %rod gain
bandwidth
    Gaussian_prop = [Gaussian_prop;Gaussian_prop_dummy]; %matrix of rod gain bandwidths
    Gaussian_final_prop_dummy =
Gaussian_prop_dummy./max(Gaussian_prop_dummy); %normalized rod gain bandwidth
    Gaussian_final_prop = [Gaussian_final_prop;Gaussian_final_prop_dummy]; %matrix of
normalized rod gain bandwidths
    Es_correct_dummy = h*c/lambda_0_prop./sigma_se; %correct saturation fluence
    Es_correct = [Es_correct;Es_correct_dummy]; %matrix of correct saturation fluences
    Es_max_dummy = h*c/lambda_0_prop/sigma_se; %maximum saturation fluence
    Es_max = [Es_max;Es_max_dummy]; %matrix of maximum saturation fluences
    Es_dummy = Es_max(i,:).*Gaussian_final_prop(i,:); %saturation fluence per wavelength
    Es_check_dummy = trapz(lambda,Es_dummy); %check area under the curve
    Es_dummy = Es_dummy.*Es_correct_dummy./Es_check_dummy; %correct adjusted values
    Es(1,i) = {Es_dummy}; %add saturation fluence to saturation fluence cell
    Es_check = [Es_check; trapz(lambda,Es_dummy)]; %double check to verify it's right
    P_dummy = Es_dummy.*A21.*transpose(log(ssg{1,m}(i,:)+.001)); %pump for this rod based
on ssg
    P(1,i) = {P_dummy}; %add pump to pump cell
    E_stored_dummy = 0; %set initial stored energy to 0
    E_stored(1,i) = {E_stored_dummy}; %add initial stored energy to cell
end
```

```
%Single Pass

if mode == 1 %single pass selected

    hold on
    for i = 1:pulses %pulse count
        E0 = cw_energy_individual(i,:); %establish each starting pulse to be the input pulse fluence
        k = 1; %rod count
        front_pass_matrix = []; %establish matrix for individual temporal portions of a pulse
        front_pass_total_matrix = []; %establish matrix for total temporal pulse
        laser_pulse_width_total = sum(laser_pulse_width); %total temporal pulse values
        laser_pulse_width_fraction = laser_pulse_width./laser_pulse_width_total; %allocated
fractional fluence to each time step

        for w = 1:length(time) %pulse temporal domain count
            k = 1; %rod count
        %Forward pass
            E0 = cw_energy_individual(i,:); %re-establish E0 as the input pulse
            while k <= length(rod_length{1,m}) %applying loss elements to input fluence

                for j = 1:length(loss_element{1,m}(k,:))
                    if loss_element{1,m}(k,j) > 0
                        E0 = E0*loss_element{1,m}(k,j);
                    end
                end

                if ssg{1,m}(k,i) < 1 %makes ssg fit above 1 at all points so equation does not break
down
                    ssg{1,m}(k,i) = 2;
                end
```

```
            if w == 1
                g0(1,k) = {log(ssg{1,m}(k,i))./rod_length{1,m}(1,k)}; %establish ssg coefficient
            end

            if P{1,k}(i,:) < 0 %Making sure Power fit is not less than 0
                P{1,k}(i,:) = 0;
            end

            if k == 1
                E00 = E0.*laser_pulse_width_fraction(w); %fractional fluence applied before first
rod only
            else
                E00 = E0;
            end
            front_pass_dummy_noGB = Es{1,k}.*log(1+(exp(E00./Es{1,k})-
1).*exp(E_stored{1,k}./Es{1,k})); %front pass dummy gain no bandwidth multiplication
            front_pass_dummy_GB = Es{1,k}.*log(1+(exp(E00./Es{1,k})-
1).*exp(E_stored{1,k}./Es{1,k})).*Gaussian_final_prop(k,:); %front pass dummy gain
bandwidth multiplication
            front_pass_dummy_noGB_check = trapz(lambda,front_pass_dummy_noGB); %front
pass dummy no gain bandwidth integral
            front_pass_dummy_GB_check = trapz(lambda, front_pass_dummy_GB); %front pass
dummy GB integral
            front_pass =
front_pass_dummy_GB.*(front_pass_dummy_noGB_check/front_pass_dummy_GB_check); %a
djusted front pass to lock total ssg to correct value and keep bandwidth changes
            front_pass_total = trapz(lambda,front_pass); %front pass check
            E00_total = trapz(lambda,E00); %initial fluence check
            eta(1,k) = {(trapz(lambda,front_pass) -
trapz(lambda,E00))./(g0{1,k}.*rod_length{1,m}(1,k).*trapz(lambda,Es{1,k}))}; %total
extraction efficiency
```

```
            if eta{1,k} < 0 %stops accidental negative values from appearing. Eta must be >= 0
               eta{1,k} = 0;
            elseif eta{1,k} > 1 %stops accidental values >1 (check)
               eta{1,k} = 1;
            end
            g0(1,k) = {g0{1,k}.*(1-eta{1,k})}; %updated ssg coefficent
            E_stored(1,k) = {E_stored{1,k}.*exp(-A21_matrix{1,k}.*(time_increment)) +
P{1,k}(i,:).*(1./A21_matrix{1,k}).*(1-exp(-A21_matrix{1,k}.*(time_increment)))-
E_stored{1,k}.*(1-(1-eta{1,k}))}; %fluence stored updated between time steps
            if E_stored{1,k} < 0 %needed in case fluence stored goes negative during first pulse
               E_stored{1,k} = 0;
            end
            k = k + 1; %rod count
            E0 = front_pass; %ouput fluence becomes input
         end
         front_pass_matrix = [front_pass_matrix; front_pass]; %updated front pass matrix
         front_pass_total_matrix = [front_pass_total_matrix; front_pass_total]; %updated total
front pass matrix
      end

      for j = 1:length(loss_element{1,m}(k,:)) %loss elements after rods
         if loss_element{1,m}(k,j) > 0
               E0 = E0*loss_element{1,m}(k,j);
         end
      end
      for j = 1:length(rod_length{1,m}) %fluence stored updated between pulses
         E_stored(1,j) = {E_stored{1,j}.*exp(-A21_matrix{1,j}./rep_rate) +
P{1,j}(i,:).*(1./A21_matrix{1,j}).*(1-exp(-A21_matrix{1,j}./rep_rate))};
      end
      output_time = [output_time, front_pass_total_matrix]; %temporal output
```

```
        output_energy = [output_energy; sum(front_pass_matrix)]; %wavelength dependent fluence
output
        scatter_y = [scatter_y,sum(front_pass_total_matrix)]; %total fluence output
    end
    hold off
end

%Double Pass

if mode == 2 %double pass selected
    hold on
    for i = 1:pulses
        E0 = cw_energy_individual(i,:); %establish each starting pulse to be the input pulse fluence
        k = 1; %rod count
        front_pass_matrix = []; %establish matrix for individual temporal portions of a pulse for the
forward pass
        front_pass_total_matrix = []; %establish matrix for total temporal pulse for the forward pass
        back_pass_matrix = []; %establish matrix for individual temporal portions of a pulse for the
backward pass
        back_pass_total_matrix = []; %establish matrix for total temporal pulse for backward pass
        laser_pulse_width_total = sum(laser_pulse_width); %total of temporal pulse values
        laser_pulse_width_fraction = laser_pulse_width./laser_pulse_width_total; %allocated
fractional fluence to each time step

        for w = 1:length(time) %pulse temporal domain count

        %Forward pass

            E0 = cw_energy_individual(i,:); %re-establish E0 as the input pulse
            while k <= length(rod_length{1,m}) %applying loss elements to input fluence
```

```
            for j = 1:length(loss_element{1,m}(k,:))
                if loss_element{1,m}(k,j) > 0
                    E0 = E0*loss_element{1,m}(k,j);
                end
            end

            if ssg{1,m}(k,i) < 1 %makes ssg fit above 1 at all points so equation does not break
down
                ssg{1,m}(k,i) = 2;
            end
            if w == 1
                g0(1,k) = {log(ssg{1,m}(k,i))./rod_length{1,m}(1,k)}; %establish ssg coefficient
            end

            if P{1,k}(i,:) < 0 %making sure power fit is not less than 0
                P{1,k}(i,:) = 0;
            end

            if k == 1
                E00 = E0.*laser_pulse_width_fraction(w); %fractional fluence applied before first
rod only
            else
                E00 = E0;
            end
            front_pass_dummy_noGB = Es{1,k}.*log(1+(exp(E00./Es{1,k})-
1).*exp(E_stored{1,k}./Es{1,k})); %front pass dummy gain no bandwidth multiplication
            front_pass_dummy_GB = Es{1,k}.*log(1+(exp(E00./Es{1,k})-
1).*exp(E_stored{1,k}./Es{1,k})).*Gaussian_final_prop(k,:); %front pass dummy gain
bandwidth multiplication
            front_pass_dummy_noGB_check = trapz(lambda,front_pass_dummy_noGB); %front
pass dummy no gain bandwidth integral
```

```
            front_pass_dummy_GB_check = trapz(lambda, front_pass_dummy_GB); %front pass
dummy GB integral
            front_pass =
front_pass_dummy_GB.*(front_pass_dummy_noGB_check/front_pass_dummy_GB_check); %a
djusted front pass to lock total ssg to correct value and keep bandwidth changes
            front_pass_total = trapz(lambda,front_pass); %front pass check
            E00_total = trapz(lambda,E00); %total fluence check
            eta(1,k) = {(trapz(lambda,front_pass) -
trapz(lambda,E00))./(g0{1,k}.*rod_length{1,m}(1,k).*trapz(lambda,Es{1,k}))}; %total
extraction efficiency
            if eta{1,k} < 0 %stops accidental negative values from appearing. Eta must be >= 0
               eta{1,k} = 0;
            elseif eta{1,k} > 1 %stops value from exceeding 1 (check)
               eta{1,k} = 1;
            end
            g0(1,k) = {g0{1,k}.*(1-eta{1,k})}; %updated ssg coefficent
            E_stored(1,k) = {E_stored{1,k}.*exp(-A21_matrix{1,k}.*(time_increment)) +
P{1,k}(i,:).*(1./A21_matrix{1,k}).*(1-exp(-A21_matrix{1,k}.*(time_increment)))-
E_stored{1,k}.*(1-(1-eta{1,k}))}; %fluence stored updated between time steps
            if E_stored{1,k} < 0 %needed in case fluence stored goes negative during first pulse
               E_stored{1,k} = 0;
            end
            k = k + 1; %rod count
            E0 = front_pass; %ouput fluence becomes input
         end

      %Backward pass

         while k > 1
            for j = 1:length(loss_element{1,m}(k,:)) %applying loss elements to input fluence
               if loss_element{1,m}(k,j) > 0
```

```
            if k == length(rod_length{1,m}) + 1
                E0 = E0*loss_element{1,m}(k,j)^2;
            end
            E0 = E0*loss_element{1,m}(k,j);
        end
    end
    if ssg{1,m}(k-1,i) < 1 %makes ssg fit above 1 at all points so equation does not break down
        ssg{1,m}(k-1,i) = 2;
    end

    total = 0;
    if P{1,k-1}(i,:) < 0 %making sure power fit is not less than 0
        P{1,k-1}(i,:) = 0;
    end
    E00 = E0;
    back_pass_dummy_noGB = Es{1,k-1}.*log(1+(exp(E00./Es{1,k-1})-1).*exp(E_stored{1,k-1}./Es{1,k-1})); %front pass dummy gain no bandwidth multiplication
    back_pass_dummy_GB = Es{1,k-1}.*log(1+(exp(E00./Es{1,k-1})-1).*exp(E_stored{1,k-1}./Es{1,k-1})).*Gaussian_final_prop(k-1,:); %front pass dummy gain bandwidth multiplication
    back_pass_dummy_noGB_check = trapz(lambda,back_pass_dummy_noGB); %front pass dummy no gain bandwidth integral
    back_pass_dummy_GB_check = trapz(lambda, back_pass_dummy_GB); %front pass dummy GB integral
    back_pass = back_pass_dummy_GB.*(back_pass_dummy_noGB_check/back_pass_dummy_GB_check); %adjusted front pass to lock total ssg to correct value and keep bandwidth changes
    back_pass_total = trapz(lambda,back_pass); %back pass check
    E00_total = trapz(lambda,E00); %total fluence check
```

```
            eta(1,k-1) = {(trapz(lambda,back_pass) - trapz(lambda,E00))./(g0{1,k-
1}.*rod_length{1,m}(1,k-1).*trapz(lambda,Es{1,k-1}))}; %total extraction efficiency
            if eta{1,k-1} < 0 %stops accidental negative values from appearing. Eta must be >= 0
               eta{1,k-1} = 0;
            elseif eta{1,k-1} > 1 %stops value from exceeding 1 (check)
               eta{1,k-1} = 1;
            end
            g0(1,k-1) = {g0{1,k-1}.*(1-eta{1,k-1})}; %updated ssg coefficent
            E_stored(1,k-1) = {E_stored{1,k-1}.*exp(-A21_matrix{1,k-1}.*(time_increment)) +
P{1,k-1}(i,:).*(1./A21_matrix{1,k-1}).*(1-exp(-A21_matrix{1,k-1}.*(time_increment)))-
E_stored{1,k-1}.*(1-(1-eta{1,k-1}))}; %fluence stored updated between time steps
            if E_stored{1,k-1} < 0 %needed in case fluence stored goes negative during first pulse
               E_stored{1,k-1} = 0;
            end
            k = k - 1; %rod count
            E0 = back_pass; %ouput fluence becomes input
         end

         front_pass_matrix = [front_pass_matrix; front_pass]; %updated front pass matrix
         front_pass_total_matrix = [front_pass_total_matrix; front_pass_total]; %updated total
front pass matrix
         back_pass_matrix = [back_pass_matrix; back_pass]; %updated back pass matrix
         back_pass_total_matrix = [back_pass_total_matrix; back_pass_total]; %updated total
back pass matire
      end
      for j = 1:length(rod_length{1,m}) %fluence stored updated between pulses
         E_stored(1,j) = {E_stored{1,j}.*exp(-A21_matrix{1,j}./rep_rate) +
P{1,j}(i,:).*(1./A21_matrix{1,j}).*(1-exp(-A21_matrix{1,j}./rep_rate))};
      end
      output_time = [output_time, back_pass_total_matrix]; %temporal output
```

```
        output_energy = [output_energy; sum(back_pass_matrix)]; %wavelength dependent fluence
output
        scatter_y = [scatter_y,sum(back_pass_total_matrix)]; %total fluence output
    end
    hold off
end
end

function ssg = small_signal_gain(ssg_prompt, burst_length, pulses)

time2 = linspace(0,burst_length,pulses); %time domain established from burst
ssg = []; %ssg matrix

for i = 1:length(time2)
    ssg = [ssg,ssg_prompt.*(1-exp(-time2(i)./10E-6))]; %ssg formulated
end

end

function cw_energy = energy(cw_power, rep_rate)

cw_energy = cw_power/rep_rate; % initial pulse energy (J)

end

function [laser_pulse_width_0, laser_bandwidth, laser_spatial, lambda, time, space, increment] =
time_bandwidth_spatial_input(lambda_0_laser, pulse_width, bandwidth, beam_diameter)

linspace_count = 100;
lambda = linspace(lambda_0_laser - bandwidth, lambda_0_laser + bandwidth,
linspace_count); % m
```

```
time = linspace( -pulse_width, pulse_width, linspace_count); %s
space = linspace( -beam_diameter, beam_diameter, linspace_count); % m
increment = (lambda(2)-lambda(1));
sigma = beam_diameter/(2*sqrt(2*log(2)));
for i = 1:length(lambda)
    laser_bandwidth = 2./((bandwidth./(2.*sqrt(2.*log(2)))).*sqrt(2.*pi)) ...
        .*exp(-(lambda-lambda_0_laser).^2./(2.*(bandwidth./(2.*sqrt(2.*log(2))))).^2));
    laser_pulse_width_0 = 2./((pulse_width./(2.*sqrt(2.*log(2)))).*sqrt(2.*pi)).*exp(-(time).^2 ...
        ./(2.*(pulse_width./(2.*sqrt(2.*log(2))))).^2));
end
for i = 1:length(space)
        laser_spatial = 2./(2.*pi.*sigma.^2).*exp(-((space.^2)+(space'.^2))./(2.*sigma.^2));
end
laser_spatial = laser_spatial./laser_spatial(linspace_count/2,linspace_count/2);
laser_bandwidth = laser_bandwidth./max(laser_bandwidth);
laser_pulse_width_0 = laser_pulse_width_0./max(laser_pulse_width_0);

end

function [c,h,delta_lambda,lambda_0_prop,density,M,M_p,kb,A21,
sigma_se]=Matprops(laser_prop)

if laser_prop == 1
    c = 3E8; % speed of light (m/s)
    h = 6.626E-34; % Planck's constant (J*s)
    delta_lambda = 4.5E-10; % Nd:YAG linewidth (m)
    lambda_0_prop = 1064.45E-9; % Nd:YAG central wavelength (m)
    density = 4560; % Nd:YAG density (kg/m^3)
    M = 593.7; % YAG molecular weight (kg/kmol)
    M_p = 1.6727E-27; % mass of proton (kg)
    kb = 1.381E-23; % Boltzmann's constant (m^2*kg*s^-2*K^-1)
```

```
    A21 = 1/230E-6; % Einstein coefficient (s^-1)
    sigma_se = 2.8E-23; % m^2
end
if laser_prop == 2
    c = 3E8; % m/s
    h = 6.626E-34; % J*sa
    delta_lambda = 27.7E-9; % m
    lambda_0_prop = 1062E-9; %m
    density = 4560; % kg/m^3
    M = 593.7; %kg/kmol
    M_p = 1.6727E-27; %kg
    kb = 1.381E-23; %m^2*kg*s^-2*K^-1
    A21 = 1/340E-6; % s^-1
    sigma_se = 2.9E-24; % m^2

end
end
```

APPENDIX B. REGENERATIVE AMPLIFIER CODE

```
%% Pre cavity


d1 = 100; %first distance
d2 = 50; %second distance
d3 = 4350; %this is the important variable distance in the cavity
d4 = 50; %fourth distance
dvar = 980; %variable distance
% d5 = -2050;
l_pc = 50; %Pockels cell length
l_pbs = 12.5; %polarizing beamsplitter length
l_rod = 100; %rod length
L = d1+d2+d3+d4+l_pc+l_pbs+l_rod; %total length to cavity
n_air = 1; %air index of refraction
n_pc = 1.5; %Pockels cell index of refraction
n_pbs = 1.5; %polarizing beamsplitter index of refraction
n_rod = 1.5; %rod index of refraction
y00 = .125/2; %initial beam radius from fiber
R0 = .591; %initial guessed radius of curvature (m^-1)
q0 = (1./R0 - 1i*1064E-6/(pi*y00^2*n_pbs)); %initial complex beam parameter
R_rod1 = 1000000000; %estimated thermal lens
R_rod2 = -1000000000; %estimated thermal lens
f = 1/((n_rod-1)*(1/R_rod1-1/R_rod2+(n_rod-1)*l_rod/n_rod/R_rod1/R_rod2)); %estimated
thermal lensing
T01 = [1 d1; 0 1]; %distance
T02 = [1 0; 0 n_pc/n_air]; %PC
T03 = [1 l_pc; 0 1]; %PC
T04 = [1 0; 0 n_air/n_pc]; %PC
T05 = [1 d2; 0 1]; %distance
T06 = [1 0; 0 n_pbs/n_air]; %PBS
```

```
T07 = [1 l_pbs; 0 1]; %PBS
T08 = [1 0; 0 n_air/n_pbs]; %PBS
T09 = [1 d3; 0 1]; %distance
T010 = [1 0; -(n_air-n_rod)/n_air/R_rod1 n_rod/n_air]; %rod
T011 = [1 l_rod; 0 1]; %rod
T012 = [1 0; -(n_rod-n_air)/n_rod/R_rod2 n_air/n_rod]; %rod
T013 = [1 0; 0 n_pbs/n_air]; %PBS
T014 = [1 l_pbs; 0 1]; %PBS
T015 = [1 0; 0 n_air/n_pbs]; %PBS
T016 = [1 25.4; 0 1]; %distance
T017 = [1 0; 0 n_pbs/n_air]; %OI
T018 = [1 25.4*4; 0 1]; %OI
T019 = [1 0; 0 n_air/n_pbs]; %OI
T020 = [1 dvar; 0 1]; %variable distance
T021 = [1 0; 0 n_pbs/n_air]; %HWP
T022 = [1 9.7; 0 1]; %HWP
T023 = [1 0; 0 n_air/n_pbs]; %HWP
T024 = [1 25.4; 0 1]; %distance
T025 = [1 0; 0 n_pbs/n_air]; %PBS
T026 = [1 l_pbs; 0 1]; %PBS
T027 = [1 0; 0 n_air/n_pbs]; %PBS
T028 = [1 25.4*4; 0 1]; %distance
T029 = [1 0; 0 n_pbs/n_air]; %QWP
T030 = [1 9.7; 0 1]; %QWP
T031 = [1 0; 0 n_air/n_pbs]; %QWP
T032 = [1 25.4*2; 0 1]; %distance
T033 = [1 0; 0 n_pbs/n_air]; %VBG
T034 = [1 25.4*4; 0 1]; %VBG
T035 = [1 0; 0 n_air/n_pbs]; %VBG
T036 = [1 50.8; 0 1]; %distance
T037 = [1 0; 0 n_pbs/n_air]; %QWP
```

```
T038 = [1 9.7; 0 1]; %QWP
T039 = [1 0; 0 n_air/n_pbs]; %QWP
T040 = [1 25.4*4; 0 1]; %distance
T041 = [1 0; 0 n_pbs/n_air]; %OI
T042 = [1 25.4*4; 0 1]; %OI
T043 = [1 0; 0 n_air/n_pbs]; %OI
T044 = [1 50.8; 0 1]; %distance
T045 = [1 0; .5/(1*-5.48) 1.5]; %n1 is glass n2 is air
T046 = [1 3.69; 0 1]; %asphere thickness
T047 = [1 0; -.5/(1.5*632.73) 1]; %n1 is air n2 is glass
T048 = [1 12.3; 0 1]; %guessed distance between asphere and fiber
T049 = [1 0; 0 n_pbs/n_air]; %fiber
T0 =
T01*T02*T03*T04*T05*T06*T07*T08*T09*T010*T011*T012*T013*T014*T015*T016*T01
7*T018*T019*T020*T021*T022*T023*T024*T025*T026*T027*T028*T029*T030*T031*T0
32*T033*T034*T035*T036*T037*T038*T039*T040*T041*T042*T043*T044*T045*T046*T
047*T048*T049; %total precavity transfer matrix
q1 = (T0(2,2).*q0+T0(2,1))./(T0(1,2).*q0+T0(1,1)); %complex beam parameter going into cavity
disp((1./real(q1))); %radius of curvature check
disp(sqrt(1064E-6./(-imag(q1))./pi)) %beam radius check

%% Cavity

R1 = 6200; %all units in mm %convex mirror
R2 = -6800; %concave mirror
% q1 = (1/R1 - 1i*1064E-6/(pi*1^2*1));
T1 = [1 0; 2/R1 1]; %mirror
T2 = [1 d1; 0 1]; %distance
T3 = [1 0; 0 n_pc/n_air]; %PC
T4 = [1 l_pc; 0 1]; %PC
T5 = [1 0; 0 n_air/n_pc]; %PC
```

```
T6 = [1 d2; 0 1]; %distance
T7 = [1 0; 0 n_pbs/n_air]; %PBS
T8 = [1 l_pbs; 0 1]; %PBS
T9 = [1 0; 0 n_air/n_pbs]; %PBS
T10 = [1 d3; 0 1]; %distance
T11 = [1 0; -(n_air-n_rod)/n_air/R_rod1 n_rod/n_air]; %rod
T12 = [1 l_rod; 0 1]; %rod
T13 = [1 0; -(n_rod-n_air)/n_rod/R_rod2 n_air/n_rod]; %rod
T14 = [1 d4; 0 1]; %distance
T15 = [1 0; 2/R2 1]; %mirror
T16 = [1 d4; 0 1]; %distance
T17 = [1 0; 0 n_rod/n_air]; %rod
T18 = [1 l_rod; 0 1]; %rod
T19 = [1 0; 0 n_air/n_rod]; %rod
T20 = [1 d3; 0 1]; %distance
T21 = [1 0; 0 n_pbs/n_air]; %PBS
T22 = [1 l_pbs; 0 1]; %PBS
T23 = [1 0; 0 n_air/n_pbs]; %PBS
T24 = [1 d2; 0 1]; %distance
T25 = [1 0; 0 n_pc/n_air]; %PC
T26 = [1 l_pc; 0 1]; %PC
T27 = [1 0; 0 n_air/n_pc];%PC
T28 = [1 d1; 0 1]; %PC

T = T1*T2*T3*T4*T5*T6*T7*T8*T9*T10*T11*T12*T13*T14*T15*T16*T17*T18*T19*T20*T21*T22*T23*T24*T25*T26*T27*T28; %cavity transfer matrix
TM2 = T15*T16*T17*T18*T19*T20*T21*T22*T23*T24*T25*T26*T27*T28; %half cavity transfer matrix
q2 = (T(2,2).*q1+T(2,1))./(T(1,2).*q1+T(1,1)); %complex beam parameter through a cavity pass
clc
```

```
disp(1./real(q2)) %radius of curvature check
disp(sqrt(1064e-6./(-imag(q2))./pi)) %beam radius check
disp((T(2,2)+T(1,1))./2) %stability check
% TM2 = T3*T2*T1*T2*T3*T2*T1*T2*T3*T2;
S= []; %stability matrix
R = []; %mirror 1 radius of curvature matrix
w = []; %mirror 1 beam radius matrix
w2 = []; %mirror 2 beam radius matrix
TT = []; %cavity passes matrix
figure()

for i = 1:30
   TT = [TT,T^i]; %cavity passes matrix
   q2 = (TT(2,2*i)*q1+TT(2,2*i-1))/(TT(1,2*i)*q1+TT(1,2*i-1)); %complex beam parameter per
cavity pass
   S = [S,(TT(2,2)+TT(1,1)+2)/4]; %stability per cavity pass
   R = [R,1/real(q2)]; %radius of curvature per cavity pass
   w = [w,sqrt(1064E-6/(-imag(q2))/pi)]; %mirror 1 beam radius per cavity pass
   TTM2 = TM2*T^i; %adjusted for mirror 2
   q2 = (TTM2(2,2)*q1+TTM2(2,1))/(TTM2(1,2)*q1+TTM2(1,1)); %adjust complex beam
parameter
   w2 = [w2,sqrt(1064E-6/(-imag(q2))/pi)]; %mirror 2 beam radius per cavity pass
end
subplot(2,2,1)
plot(S, '.')
set(gcf,'color','w')
set(gca,'FontSize',8)
ax = gca;
ax.XAxis.MinorTick = 'on';
ax.XAxis.MinorTickValues = 0:1:30;
ax.YAxis.MinorTick = 'on';
```

```
ax.YAxis.MinorTickValues = 0:0.02:1;
axis([1 30 0 1])
title('Cavity Stability')
xlabel('# of Double Passes')
ylabel('Stability')
subplot(2,2,2)
plot(R, '.')
set(gcf,'color','w')
set(gca,'FontSize',8)
ax = gca;
ax.XAxis.MinorTick = 'on';
ax.XAxis.MinorTickValues = 0:1:30;
ax.YAxis.MinorTick = 'on';
ax.YAxis.MinorTickValues = 0:500:5000;
axis([1 30 5000 7000])
title('Radius of Curvature at M1')
xlabel('# of Double Passes')
ylabel('Radius of Curvature (mm)')
subplot(2,2,3)
plot(w, '.')
set(gcf,'color','w')
set(gca,'FontSize',8)
ax = gca;
ax.XAxis.MinorTick = 'on';
ax.XAxis.MinorTickValues = 0:1:30;
ax.YAxis.MinorTick = 'on';
ax.YAxis.MinorTickValues = 0:0.02:1;
axis([1 30 0 2])
title('Beam Radius at M1')
xlabel('# of Double Passes')
ylabel('Beam Radius (mm)')
```

```
subplot(2,2,4)
plot(w2, '.')
set(gcf,'color','w')
set(gca,'FontSize',8)
ax = gca;
ax.XAxis.MinorTick = 'on';
ax.XAxis.MinorTickValues = 0:1:30;
ax.YAxis.MinorTick = 'on';
ax.YAxis.MinorTickValues = 0:0.02:1;
axis([1 30 0 5])
title('Beam Radius at M2')
xlabel('# of Double Passes')
ylabel('Beam Radius (mm)')
```

APPENDIX C. SELF-PHASE MODULATION CODE

```
c = 3E8; % m/s
h = 6.626E-34; % J*s
laser_delta_lambda = 20E-9; %m
delta_lambda = 27.7E-9; % m
lambda_0_laser = 1064E-9; % m
lambda_0_q246 = 1062E-9; %m
nonlinear_index = 1.4E-13/4.19E7; %m^2/W
beam_diameter = 12.5E-6; % m
pulse_width = 15.5E-12; % s
rod_length = .1013; % m
A21 = 1/340E-6; % s^-1
Rep_Rate = 100000; %s^-1
cw_power = .4; % W
cw_energy = cw_power/Rep_Rate; % J
L = 5; %m
I_0 = cw_energy./pulse_width./(pi.*(beam_diameter/2).^2);
n2 = 28.7E-21;

%Create frequency and time domains

Linspace_count = 1000;
lambda = linspace(-.25*delta_lambda+lambda_0_laser,lambda_0_laser+.25*delta_lambda,
Linspace_count); % m
omega = 2.*pi.*c./lambda; %instantaneous frequency
wavenumber = 1E7./(lambda_0_laser.*1E9)- 1E7./(lambda.*1E9); %wavenumber conversion
time = linspace( -3*pulse_width, 3*pulse_width, Linspace_count); %s
increment = (lambda(2)-lambda(1));
n_sellmeier = sqrt(1+1.12365662.*(lambda.*1000000).^2./((lambda.*1000000).^2-
0.00644742752)+0.309276848.*(lambda.*1000000).^2./((lambda.*1000000).^2-
```

```
0.0222284402)+0.881511957.*(lambda.*1000000).^2./((lambda.*1000000).^2-
107.297751)); %BAK1
n_0 = n_sellmeier(length(lambda));

%Establish gamma = w0^2*n0*n2/(Beta0*c^2*Aeff)

D = .003; % m
A_eff = 2*pi*(D/2)^2; %A_eff is usually 1.5 to 2.5 times the actual core area
beta_0 = omega.*n_sellmeier./c; %0th order spectral phase
gamma = omega.*n_sellmeier.*n2./beta_0./c.^2./A_eff; %proportionality constant

%Establish |a|^2 = P(t) = I0*exp(-t^2/tau^2)
B = [1,10,20]; %B-integral
P_t = I_0.*exp(-time.^2./pulse_width.^2); %P(t)
delta_omega = -I_0.*gamma.*L.*(2.*time.*exp(-
time.^2./pulse_width.^2))./pulse_width.^2; %isnt freq. shift
tm = pulse_width/sqrt(2); %temporal value
figure()
hold on
for i = 1:length(B)
    wm = B(i)./tm.*exp(-.5); %Intensity minima related
    wm_prime = wm - pi^(2/3)*wm^(1/3)/2/pulse_width^(2/3); %related to position of outermost
spectral peak
    delta_t = 2.*tm.*sqrt((omega-wm)./wm); %interfering time instance separation
    delta_phi_D = omega.*delta_t.*10E-5; %linear phase difference
    delta_phi_NL = -wm_prime.*delta_t*1E1; %nonlinear phase difference
    delta_phi =(delta_phi_D+delta_phi_NL); %total phase difference
    Intensity = P_t + P_t + 2.*sqrt(P_t.*P_t).*cos(delta_phi + pi/2); %Intensity output
    omega_new = omega+delta_omega; %Instantaneous frequency change
    plot(2.*pi.*c./omega_new*1E9,Intensity/max(Intensity),'Linewidth',5)
end
```

```
plot(2.*pi.*c./omega_new*1E9, P_t/max(P_t), 'Linewidth', 5);
set(gcf,'color','w')
set(gca,'FontSize',12)
xlabel('Wavelength (nm)')
ylabel('Normalized Intensity')
legend('B = 1','B = 10','B = 20', 'Initial Bandwidth')
title(legend, 'B-Integral Values')
hold off
```